Keiichi Kitamura

Advancement of Shock Capturing Computational Fluid Dynamics Methods

Numerical Flux Functions in Finite Volume Method

Springer

Advancement of Shock Capturing Computational Fluid Dynamics Methods

Keiichi Kitamura

Advancement of Shock Capturing Computational Fluid Dynamics Methods

Numerical Flux Functions in Finite Volume Method

Springer

Keiichi Kitamura
Faculty of Engineering
Yokohama National University
Yokohama, Kanagawa, Japan

ISBN 978-981-15-9010-8 ISBN 978-981-15-9011-5 (eBook)
https://doi.org/10.1007/978-981-15-9011-5

© The Editor(s) (if applicable) and The Author(s), under exclusive license to Springer Nature Singapore Pte Ltd. 2020
This work is subject to copyright. All rights are solely and exclusively licensed by the Publisher, whether the whole or part of the material is concerned, specifically the rights of translation, reprinting, reuse of illustrations, recitation, broadcasting, reproduction on microfilms or in any other physical way, and transmission or information storage and retrieval, electronic adaptation, computer software, or by similar or dissimilar methodology now known or hereafter developed.
The use of general descriptive names, registered names, trademarks, service marks, etc. in this publication does not imply, even in the absence of a specific statement, that such names are exempt from the relevant protective laws and regulations and therefore free for general use.
The publisher, the authors, and the editors are safe to assume that the advice and information in this book are believed to be true and accurate at the date of publication. Neither the publisher nor the authors or the editors give a warranty, expressed or implied, with respect to the material contained herein or for any errors or omissions that may have been made. The publisher remains neutral with regard to jurisdictional claims in published maps and institutional affiliations.

This Springer imprint is published by the registered company Springer Nature Singapore Pte Ltd.
The registered company address is: 152 Beach Road, #21-01/04 Gateway East, Singapore 189721, Singapore

This book is dedicated to Chihiro, Misora,
and Tsubasa.

Preface

There are well-known computational fluid dynamics (CFD) books such as *Numerical Computation of Internal and External Flows. Vol. 1: The Fundamentals of Computational Fluid Dynamics*, 2nd ed., Butterworth-Heinemann, Burlington, VA, 2007, by Hirsch, C., and *Riemann Solvers and Numerical Methods for Fluid Dynamics: A Practical Introduction*, 3rd ed., Springer-Verlag Berlin Heidelberg, 2009, by Toro, E. F. They were written primarily for CFD beginners in a very reader-friendly manner, and have been read all over the world for decades. However, because CFD technology is updated every year, these books naturally lack very recent information. This is the primary motivation for writing this book. In other words, this book is intended to bridge the gap between well-known CFD books and state-of-the-art CFD technologies, including the ones proposed by the author himself. Particular attention will be paid to numerical flux functions, which have significant impacts on flow solutions. In fact, recent developments in flux functions are scattered in various papers in different journals. The author has therefore collected these pieces of knowledge and technologies and summarized them in a consistent manner: this is the second motivation for writing the present book.

This book is organized as follows: After a brief introduction to CFD in Chap. 1, Chap. 2 will be dedicated to two important reported problems concerning a finite volume method (FVM) for compressible CFD at high speeds (e.g., the carbuncle phenomenon) and low speeds (e.g., the stiffness problem). The numerical flux functions will be explained in Chap. 3, ranging from Godunov's exact Riemann solver to the recently proposed all-speed fluxes such as the Simple Low-dissipation Advection Upstream Splitting Method 2 (SLAU2). Chapter 4 introduces their extensions to real fluids, i.e., multiphase flows, supercritical fluids, and magnetohydrodynamics (MHD), based on separate technical papers but with all the new and original numerical results prepared for the present book. In Chap. 5, slope limiters typically used with those numerical fluxes will be described. Hopefully, the reader will be able to distinguish the areas that are already well established from the areas that are still under development in CFD technology, after reading this book.

Yokohama, Japan Keiichi Kitamura
August 2020

Acknowledgments

The author thanks his past advisors and collaborators:
Prof. Emeritus Yoshiaki Nakamura (Nagoya University, Japan)
Dr. Eiji Shima (JAXA, Japan)
Prof. Philip L. Roe (University of Michigan, USA)
Dr. Hiroaki Nishikawa (National Institute for Aerospace, USA)
Dr. Meng-Sing Liou (NASA Glenn Research Center, USA) (Deceased)
Prof. Z.J. Wang (University of Kansas, USA)
Dr. Atsushi Hashimoto (JAXA, Japan)
Dr. Masashi Kanamori (JAXA, Japan)
Assoc. Prof. Taku Nonomura (Tohoku University, Japan)
Assoc. Prof. Hiroshi Terashima (Hokkaido University, Japan)
Dr. Takashi Minoshima (JAMSTEC, Japan)
Prof. Dinshaw S. Balsara (University of Notre Dame, USA)
Prof. Dongsu Ryu (UNIST, Republic of Korea)
and
All the members of Aerodynamics Laboratory (Yokohama National University, Japan).

This work was partially supported by the JSPS KAKENHI grant number JP19K04834.

Contents

Chapter 1
Introduction: Brief Review of Finite Volume Method (FVM) in Computational Fluid Dynamics

Abstract Computational fluid dynamics (CFD) is sometimes regarded as a mature technology. In the author's opinion, this is only partly correct. The fundamental ideas of CFD such as the finite volume method (FVM) are indeed well established, whereas some classes of problems such as hypersonic heating or real fluid simulations are still challenging, as will be discussed in the subsequent chapters. Thus, we begin this book by reviewing those basics in this chapter, specifically by describing the governing equations (i.e., the Navier–Stokes equations, or equations of mass, momentum, and energy conservation) for compressible flows. They are discretized, for computational purposes, by the FVM, which is the conventional procedure. Through this approximation, the equations are closed along with the equation of state and are valid for every computational element (=cell). In this chapter, only a brief explanation is given of how those equations are numerically solved in the framework of the FVM, using methods such as space reconstruction, slope limiting, flux computation, and time integration. Interested readers, including who have just entered the CFD world, are encouraged to refer to the standard books mentioned in the Preface.

Keywords Computational fluid dynamics (CFD) · Finite volume method (FVM) · Flux function

1.1 Finite Volume Method

In the finite volume method (FVM), a control volume (such as a cell in a cell-centered method; Fig. 1.1) rather than a mesh point is considered as a computational element. Then, for each control volume, the governing equations in discretized form are solved to satisfy the conservation laws of mass, momentum, and energy. The next subsection is dedicated to the governing equations, their FVM discretization, and a brief explanation of the whole computational procedure of FVM for solving the discretized equations.

K. Kitamura, *Advancement of Shock Capturing Computational Fluid Dynamics Methods*, https://doi.org/10.1007/978-981-15-9011-5_1

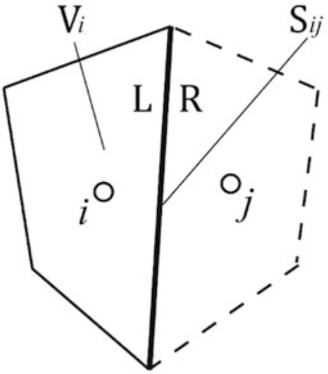

Fig. 1.1 Schematic of cell geometric properties

Readers who have recently entered the CFD world are encouraged to refer to, for instance, Chap. 5 (p. 208) of [1] to see why the FVM (in its conservative form) is necessary for flows involving strong discontinuities such as shocks. References [2–6] are also recommended for reviewing the fundamentals of CFD.

1.2 Governing Equations

The governing equations, the compressible Navier–Stokes (N–S) equations, are described as follows for single-phase air. They include the preconditioning matrix $\mathbf{\Gamma}$ of Weiss and Smith [7, 8] for low-speed flows, which is simply eliminated in the non-preconditioned form if not necessary. In general, conservative variables are commonly used in compressible flow solvers. Thus, in this book, we will use the conservative variables $\mathbf{Q}$ as dependent variables [9, 10], although the primitive variables $\mathbf{q}$ [11] or characteristic variables $\mathbf{w}$ can be used instead.

$$\mathbf{\Gamma}\frac{\partial \mathbf{Q}}{\partial t}+\frac{\partial \mathbf{F}_k}{\partial x_k}=\frac{\partial \mathbf{Fv}_k}{\partial x_k} \tag{1.1}$$

$$\mathbf{Q}=\begin{bmatrix}\rho\\ \rho u_l\\ \rho E\end{bmatrix},\mathbf{F}_k=\begin{bmatrix}\rho u_k\\ \rho u_l u_k+p\delta_{lk}\\ \rho u_k H\end{bmatrix},\mathbf{Fv}_k=\begin{bmatrix}0\\ \tau_{lk}\\ u_m\tau_{mk}+\kappa\dfrac{\partial T}{\partial x_k}\end{bmatrix} \tag{1.2}$$

$$\tau_{lk}=\mu\left(\frac{\partial u_l}{\partial x_k}+\frac{\partial u_k}{\partial x_l}\right)-\frac{2}{3}\mu\frac{\partial u_n}{\partial x_n}\delta_{lk} \tag{1.3}$$

where $k, l, m = 1, 2, 3$ in 3D, ρ is the density, u_l denotes the velocity components in Cartesian coordinates, E is the total energy per unit *mass* (do not confuse this with the total energy per unit *volume*, ρE), p is the pressure, H is the total enthalpy ($H = E + (p/\rho)$), and T is the temperature. The first line corresponds to the mass conservation equation (continuity equation), the second line to the momentum conservation equation (equation of motion, or N–S equation in a narrow sense), and the last line is called the energy conservation equation. These constitute the full set of the N–S equations in a broad sense, in the vector form above.

The working gas is air approximated by the calorically perfect gas model ($p = \rho RT$, where R is the universal gas constant, $R \simeq 287$ [J/kg/K] for air; $E = (p/\rho)/(\gamma\text{-}1) + \mathbf{u}^2/2$) with the specific heat ratio $\gamma = 1.4$. The Prandtl number is $\mathrm{Pr} \simeq 0.72$. The molecular viscosity μ and thermal conductivity κ are related as $\kappa = \mathrm{c_p}\mu/\mathrm{Pr}$, where $\mathrm{c_p}$ is the specific heat at constant pressure. **F** and **Fv** are called the inviscid and viscous fluxes, respectively.

In the Euler (=inviscid) simulations, μ is merely turned off ($\mu = \kappa = 0$). In the Reynolds-averaged turbulence calculations, the molecular viscosity μ is replaced by ($\mu + \mu_t$), where μ_t is the turbulence viscosity given by a turbulence model. Likewise, κ is replaced by ($\kappa + \mathrm{c_p}\mu_t/\mathrm{Pr}_t$), and Pr_t is the turbulent Prandtl number, $\mathrm{Pr}_t \simeq 0.89$.

Equation (1.1) is solved with a finite-volume code, and can be written in the delta form as

$$\frac{V_i}{\Delta t}\Delta\mathbf{Q}_i + \boldsymbol{\Gamma}_i^{-1}\sum_j \left(\mathbf{F}_{ij} - \mathbf{Fv}_{ij}\right)S_{ij} = 0 \tag{1.4}$$

where V_i stands for the volume of cell i, Δt is the (global) time step, $\Delta\mathbf{Q}_i = \mathbf{Q}_i^{n+1} - \mathbf{Q}_i^n$ is the change in the conservative variables in time from the nth to the (n + 1)-th step, $\mathbf{F}_{ij}$ and $\mathbf{Fv}_{ij}$ are the inviscid (Euler) and viscous fluxes through the cell interface S_{ij} (which separates cell i from its neighbor cell j), respectively (see Fig. 1.1). Remember that $\Delta\mathbf{Q}_i$ is what we want at the current time step. To obtain this, we perform the following procedure (see Fig. 1.2):

i. The values $\mathbf{Q}_{ij,L/R}$ (or $\mathbf{q}_{ij,L/R}$) at the interface $S_{i,j}$ are computed (interpolated) from the cell-center values via the Monotonic Upstream-centered Scheme for Conservation Laws (MUSCL) [15], the Least-Squares, or Green-Gauss [16] reconstruction method.
ii. A slope limiter is then called to suppress possible oscillations.
iii. The fluxes $\mathbf{F}_{ij}$ and $\mathbf{Fv}_{ij}$ are computed. A numerical flux function such as Roe [12] or SLAU(2) [9, 13] determines $\mathbf{F}_{ij}$, while $\mathbf{Fv}_{ij}$ is typically computed by a central difference or its modified form (with a dissipation term for unstructured grids [14]).
iv. Now that all the unknown values are obtained, time is marched for Δt by either an explicit (e.g., Euler, Runge-Kutta) or implicit method (e.g., Lower-Upper Symmetric Gauss-Seidel (LU-SGS) [17]) to obtain $\Delta\mathbf{Q}_i$ (and hence, $\mathbf{Q}_i^{n+1} = \mathbf{Q}_i^n + \Delta\mathbf{Q}_i$).
v. Here we are at the next time level (n ← n + 1), and it is time to return to step (i).

These steps (i)–(v) are contained in one time step, and they are repeated until a prescribed termination time or step count is reached, or a convergence criterion is satisfied. This whole procedure is called a Godunov-type scheme. Next chapter will

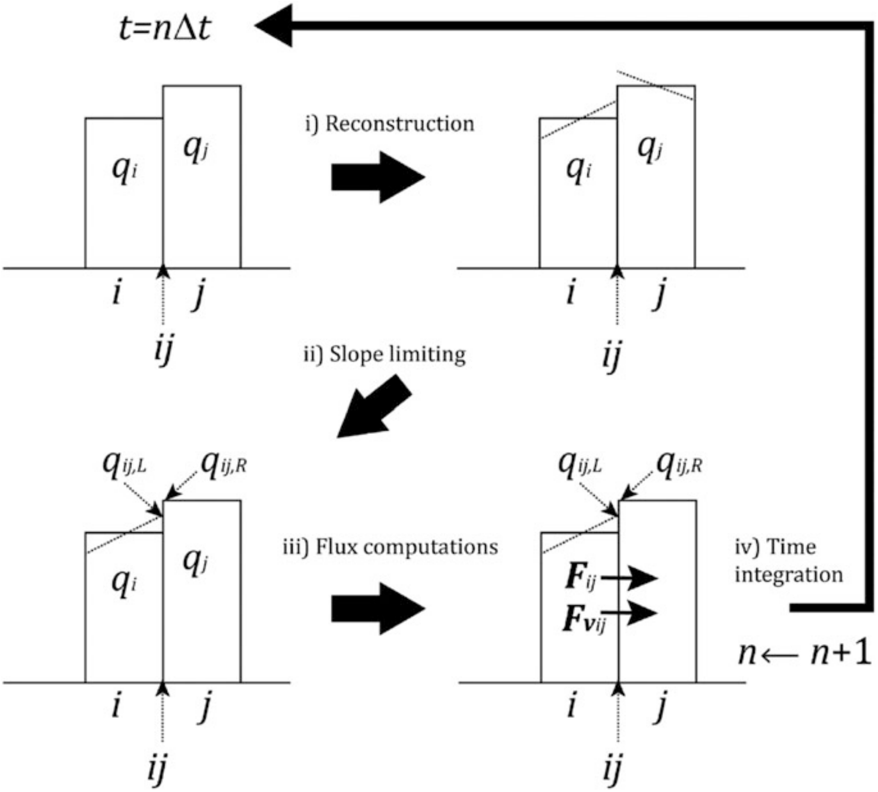

Fig. 1.2 Schematic of one time step in FVM

describe two issues of the Godunov-type scheme of FVM, which has been widely used as a standard compressible CFD method.

References

1. Hirsch, C.: Numerical Computation of Internal and External Flows Vol. 1: the Fundamentals of Computational Fluid Dynamics, 2nd edn. Butterworth-Heinemann, Burlington (2007)
2. Hirsch, C.: Numerical Computation of Internal and External Flows Vol. 2: computational Methods for Inviscid and Viscous Flows (Wiley Series in Numerical Methods in Engineering). Wiley (1990). ISBN 978-0471924524
3. Laney, C.B.: Computational Gasdynamics. Cambridge University Press, New York (1998. ISBN 9780511605604). https://doi.org/10.1017/CBO9780511605604
4. Anderson Jr., J.D.: Computational Fluid Dynamics. McGraw-Hill Education, New York (1995) 978-1259025969
5. Toro, E.F.: Riemann Solvers and Numerical Methods for Fluid Dynamics: a Practical Introduction, 3rd edn. Springer-Verlag, Berlin Heidelberg (2009). ISBN 978-3540252023

6. Masatsuka, K.: I do like CFD Vol. 1: governing Equations and Exact Solutions. (2009). https://www.lulu.com/commerce/index.php?fBuyContent=5991452
7. Weiss, J.M., Smith, W.A.: Preconditioning applied to variable and constant density flows. AIAA J. **33**(11), 2050–2057 (1995)
8. Turkel, E.: Preconditioning technique in computational fluid dynamics. Annu. Rev. Fluid Mech. **31**, 385–416 (1999)
9. Shima, E., Kitamura, K.: Parameter-free simple low-dissipation AUSM-family scheme for all speeds. AIAA J. **49**(8), 1693–1709 (2011). https://doi.org/10.2514/1.55308
10. Unrau, D., Zingg, D.W.: Viscous airfoil computations using local preconditioning. In: AIAA Paper 972027 (1997)
11. Hauke, G., Hughes, T.J.R.: A comparative study of different sets of variables for solving compressible and incompressible flows. Comput. Methods Appl. Mech. Eng. **153**, 1–44 (1998)
12. Roe, P.L.: Approximate Riemann solvers, parameter vectors and difference schemes. J. Comput. Phys. **43**, 357–372 (1981)
13. Kitamura, K., Shima, E.: Towards shock-stable and accurate hypersonic heating computations: a new pressure flux for AUSM-family schemes. J. Comput. Phys. **245**, 62–83 (2013)
14. Wang, Z.J.: A Quadtree-based adaptive Cartesian/Quad grid flow solver for Navier-Stokes equations. Comput. Fluids. **27**(4), 529–549 (1998)
15. van Leer, B.: Towards the ultimate conservative difference scheme. V. A second-order sequel to Godunov's method. J. Comput. Phys. **32**, 101–136 (1979)
16. Mavriplis, D.J., Revisiting the least-squares procedure for gradient reconstruction on unstructured meshes. AIAA Paper 2003-3986 (2003).
17. Jameson, A., Turkel, E.: Implicit schemes and LU decompositions. Math. Comput. **37**, 385–397 (1981)

Chapter 2
Role and History of Numerical Flux Functions

Abstract In spite of the (assumed) maturity of compressible CFD technologies today, simulations of a hypersonic flow and a low-speed flow (nearly incompressible flow) are still challenging. The former suffers from anomalous solutions arising from shock capturing (e.g., the carbuncle phenomena). This can be mitigated at least partly by carefully selecting a numerical flux function, a slope limiter, and a computational grid. However, there is no universal scheme that is completely free of those shock anomalies. The latter, the low-speed flow problem, is divided into two subproblems: very slow convergence, known as the "stiffness problem," and a physically incorrect solution due to huge numerical dissipation. Fortunately, these are known to be avoided if an appropriate combination is adopted for a time integration method and a numerical flux function. In this chapter, the current status of these problems is introduced with some actual numerical examples and the author's explanations based on his experience. The detailed formulations of the numerical algorithms are deferred to the next chapter or simply referred to external sources.

Keywords Hypersonic flow · Carbuncle · Shock wave · Aerodynamic heating · Preconditioning · Stiffness problem

2.1 Issue 1: Anomalous Solutions of Captured Shock and Heating at Hypersonic Speeds

Hypersonic flow computations still suffer from shockwave anomalous solutions such as the "carbuncle phenomenon" (Fig. 2.1) [1–4], a term borrowed from medical terminology. There is some confusion about whether the carbuncle is a numerical artifact or a physical phenomenon that is observed even in experiments. In either case, the carbuncle can severely degrade the predictability of hypersonic heating, which can be disastrous to space vehicles at reentry [5].

Let us briefly review how we derived numerical expressions for shockwaves (Fig. 2.2): (i) In the real world, the shock is very thin but has a certain thickness

K. Kitamura, *Advancement of Shock Capturing Computational Fluid Dynamics Methods*, https://doi.org/10.1007/978-981-15-9011-5_2

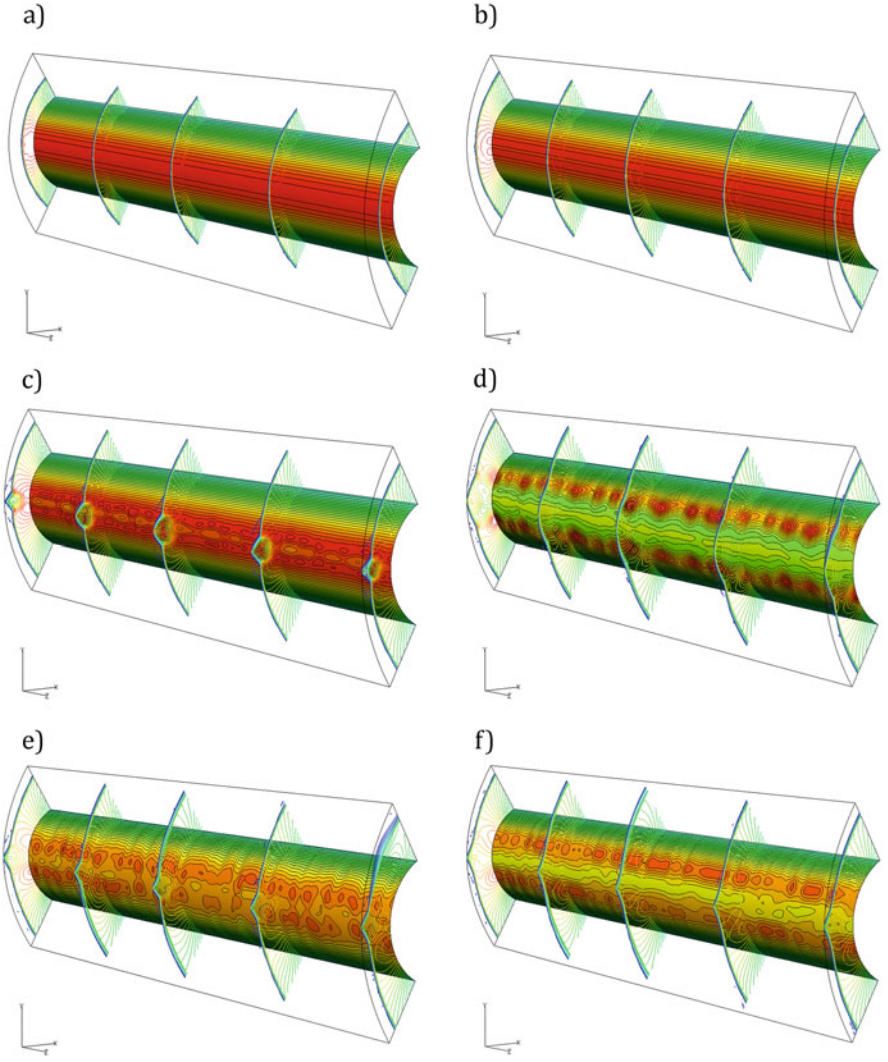

Fig. 2.1 Development of carbuncle phenomenon in hypersonic flow computations (pressure contours, Mach 6) (**a**) 500 steps, (**b**) 1000 steps, (**c**) 1500 steps, (**d**) 2000 steps, (**e**) 2500 steps, and (**f**) 5000 steps (Roe, E-fix)

(physically). (ii) On the other hand, if we express it using Euler equations (mathematically), we regard the shock as a discontinuous jump with zero thickness. (iii) However, when the shock is captured by an FVM (numerically), it should have a certain thickness again, but on the order of the cell size. It should be carefully noted that this shock thickness, along with its internal structure, is a numerical artifact, not a physical one.

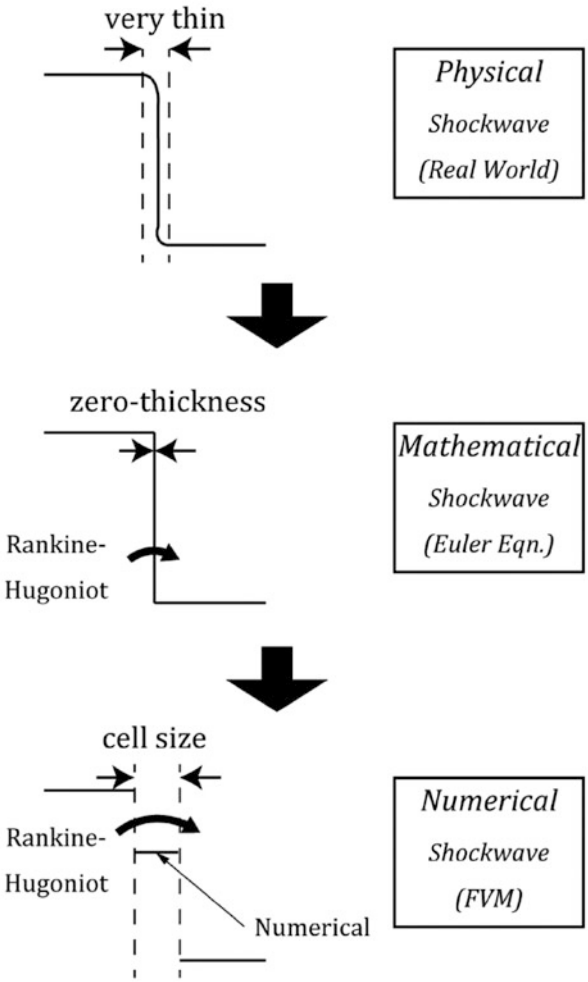

Fig. 2.2 Schematics of physical, mathematical, and numerically expressed shockwaves

Here is a very important observation: Barth [6] pointed out that along the Hugoniot curve, the mass conservation law is violated within the numerically captured shock by at most 40% at Mach 10, for instance [6]. Therefore, we are of the view that the shock anomalies are caused in part by the lack of a mathematical expression for the internal shock structure in the governing equations [6–9], and hence, we felt that they should be investigated with numerical experiments rather than with (invalid) mathematical considerations.

In 1988, Peery and Imlay [10] first identified the carbuncle, supported later by Quirk [1], Sanders [11], and others in the 1990s. They also proposed ways to relax it by introducing multidimensional dissipations. The 2000s saw important papers related to the shock anomalies. Liou [12] analyzed several flux functions, and he

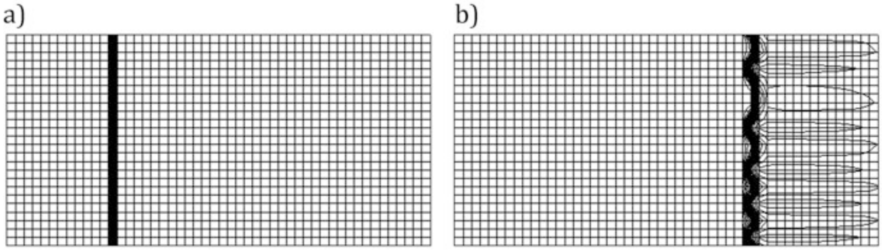

Fig. 2.3 "1-1/2D test" for the carbuncle (M=6): (**a**) stable, (**b**) unstable solutions (Harten–Lax–van Leer–Contact, HLLC)

concluded that a flux function having a pressure dissipation term in the mass flux is vulnerable to the carbuncle. Pandolfi and D'Ambrosio [2] investigated and summarized the occurrence of the carbuncle under various conditions with numerical methods, and proposed a method of suppressing it. Dumbser et al. [13] and Chauvat et al. [7] focused on the internal structure of the captured shockwave and the growth of numerical errors there. During this period, several numerical flux functions with controlled-dissipation terms that were *claimed to be carbuncle free* were published [14–16].

In our numerical experiments, however, those methods did exhibit shock anomalous solutions (carbuncle, oscillations of shock either in time or space, or wiggles) under certain circumstances, in the course of developing and investigating an entropy-consistent numerical flux [17]. At that time, the author was an exchange student at the University of Michigan, Ann Arbor, Michigan, United States, under supervision of Prof. Philip L. Roe and Prof. Bram van Leer. We then decided to switch our research motivation and direction from flux development to an examination of popular flux functions under as many conditions as possible, such as the Mach number, initial shock location relative to the grid line, cell geometry, numerical methods—eventually, it turned out that all the methods tested (including Harten–Lax–van Leer–Einfeldt, HLLE) showed either of 1D and 2D shock anomalies (Fig. 2.3) (Table 2.1). This discovery was first presented at the AIAA Computational Fluid Dynamics Conference in Miami, Florida, 2007, and then published in *AIAA Journal* in 2009 [3].

In our series of subsequent works [3, 18–24], the following findings have also been reported:

- Even though the carbuncle is avoided, the aeroheating may or may not be erroneous.
- The carbuncle appears even in 3D (Fig. 2.1).
- Several flux functions passed the 1-1/2D test (Table 2.2). However, even these methods exhibited shock anomalies under more severe conditions, such as Mach 20 or computational cells having a large aspect ratio (e.g., 10).
- While the pressure dissipation term can cause the carbuncle, it also suppresses multidimensional wiggles at the shock.

Table 2.1 Summary of computed results for 1-D and 1-1/2-D, M=6.0 steady shock tests with various flux functions [2: Symmetry and Converged, 1: Asymmetry or Oscillatory, and 0: Breakdown of Shock (Carbuncle)], modified from 2009

Scheme		Test problem	$\varepsilon = 0.0$	0.1	0.2	0.3	0.4	0.5	0.6	0.7	0.8	0.9	Total	
Godunov		1-D	1	2	2	2	2	2	2	1	1	1	16	16
		1-1/2-D	0	0	0	0	0	0	0	0	0	0	0	
Roe		1-D	1	2	2	2	2	2	2	1	1	1	16	22
		1-1/2-D	0	2	2	2	0	0	0	0	0	0	6	
	(E-fix)	1-D	2	2	2	2	2	2	2	2	2	2	20	20
		1-1/2-D	0	0	0	0	0	0	0	0	0	0	0	
EC-Roe	($\alpha = 0.2$)	1-D	2	2	2	2	2	1	1	1	1	2	16	29
		1-1/2-D	2	2	2	1	1	2	0	0	1	2	13	
	($\alpha = 0.8$)	1-D	2	2	2	2	2	2	2	2	2	2	20	20
		1-1/2-D	0	0	0	0	0	0	0	0	0	0	0	
HLLE		1-D	1	2	2	2	2	2	2	1	1	1	16	32
		1-1/2-D	1	2	2	2	2	2	2	1	1	1	16	
AUSMPW+		1-D	2	2	2	2	2	2	2	1	1	1	17	35
		1-1/2-D	2	2	2	2	2	2	2	1	1	2	18	
RoeM		1-D	1	2	2	2	2	2	2	2	1	1	17	28
		1-1/2-D	1	1	1	1	1	2	1	1	1	1	11	
AUSM+		1-D	2	2	2	2	1	1	1	2	2	2	17	33
		1-1/2-D	2	2	2	2	1	1	1	1	2	2	16	
AUSM$^+$-up		1-D	2	2	2	2	2	1	1	1	2	2	17	33
		1-1/2-D	2	2	2	2	2	1	1	1	1	2	16	

Table 2.2 Summary of computed results for 1-D and 1-1/2-D M=6.0 steady shock tests with various flux functions [2: Symmetry and Converged, 1: Asymmetry or Oscillatory, and 0: Breakdown of Shock (Carbuncle)], modified from 2013

Scheme	Test problem	$\varepsilon = 0.0$	0.1	0.2	0.3	0.4	0.5	0.6	0.7	0.8	0.9	Total	
van Leer	1-D	2	2	2	2	2	2	2	2	2	2	20	40
	1-1/2-D	2	2	2	2	2	2	2	2	2	2	20	
Hänel	1-D	2	2	2	2	2	2	2	2	2	2	20	40
	1-1/2-D	2	2	2	2	2	2	2	2	2	2	20	
AUSMDV	1-D	2	2	2	2	2	2	2	2	2	2	20	30
	1-1/2-D	1	1	1	1	1	1	1	1	1	1	10	
AUSMDV (shock fix)	1-D	2	2	2	2	2	2	2	2	2	2	20	40
	1-1/2-D	2	2	2	2	2	2	2	2	2	2	20	
Rotated-RHLL	1-D	1	2	2	2	2	2	2	1	1	1	16	36
	1-1/2-D	2	2	2	2	2	2	2	2	2	2	20	
SLAU	1-D	2	2	2	2	2	2	2	2	2	2	20	33
	1-1/2-D	1	2	2	2	1	1	1	1	1	1	13	
SLAU2	1-D	2	2	2	2	2	2	2	2	2	2	20	40
	1-1/2-D	2	2	2	2	2	2	2	2	2	2	20	

- Flux functions such as SLAU2 tend to capture the shock smoothly and broadly. For those methods, the minmod slope limiter using primitive variables is recommended for robustness.
- Even if the shock is stable in steady flow cases (Tables 2.1 and 2.2), it can collapse with time when it travels through the cells. For such a traveling shock, multidimensional dissipation, such as in Advection Upstream Splitting Method by Pressure Weight +, AUSMPW+ [14], was effective in stabilizing it. Research in this direction is still ongoing.

In addition, while recent papers [25–27] have claimed that they established effective methods to avoid carbuncles, the author failed to reproduce their results with his own code.

Now let us turn our attention to another important aspect of hypersonic CFD. As mentioned above, those shock anomalies lead to significant errors in aerodynamic heating at vehicle surfaces. The heating, or heat flux $\dot{q}$, can be expressed as

$$\dot{q} = -\kappa \nabla T$$

according to Fourier's law, where κ is the thermal conductivity, and T is the temperature. This is expressed more specifically in the surface wall normal (y) direction as

$$\dot{q} = -\kappa \frac{\partial T}{\partial y}$$

As can be clearly seen, $\dot{q}$ is proportional to the temperature gradient. Such differential values, as well as the surface friction c_f, are much more sensitive than non-differential values such as T or p (pressure). In particular, even though the surface pressure is well captured ($<1\%$ errors), the heating may exhibit large errors, O (10%), due to the locally very high-temperature gradients compared with the velocity counterparts (Fig. 2.4). This typically calls for very small-sized (Δy) cells near the wall (several orders smaller than the one employed in typical viscous simulations), i.e., $Re_{cell} = \frac{\rho U_\infty \Delta y}{\mu} \leq 3$ as recommended by Klopfer and Yee [28], although a strong basis to support its physical validity appears to be lacking. Thus, special attention must be paid to the computational grid generation, and implicit time integration is necessary due to the very small Δy. In addition, the isothermal wall condition is imposed at the wall boundary, instead of the adiabatic wall treatment, to resolve the temperature gradient very close to the wall. All these make the aeroheating computation extremely challenging.

The aeroheating is extremely high when a shock wave impinges on the wall, and the temperature boundary layer is detached (Fig. 2.5) (detailed explanations are found in [29, 30]). The temperature gradient is then locally magnified 10 or even 20 times [31, 32]. Edney classified such shock interferences into six types [31], and these (specifically, the strongest: "type IV") were further experimentally investigated by [32], and numerically investigated by [33, 34]. From the numerical point of view,

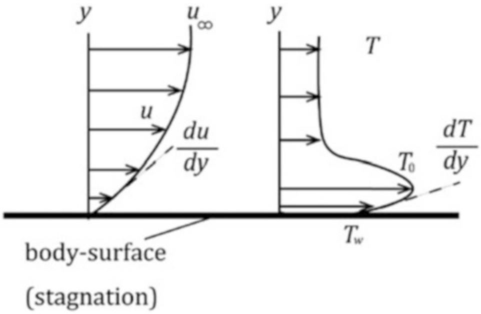

Fig. 2.4 Schematic of temperature gradient and velocity gradient within boundary layer

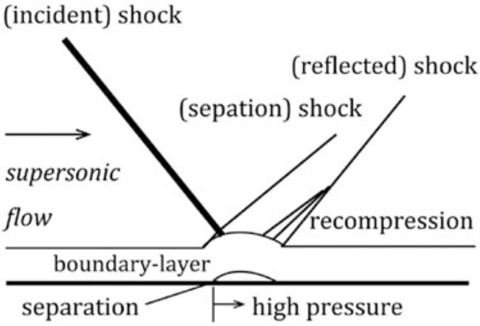

Fig. 2.5 Shock/boundary-layer interaction

Type IV heating is a tough benchmark problem, because apart from the steep temperature gradient, it involves a small jet structure hitting the wall to generate the peak heating value. Thus, Zhong [33] employed a spatially fifth-order essentially non-oscillatory (ENO) approach to reproduce Type IV in his computations. By contrast, the author in [23] successfully captured the Type IV interaction, including important physics, by using the second-order method (Fig. 2.6). As a result, in [18] and [23], we advocated three tips for accurate aeroheating computations:

1. Robustness against shock anomalies (e.g., the carbuncle phenomenon)
2. Conservation of total enthalpy (this proved to be less critical than the other two, though)
3. (Economical) Boundary-layer resolving (the ability of the Euler solver to sharply resolve contact discontinuities)

This set illustrates why it is difficult to capture aeroheating accurately, even under the perfect gas assumption. SLAU2 is designed to satisfy all those items. The multidimensional version of the Roe flux by Gnoffo [35] also captured heating at hypersonic speeds well.

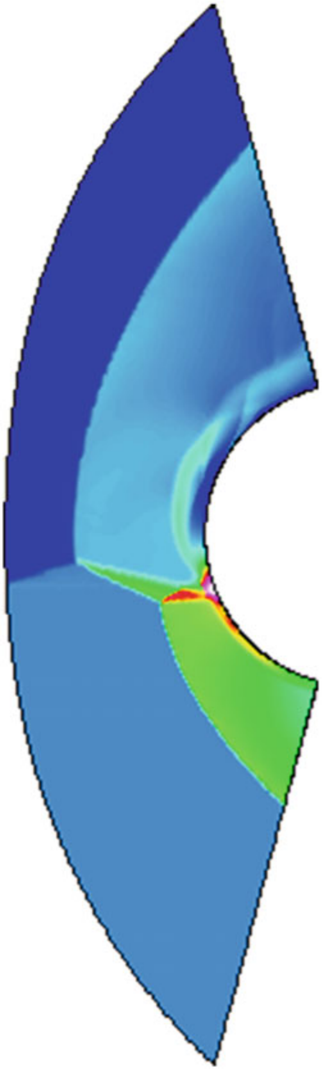

Fig. 2.6 Type IV shock/shock interaction solution (SLAU)

2.2 Issue 2: Stiffness Problem at Low Speeds

As the Mach number [= (flow speed)/(acoustic speed)] decreases, the compressibility of the fluid is weakened, and eventually incompressible treatment may become valid. In fact, many methods are available for treating incompressible flows numerically. However, such treatments have several drawbacks, exemplified by the lack of energy conservation and the physically unrealistic assumption of the speed of sound being infinity (i.e., all the information travels instantaneously). Thus, such an assumption is not suitable for problems involving both a low-speed flow and sound propagation. An ideal solution is, therefore, to propose a method of extending a compressible flow solver to an incompressible flow regime so that the flows at low speeds and the sound propagation are solved by a single method simultaneously. However, direct use of compressible flow simulation methods failed at low speeds for two reasons: (i) the stiffness problem (very degraded time progress due to the disparity in the characteristic speeds) and (ii) deteriorated solution (blatantly erroneous, due to excessive numerical dissipation). Research to resolve these issues was actively conducted in the 1980s and later.

Weiss and Smith [36] and Turkel [37] introduced "preconditioning" of the system of equations (e.g., Euler equations) to be solved. According to this concept, the speed of sound is artificially scaled down to the flow convection speed. This solved problem (i) above. At the same time, the dissipation of the order of the speed of sound (which was included in the Roe flux, for example) also had to be reduced to the flow-speed scale: then, problem (ii) was also resolved. See Sect. 3.3 and the equations therein, where the central difference term (the first term of the right-hand-side below) is O(M), while the dissipation term (the second term) is O(1) for the original Roe flux.

$$\mathbf{F}_{1/2(Roe)} = \frac{1}{2}(\mathbf{F}_L + \mathbf{F}_R) - \frac{1}{2}\widehat{\mathbf{R}}\left|\widehat{\mathbf{\Lambda}}\right|\widehat{\mathbf{L}}\mathbf{\Delta Q}$$

This creates no problem if $M = 1$, but at $M << 1$ the dissipation is huge compared with the first term, leading to completely erroneous solutions. Thus, the dissipation term is also preconditioned to O(M^2) as

$$\mathbf{F}_{1/2(P-Roe)} = \frac{1}{2}(\mathbf{F}_L + \mathbf{F}_R) - \frac{1}{2}\mathbf{\Gamma}^{-1}\widehat{\mathbf{R}}\left|\widehat{\mathbf{\Lambda}}\right|\widehat{\mathbf{L}}\mathbf{\Delta Q}$$

Later, the two problems have been separately discussed, because once (i) is solved, we do not have to necessarily resort to the Roe flux. Now the dissipation term has been properly scaled in many recent flux functions, such as AUSM(P), AUSM+-up, All-Speed Roe, SLAU, SLAU2, and HR (High-Resolution)-SLAU2, and used along with the preconditioned time integration method (such as the preconditioned LU-SGS, or "pLU-SGS") for low-speed flow computations.

In [38], the authors surveyed several numerical flux functions used together with LU-SGS or pLU-SGS for subsonic flows at Mach 0.001–0.5 around a 2D airfoil. Overall, combinations of "the all-speed schemes (e.g., SLAU) + pLU-SGS" were nearly always stable, but "the non-all-speed schemes (e.g., Roe)" were unable to arrive at a solution, regardless of the choice of the implicit method (Table 2.3).

Table 2.3 Computed results of three sub-iteration cases (CFL=20), **S** (Successful), and ***F*** (Failure: diverged, unphysical, or oscillatory))

		Inviscid			Viscous ($Re = 2000$)
Implicit schemes	Euler fluxes	$M_\infty = 0.1$	$M_\infty = 0.01$	$M_\infty = 0.001$	$M_\infty = 0.01$
LU-SGS	Roe	*F*			*F*
	AUSM+				
	SHUS				
	P-Roe	*F*	*F*	*F*	*F*
	A-Roe	S	*F*	*F*	*F*
	AUSM$^+$-up	*F*	*F*	*F*	*F*
	SLAU	S	S	S	S
pLU-SGS	Roe	*F*			*F*
	AUSM+				
	SHUS				
	P-Roe	S	S	S	S
	A-Roe	S	S	S	S
	AUSM$^+$-up	*F*	S	S	S
	SLAU	S	S	S	S

References

1. Quirk, J.J.: A contribution to the great Riemann solver debate. Int. J. Numer. Methods Fluids. **18**(6), 555–574 (1994). https://doi.org/10.1002/fld.1650180603
2. Pandolfi, M., D'Ambrosio, D.: Numerical instabilities in upwind methods: analysis and cures for the 'carbuncle' phenomenon. J. Comput. Phys. **166**(2), 271–301 (2001). https://doi.org/10.1006/jcph.2000.6652
3. Kitamura, K., Roe, P., Ismail, F.: Evaluation of Euler fluxes for hypersonic flow computations. AIAA J. **47**, 44–53 (2009). https://doi.org/10.2514/1.33735
4. Zaide, D., Roe, P.L.: Shock capturing anomalies and the jump conditions in one dimension. AIAA Paper 2011-3686 (2011)
5. Horvath, T.J.: Experimental aerothermodynamics in support of the Columbia accident investigation. In: AIAA 2004-1387, 42nd AIAA Aerospace Sciences Meeting and Exhibit 5–8 January 2004, Reno
6. Barth, T.J.: Some Notes on Shock-Resolving Flux Functions Part 1: Stationary Characteristics. NASA TM-101087 (1989)
7. Chauvat, Y., Moschetta, J.M., Gressier, J.: Shock wave numerical structure and the carbuncle phenomenon. Int. J. Numer. Methods Fluids. **47**(8–9), 903–909 (2005)
8. Robinet, J., Gressier, J., Casalis, G., Moschetta, J.: Shock wave instability and the carbuncle phenomenon: same intrinsic origin? J. Fluid Mech. **417**(1), 237–263 (2000)
9. Roe, P.L.: Fluctuations and signals—a framework for numerical evolution problems. In: Morton, K.W., Baines, M.J. (eds.) Numerical Methods for Fluid Dynamics, pp. 219–257. Academic Press, New York (1982)
10. Peery, K.M., Imlay, S.T.: Blunt-body flow simulations. In: AIAA Paper 88-2904 (1988)

11. Sanders, R., Morano, E., Druguetz, M.C.: Multidimensional dissipation for upwind schemes: stability and applications to gas dynamics. J. Comput. Phys. **145**(2), 511–537 (1998)
12. Liou, M.: Mass flux schemes and connection to shock instability. J. Comput. Phys. **160**(2), 623–648 (2000)
13. Dumbser, M., Moschetta, J.M., Gressier, J.: A matrix stability analysis of the carbuncle phenomenon. J. Comput. Phys. **197**(2), 647 (2004)
14. Kim, K.H., Kim, C., Rho, O.H.: Methods for the accurate computations of hypersonic flows I. AUSMPW+ scheme. J. Comput. Phys. **174**(1), 38–80 (2001)
15. Kim, S.S., Kim, C., Rho, O.H., Hong, S.K.: Cures for the shock instability: development of a shock-stable Roe scheme. J. Comput. Phys. **185**(2), 342 (2003)
16. Liou, M.S.: A sequel to AUSM, part II: AUSM+-up for all speeds. J. Comput. Phys. **214**, 137–170 (2006)
17. Ismail, F., Roe, P.L.: Affordable, entropy-consistent Euler flux functions 2: entropy production at shocks. J. Comput. Phys. **228**(15), 5410–5436 (2009)
18. Kitamura, K., Shima, E., Nakamura, Y., Roe, P.: Evaluation of Euler fluxes for hypersonic heating computations. AIAA J. **48**(4), 763–776 (2010)
19. Kitamura, K., Shima, E., Roe, P.: Carbuncle phenomena and other shock anomalies in three dimensions. AIAA J. **50**(12), 2655–2669 (2012). https://doi.org/10.2514/1.J051227
20. Shima, E., Kitamura, K.: Parameter-free simple low-dissipation AUSM-family scheme for all speeds. AIAA J. **49**(8), 1693–1709 (2011). https://doi.org/10.2514/1.55308
21. Shima, E., Kitamura, K.: Multidimensional numerical noise from captured shockwave and its cure. AIAA J. **51**(4), 992–998 (2013). https://doi.org/10.2514/1.J052046
22. Kitamura, K., Shima, E.: Towards shock-stable and accurate hypersonic heating computations: a new pressure flux for AUSM family schemes. J. Comput. Phys. **245**, 62–83 (2013)
23. Kitamura, K.: Assessment of SLAU2 and other flux functions with slope limiters in hypersonic shock-interaction heating. Comput. Fluids. **129**, 134–145 (2016). https://doi.org/10.1016/j.compfluid.2016.02.006
24. Kitamura, K., Shima, E.: Numerical experiments on anomalies from stationary, slowly moving, and fast-moving shocks. AIAA J. **57**(4), 1763–1772 (2019) https://arc.aiaa.org/doi/abs/10.2514/1.J057366
25. Chen, Z., Huang, X., Ren, Y., Zhou, M.: General procedure for Riemann-Solver to eliminate carbuncle and shock instability. AIAA J. **55**(6), 2002–2015 (2017)
26. Chen, Z., Huang, X., Ren, Y., Xie, Z., Zhou, M.: Mechanism-derived shock instability elimination for Riemann-Solver-based shock-capturing scheme. AIAA J. **56**(9), 3636–3651 (2018)
27. Rodionov, A.V.: Artificial viscosity in Godunov-type schemes to cure the carbuncle phenomenon. J. Comput. Phys. **345**, 308–329 (2017)
28. Klopfer, G.H., Yee, H.C.: Viscous hypersonic shock-on-shock interaction on blunt cowl lips. In: AIAA Paper 88–0233 (1988)
29. Anderson Jr., J.D.: Hypersonic and High Temperature Gas Dynamics. AIAA, Reston (2000)
30. Bertin, J.J.: Hypersonic Aerothermodynamics, AIAA Education Series, Washington, DC (1994)
31. Edney, B.: Anomalous Heat Transfer and Pressure Distributions on Blunt Bodies at Hypersonic Speeds in the Presence of an Impinging Shock. Aeronautical Research Institute of Sweden, Stockholm, Sweden, FFA Rept. 115 (1968)
32. Wieting, A.R., Holden, M.S.: Experimental shock-wave interference heating on a cylinder at mach 6 and 8. AIAA J. **27**(11), 1557–1565 (1989)
33. Zhong, X.: Application of essentially nonoscillatory schemes to unsteady hypersonic shock-shock interference heating problems. AIAA J. **32**(8), 1606–1616 (1994)
34. Thareja, R.R., Stewart, J.R., Hassan, O., Morgan, K., Peraire, J.: A point implicit unstructured grid solver for the Euler and Navier-Stokes equations. Int. J. Numer. Methods Fluids. **9**(4), 405–425 (1989)

35. Gnoffo, P.A.: Multi-dimensional. Inviscid flux reconstruction for simulation of hypersonic heating on tetrahedral grids. In: AIAA Paper 2009-599 (2009)
36. Weiss, J.M., Smith, W.A.: Preconditioning applied to variable and constant density flows. AIAA J. **33**(11), 2050–2057 (1995)
37. Turkel, E.: Preconditioning technique in computational fluid dynamics. Annu. Rev. Fluid Mech. **31**, 385–416 (1999)
38. Kitamura, K., Shima, E., Fujimoto, K., Wang, Z.J.: Performance of low-dissipation Euler fluxes and preconditioned LU-SGS at low speeds. Commun. Comput. Phys. **10**(1), 90–119 (2011). https://doi.org/10.4208/cicp.270910.131110a

Chapter 3
Numerical Flux Functions for Ideal Gases

Abstract There are many flux functions available today to obtain the inviscid flux through the cell interface. The idea of treating the cell interface was first proposed by Godunov, who regarded the variable jump there as a Riemann problem. Later, many Godunov-type methods were invented, such as an approximate Riemann solver by Roe, flux vector splitting (FVS) by Steger and Warming or van Leer, its simplified version AUSM (Advection Upstream Splitting Method), and the further modified SLAU (Simple Low-dissipation AUSM) or SLAU2. The Roe flux successfully avoided the iterations required in Godunov's exact Riemann solver with a reasonable approximation of discontinuities with the "Roe average." The FVS's feature is simplicity: it splits waves traveling in the positive (right) and negative (left) directions. Liou further simplified the FVS by treating the mass flux (= convective field) and pressure flux (= acoustic field) separately in AUSM. SLAU is one of its variants extended to low speeds, and SLAU2 greatly enhanced its robustness at high speeds. There is also an HLL (Harten–Lax–van Leer) family which is also popular partly due to its conceptual clarity. In addition, combinations of these methods are, of course, possible. In the following, the flux functions will be explained in two-dimensional forms, unless otherwise stated.

Keywords Riemann solver · Godunov · Roe · Flux vector splitting · HLL (Harten–Lax–van Leer) · HLLE (Harten–Lax–van Leer–Einfeldt) · HLLC (Harten–Lax–van Leer–contact) · AUSM (advection upstream splitting method) · SLAU (simple low-dissipation AUSM) · SLAU2

K. Kitamura, *Advancement of Shock Capturing Computational Fluid Dynamics Methods*, https://doi.org/10.1007/978-981-15-9011-5_3

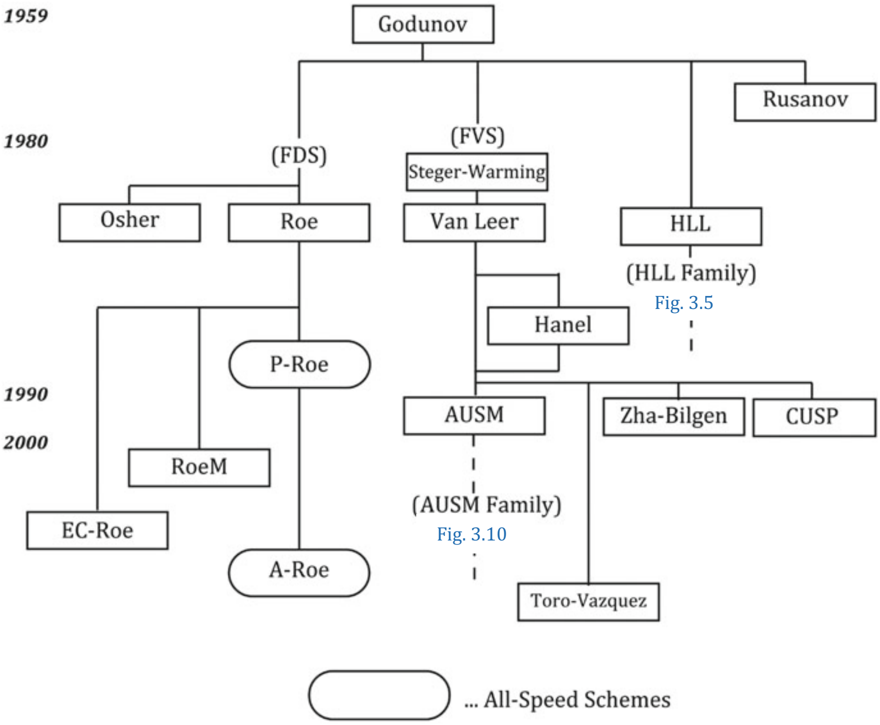

3.1 Godunov's Exact Riemann Solver

Once the cell-interfacial physical values $\mathbf{u}_\mathrm{L}$ and $\mathbf{u}_\mathrm{R}$ are given, their difference is regarded as a discontinuous jump across the interface (a Riemann problem). Figure 3.1 displays the typical situation, in which "shock" and "expansion fan" are interchangeable depending on the left (**L**) and the right (**R**) states (or even "shock

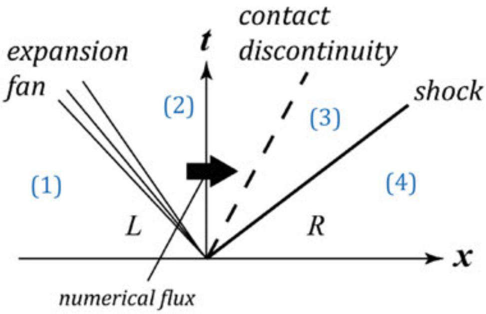

Fig. 3.1 Typical Riemann problem (*x*-*t* diagram)

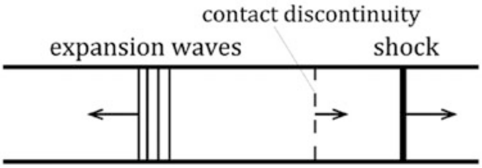

Fig. 3.2 Typical shock tube solution

and shock" or "expansion and expansion"). These left- and right-running waves (= acoustic waves), as well as the contact discontinuity (= entropy wave), separate the domain into four regions. The question here is to which region the cell interface belongs (it lies between the expansion fan and the contact discontinuity in the example of Figs. 3.1 and 3.2). However, the truth is that we do not know this information *a priori*, and it has to be obtained by a flux function.

Godunov's method [1] *exactly* solves this *Riemann problem* based on $\mathbf{Q}_\mathrm{L}$ and $\underline{\mathbf{Q}}_\mathrm{R}$, and finally obtains the numerical flux $\mathbf{F}_{1/2}$ as

$$\mathbf{F}_{1/2(Godunov)} = \mathbf{F}_{Riemann}(x/t, \mathbf{Q}_L, \mathbf{Q}_R) = \mathbf{F}_{Riemann}(0, \mathbf{Q}_L, \mathbf{Q}_R) \tag{3.1}$$

which depends on regions (1)–(4), but these regions depend on the solution. The details can be found in many textbooks, such as [2–5]. Note that Godunov's method obtains the solution by an iterative method (such as Newton iterations), typically requiring a very high computational cost.

3.2 Central Difference Formulas and Lax–Friedrichs (Rusanov) Method

One of the easiest ways of obtaining the numerical flux may be the central difference method. It simply averages the left and the right states arithmetically.

3.2.1 Central Difference Method

$$\mathbf{F}_{1/2(C.D.)} = \frac{1}{2}[\mathbf{F}(\mathbf{Q}_L) + \mathbf{F}(\mathbf{Q}_R)]$$

This form is believed to be the least dissipative method. It is known, however, that it fails to obtain physically reliable solutions (and even diverges) because the travel direction of information is completely neglected. Thus, the common practice is to add a certain amount of dissipation in the form of an extra term D (called the dissipation term), such as Jameson's or MacCormack's artificial dissipation.

Because D is somewhat complicated, we will not go into its detailed formulation; the reader is referred to sect. 22.3 of [4] or to Jameson's review paper [6]).

$$\mathbf{F}_{1/2(C.D.)} = \frac{1}{2}[\mathbf{F}(\mathbf{Q}_L) + \mathbf{F}(\mathbf{Q}_R)] - D \tag{3.2}$$

It is worth noting that this form is common to most of the numerical flux functions introduced in subsequent sections, with differences in the definitions of D.

3.2.2 *Rusanov*

One of the simplest forms for defining the dissipation term D is the Rusanov method (or also known as the local Lax–Friedrichs method) [7].

$$\mathbf{F}_{1/2(Rusanov)} = \frac{1}{2}[\mathbf{F}(\mathbf{Q}_L) + \mathbf{F}(\mathbf{Q}_R)] - \frac{1}{2}|\lambda_{\max}|(\mathbf{Q}_R - \mathbf{Q}_L) \tag{3.3}$$

where "$\lambda_{\max}$" is the maximum characteristic speed, $|u| + a$. Note that compared with Eq. (3.2), the last term corresponds to the dissipation, though its amount is locally controlled by the characteristic speed and the difference in values between the left and right sides. This method is very simple, but very dissipative.

3.3 Flux Difference Splitting (FDS) Methods: Roe's Approximate Riemann Solver (and Entropy Fix) and Osher's Approximate Riemann Solver

3.3.1 *Roe*

3.3.1.1 Original Roe

We have reviewed two opposite extreme methods, that is, Godunov's exact three-wave solver, and Central Difference or Rusanov's very simple treatments. Roe's flux [8] also regards the jumps at cell interfaces as a Riemann problem, but *approximately* linearizes all the three waves. As a result, two shock waves and one entropy wave are assumed as in Fig. 3.3. The numerical flux across the cell interface is then written as

$$\mathbf{F}_{1/2(Roe)} = \frac{1}{2}(\mathbf{F}_L + \mathbf{F}_R) - \frac{1}{2}\widehat{\mathbf{R}}\left|\widehat{\boldsymbol{\Lambda}}\right|\widehat{\mathbf{L}}\boldsymbol{\Delta}\mathbf{Q} \tag{3.4}$$

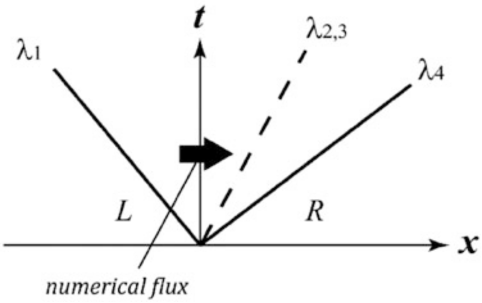

Fig. 3.3 Riemann problem linearly approximated by the Roe flux

where Δ denotes the difference between the left and right states ($\Delta\mathbf{Q} = \mathbf{Q}_R - \mathbf{Q}_L$). $\widehat{\mathbf{R}}$ and $\widehat{\mathbf{L}}$ are the right and left eigenvectors, respectively, of the Jacobian matrix $\widehat{\mathbf{A}}$, which satisfies

$$\Delta\mathbf{F} = \widehat{\mathbf{A}}\Delta\mathbf{Q} \tag{3.5}$$

(^) is called the"Roe average," in which the above equation is valid in both the smooth and discontinuous flow regions, defined as

$$\left.\begin{aligned}
\widehat{\rho} &= \sqrt{\rho_L \rho_R} \\
\widehat{u} &= \frac{\sqrt{\rho_L}u_L + \sqrt{\rho_R}u_R}{\sqrt{\rho_L} + \sqrt{\rho_R}} \\
\widehat{v} &= \frac{\sqrt{\rho_L}v_L + \sqrt{\rho_R}v_R}{\sqrt{\rho_L} + \sqrt{\rho_R}} \\
\widehat{H} &= \frac{\sqrt{\rho_L}H_L + \sqrt{\rho_R}H_R}{\sqrt{\rho_L} + \sqrt{\rho_R}} \\
\widehat{a} &= \sqrt{(\gamma - 1)\left(\widehat{H} - \frac{1}{2}\left(\widehat{u}^2 + \widehat{v}^2\right)\right)}
\end{aligned}\right\} \tag{3.6}$$

where *u* and *v* are assumed normal and tangential to the cell interface, respectively. In 2D, the components of each matrix are

$$\widehat{\mathbf{R}} = \begin{pmatrix} 1 & 1 & 0 & 1 \\ \widehat{u} - \widehat{a} & \widehat{u} & 0 & \widehat{u} + \widehat{a} \\ \widehat{v} & \widehat{v} & 1 & \widehat{v} \\ \widehat{H} - \widehat{u}\widehat{a} & \frac{1}{2}\left(\widehat{u}^2 + \widehat{v}^2\right) & \widehat{v} & \widehat{H} + \widehat{u}\widehat{a} \end{pmatrix} \tag{3.7}$$

$$\left|\widehat{\mathbf{\Lambda}}\right| = diag(|\widehat{u} - \widehat{a}|, |\widehat{u}|, |\widehat{u}|, |\widehat{u} + \widehat{a}|) = diag(|\lambda_1|, |\lambda_2|, |\lambda_3|, |\lambda_4|) \tag{3.7$'$}$$

$$\widehat{\mathbf{L}} = \widehat{\mathbf{R}}^{-1} \tag{3.8}$$

where a is the speed of sound, and λ is the eigenvalue (or characteristic speed, the spectral radius).

3.3.1.2 Roe with Entropy Fix

The Roe approximation enabled us to compute the numerical flux close to the exact solution, at one time (without an iterative method). However, because this method regards even isentropic waves (where physical variables continuously change) as a discontinuous shock, it generates an unphysical "expansion shock" that violates the entropy condition (the second law of thermodynamics). This was a notorious deficiency of the original Roe flux, which was remedied later by Harten [9] and Lin [10] with what came to be known as the entropy fix (or E-fix hereafter). Harten's E-fix is

$$|\lambda_{1,4}| \to 0.5\left({\lambda_{1,4}}^2/\varepsilon_{fix} + \varepsilon_{fix}\right)\ if |\lambda_{1,4}| < \varepsilon_{fix}, \text{where} \varepsilon_{fix} = 0.2 \tag{3.9}$$

That is, it modifies the characteristic speeds corresponding to the acoustic waves (shocks here) when their speeds approach zero. The expansion shock appears when the sound waves $\lambda_{1,4}$ cross the cell interface (the t-axis) in the original Roe, and hence, the above modification effectively hinders its generation.

3.3.1.3 Alternative Expression for Roe Flux

The original form of the Roe flux appears to require an expensive matrix computation. In the actual coding, however, it is avoided by using the following alternative expression [11]:

$$\widehat{\mathbf{R}}\left|\widehat{\Lambda}\right|\widehat{\mathbf{L}}\boldsymbol{\Delta}\mathbf{Q} = \left|\widehat{\lambda}_1\right|\boldsymbol{\Delta}\mathbf{Q} + \delta_1\widehat{\mathbf{Q}}^* + \delta_2\mathbf{N} \tag{3.10}$$

where

$$\left.\begin{aligned}
\widehat{\mathbf{Q}}^{*} &= (1 \quad u \quad v \quad H)^{T} \\
\mathbf{N} &= (0 \quad 1 \quad 0 \quad u)^{T} \\
\boldsymbol{\Lambda} &= diag(\lambda_1, \quad \lambda_2, \quad \lambda_3, \quad \lambda_4) \\
\delta_1 &= (\lambda^{+} \cdot (\Delta p/\widehat{a}) + \lambda^{-} \cdot \widehat{\rho}\Delta u)/\widehat{a} \\
\delta_2 &= \lambda^{+} \cdot \widehat{\rho}\Delta u + \lambda^{-} \cdot (\Delta p/\widehat{a}) \\
\lambda^{+} &= -\left|\widehat{\lambda}_{2,3}\right| + \frac{\left|\widehat{\lambda}_4\right| + \left|\widehat{\lambda}_1\right|}{2}, \quad \lambda^{-} = \frac{\left|\widehat{\lambda}_4\right| - \left|\widehat{\lambda}_1\right|}{2}
\end{aligned}\right\} \tag{3.11}$$

$$\lambda_{2,3} = u, \lambda_4 = u + a, \lambda_1 = u - a \tag{3.12}$$

The mass flux (first row of $\mathbf{F}_{1/2}$), for example, is written as follows:

$$\begin{aligned}
\dot{m}_{1/2} = &\frac{1}{2} \\
&\times \left(\rho_L u_L + \rho_R u_R - |\widehat{u}|\Delta\rho - \frac{\left|\widehat{M}+1\right| + \left|\widehat{M}-1\right| - 2\left|\widehat{M}\right|}{2} \cdot \frac{\Delta p}{\widehat{a}} - \frac{\left|\widehat{M}+1\right| - \left|\widehat{M}-1\right|}{2} \cdot \widehat{\rho}\Delta u \right)
\end{aligned} \tag{3.13}$$

It can be clearly seen that this expression does not require a matrix computation.

3.3.1.4 Preconditioned Roe

When the time-derivative preconditioning [12, 13] (originally proposed to solve the stiffness problem) is conducted, the characteristic speeds are virtually scaled down to the local speed order. This means that the characteristic speeds used in the numerical flux (typically in its dissipation term, such as the last term of Eq. (3.4)) should also be scaled in the same manner, as a side effect of the preconditioning; otherwise, the computation (i.e., preconditioned LU-SGS + original Roe) soon diverges [14] due to the excessively large dissipation. Take the Roe flux, for instance,

$$\mathbf{F}_{1/2(P-Roe)} = \frac{1}{2}(\mathbf{F}_L + \mathbf{F}_R) - \frac{1}{2}\boldsymbol{\Gamma}^{-1}\widehat{\mathbf{R}}\left|\widehat{\boldsymbol{\Lambda}}\right|\widehat{\mathbf{L}}\Delta\mathbf{Q} \tag{3.14}$$

$$\boldsymbol{\Gamma}^{-1}\widehat{\mathbf{R}}\left|\widehat{\Lambda}\right|\widehat{\mathbf{L}}\Delta\mathbf{Q} = \left|\widehat{\lambda}_1\right|\Delta\mathbf{Q} + \delta_1'\widehat{\mathbf{Q}}^{*} + \delta_2'\mathbf{N} \tag{3.15}$$

where

$$\left.\begin{aligned}
\widehat{\mathbf{Q}}^{*} &= \begin{pmatrix} 1 & u & v & H \end{pmatrix}^{T} \\
\mathbf{N} &= \begin{pmatrix} 0 & 1 & 0 & u \end{pmatrix}^{T} \\
\mathbf{\Gamma}^{-1}\mathbf{\Lambda} &= diag\left(\lambda'_1, \quad \lambda_2, \quad \lambda_3, \quad \lambda'_4\right) \\
\delta'_1 &= \left[\frac{\left|\widehat{\lambda'_4}\right| + \left|\widehat{\lambda'_1}\right|}{2} - \varepsilon|u| - \frac{1-\varepsilon}{2}\cdot\frac{\left|\widehat{\lambda'_4}\right| - \left|\widehat{\lambda'_1}\right|}{2}\cdot\frac{u}{\widehat{a'}}\right]\cdot\frac{\Delta p}{\varepsilon\widehat{a}} + \frac{\left|\widehat{\lambda'_4}\right| - \left|\widehat{\lambda'_1}\right|}{2}\cdot\frac{\widehat{\rho}\Delta u}{\widehat{a'}} \\
\delta'_2 &= \left[\frac{\left|\widehat{\lambda'_4}\right| + \left|\widehat{\lambda'_1}\right|}{2} - |u| + \frac{1-\varepsilon}{2}\cdot\frac{\left|\widehat{\lambda'_4}\right| - \left|\widehat{\lambda'_1}\right|}{2}\cdot\frac{u}{\widehat{a'}}\right]\cdot\widehat{\rho}\Delta u + \frac{\left|\widehat{\lambda'_4}\right| - \left|\widehat{\lambda'_1}\right|}{2}\cdot\frac{\Delta p}{\widehat{a'}}
\end{aligned}\right\} \tag{3.16}$$

$$\lambda_{2,3} = u, \lambda'_{1,4} = u' \mp a' = \frac{1}{2}\left\{(1+\varepsilon)|u| \mp \sqrt{(\varepsilon-1)^2u^2 + 4\varepsilon a^2}\right\} \tag{3.17}$$

with

$$\varepsilon = \min\left(1, \max\left(KM^2, {M_{\mathrm{co}}}^2\right)\right) \tag{3.18}$$

where

- a' is the scaled speed of sound, having a local velocity order.
- K is taken as $O(1)$, and M_{co} is the cutoff Mach number, which is typically set as the free-stream Mach number M_∞, leading to $\varepsilon = \min(1, \max(M^2, {M_\infty}^2))$.
- The above expression is borrowed from a preconditioning matrix $\mathbf{\Gamma}$ so that the resulting flux formula has all the eigenvalues scaled from the order of the speed of sound to that of the local fluid velocity at low speeds.
- We do not require the complete form of $\mathbf{\Gamma}$, because the above $\mathbf{\Gamma}^{-1}\mathbf{\Lambda}$ operation is adequate.

Note that at supersonic speeds ($\max(M^2, {M_\infty}^2) > 1.0$), ε is unity and the original Roe flux is recovered; otherwise, even at a moderate speed (e.g., $M = 0.5$), the eigenvalues are no longer the same as those in Eq. (3.7), and the resulting flux is expected to behave differently from an unpreconditioned Roe flux. This aspect of the preconditioning has rarely been investigated [14]. There are other all-speed type Roe methods, such as All-Speed-Roe (A-Roe in Table 2.3) [15].

As a result, its combination with the time-derivative preconditioning (i.e., preconditioned LU-SGS + preconditioned Roe (denoted as "P-Roe")) achieves (i) fast convergence in a realistic time, and (ii) a stable and reliable solution at low speeds, say, Mach 0.1 or smaller. Furthermore, after preconditioned Roe, various preconditioned (in other words, dissipation-controlled) flux functions such as AUSM$^+$-up or SLAU(2) were proposed. Naturally, they can be used with time-derivative preconditioning for low-speed flows (e.g., preconditioned LU-SGS + SLAU2), but they can also be used for moderate- or high-speed flows without the preconditioning (e.g., the original LU-SGS + SLAU2).

3.3.2 Osher

Osher and Chakravarthy [16] developed another approach for the system of Euler equations, based on Engquist–Osher's scheme for scalar conservation laws [17]:

$$\begin{aligned}\mathbf{F}_{1/2(Osher)} &= \frac{1}{2}(\mathbf{F}_L + \mathbf{F}_R) - \frac{1}{2}\int_{\mathbf{Q}_L}^{\mathbf{Q}_R} |\mathbf{A}(\mathbf{Q})| d\mathbf{Q} \\ &= \frac{1}{2}(\mathbf{F}_L + \mathbf{F}_R) - \frac{1}{2}\sum_j \int_{\Gamma(j)} |\lambda_{(j)}| r^{(j)} dw\end{aligned} \tag{3.19}$$

where

$$\mathbf{A}(\mathbf{Q}) = \frac{\partial \mathbf{F}}{\partial \mathbf{Q}} \tag{3.20}$$

is the Jacobian matrix, $\Gamma_{(j)}$ is the subpath along which the integral is evaluated, $\lambda_{(j)}$ is the eigenvalue, $r^{(j)}$ is the right eigenvector, and w is the characteristic variable. In Osher's flux, the phase space from L to R is subdivided into simple wave subpaths: from the path associated with $\lambda = u - a$, then u, and to $u + a$ (Fig. 3.3). Please see Hirsch [2], Toro [3], or the original paper [16] for a more detailed explanation.

These Roe's and Osher's methods are called FDS, in which the numerical flux is computed based on all the three waves according to the variable differences at the cell interface.

3.4 FVS Methods: Steger–Warming, van Leer, Hänel, Liou–Steffen (Original AUSM), Zha–Bilgen, and Toro–Vazquez

On the other hand, in the FVS methods, the flux vector **F** at the cell interface is simply split into components with positive and negative directions, $\mathbf{F}^+$ and $\mathbf{F}^-$ [18]. The advantage of this is the cheap computational cost, but on the other hand, in general they have a large numerical dissipation due to the absence of the entropy wave. They will be briefly reviewed here; detailed explanations can be found in the literature, such as Chap. 20 of Hirsch [2] or Chap. 18 of Laney [4].

3.4.1 Steger–Warming

The basic concept of FVS is to split fluxes into“positive” (corresponding to positive eigenvalues, i.e., the flux vector from left to right) and“negative” (corresponding to negative eigenvalues, i.e., the flux vector from right to left) as

$$\mathbf{F}_{1/2(SW)} = \begin{cases} \mathbf{F}_L & \mathit{if}\ M > 1 \\ \mathbf{F}^+_{SW} + \mathbf{F}^-_{SW} & \mathit{if} |M| \le 1 \\ \mathbf{F}_R & \mathit{if}\ M < -1 \end{cases} \tag{3.21}$$

where $M = u/a$. For $M > 1$, for instance, the smallest eigenvalue $(u - a)$ is positive, and hence all the fluxes are simply convected from left to right ($\mathbf{F}_{1/2(SW)} = \mathbf{F}_L$). Similarly, $\mathbf{F}_{1/2(SW)} = \mathbf{F}_R$ if $M < -1$. In 1D form, for $0 < M \le 1$,

$$\begin{gathered}
\mathbf{F}^+_{SW} = \frac{\rho a}{2\gamma}(M+1)\begin{bmatrix} 1 \\ a(M+1) \\ \dfrac{a^2}{\gamma-1}\left\{1-(\gamma-1)M+\dfrac{\gamma-1}{2}M^2\right\} \end{bmatrix} + \frac{\gamma-1}{\gamma}\rho u \begin{bmatrix} 1 \\ u \\ \dfrac{u^2}{2} \end{bmatrix} \\
\mathbf{F}^-_{SW} = \frac{\rho a}{2\gamma}(M-1)\begin{bmatrix} 1 \\ a(M-1) \\ \dfrac{a^2}{\gamma-1}\left\{1-(\gamma-1)M+\dfrac{\gamma-1}{2}M^2\right\} \end{bmatrix}
\end{gathered} \tag{3.22}$$

and for $-1 \le M \le 0$,

$$\begin{gathered}
\mathbf{F}^+_{SW} = \frac{\rho a}{2\gamma}(M+1)\begin{bmatrix} 1 \\ a(M+1) \\ \dfrac{a^2}{\gamma-1}\left\{1-(\gamma-1)M+\dfrac{\gamma-1}{2}M^2\right\} \end{bmatrix} \\
\mathbf{F}^-_{SW} = \frac{\rho a}{2\gamma}(M-1)\begin{bmatrix} 1 \\ a(M-1) \\ \dfrac{a^2}{\gamma-1}\left\{1-(\gamma-1)M+\dfrac{\gamma-1}{2}M^2\right\} \end{bmatrix} + \frac{\gamma-1}{\gamma}\rho u \begin{bmatrix} 1 \\ u \\ \dfrac{u^2}{2} \end{bmatrix}
\end{gathered} \tag{3.23}$$

This flux encounters solution difficulties due to non-differentiability at sonic points, i.e., $M = 0, \pm 1$.

3.4.2 van Leer

Therefore, van Leer formulated the following differentiable FVS [19] (in 1D form):

$$\mathbf{F}_{1/2(VL)} = \begin{cases} \mathbf{F}_L & \textit{if } M > 1 \\ \mathbf{F}_{VL}^{+} + \mathbf{F}_{VL}^{-} & \textit{if} |M| \le 1 \\ \mathbf{F}_R & \textit{if } M < -1 \end{cases} \tag{3.24}$$

$$\mathbf{F}_{VL}^{\pm} = \pm \frac{\rho a}{4} (M \pm 1)^2 \begin{bmatrix} 1 \\ \frac{2a}{\gamma} \left\{ \pm 1 + \frac{\gamma - 1}{2} M \right\} \\ \frac{2a^2}{\gamma^2 - 1} \left\{ 1 \pm \frac{\gamma - 1}{2} M \right\}^2 \end{bmatrix} \tag{3.25}$$

where $M = u/a$. This is simpler and known to be robust, for instance, against the carbuncle. However, this flux is also known to be diffusive, due to its FVS nature of ignoring the contact discontinuity. In viscous simulations, therefore, the boundary layer is poorly resolved.

3.4.3 Hänel

This is a variant of van Leer's FVS, but it preserves the total enthalpy (H) even across the shock [20] (in 1D form):

$$\mathbf{F}_{1/2(Hanel)} = \begin{cases} \mathbf{F}_L & \textit{if } M > 1 \\ \mathbf{F}_{Hanel}^{+} + \mathbf{F}_{Hanel}^{-} & \textit{if} |M| \le 1 \\ \mathbf{F}_R & \textit{if } M < -1 \end{cases} \tag{3.26}$$

$$\mathbf{F}_{Hänel}^{\pm} = \pm \frac{\rho a}{4} (M \pm 1)^2 \begin{bmatrix} 1 \\ \frac{2a}{\gamma} \left\{ \pm 1 + \frac{\gamma - 1}{2} M \right\} \\ H \end{bmatrix} \tag{3.27}$$

where $M = u/a$. Note that only the last row is modified from van Leer's FVS.

3.4.4 Liou–Steffen (Original AUSM)

This is a much simpler FVS. The key idea is that the numerical flux is split into the "mass flux" and "pressure flux" in AUSM (Advection Upstream Splitting Method, pronounced "awesome"), in which the former corresponds to the velocity field and the latter to the acoustic field.

According to [21], there are two variants of the AUSM: AUSM "M-splitting" and "U-splitting." In the original paper of AUSM [22], only "M-splitting" was proposed as AUSM; but a little later, "U-splitting" was introduced [21].

3.4.4.1 AUSM (M-Splitting)

$$\mathbf{F}_{1/2(AUSM-M)} = M_{1/2}\widetilde{\boldsymbol{\Psi}}_{L/R} + \mathbf{P} \tag{3.28}$$

$$\widetilde{\boldsymbol{\Psi}} = (\rho a, \rho a u, \rho a v, \rho a H)^T, \mathbf{P} = \left(0, p_{1/2}, 0, 0\right)^T \tag{3.29}$$

where the subscript "L/R" means that it is "L" (left-side value) if $M_{1/2} > 0$ and "R" (right-side value) otherwise [21]. Thus, it is also written as

$$\mathbf{F}_{1/2(AUSM-M)} = \frac{M_{1/2} + \left|M_{1/2}\right|}{2}\widetilde{\boldsymbol{\Psi}}_L + \frac{M_{1/2} - \left|M_{1/2}\right|}{2}\widetilde{\boldsymbol{\Psi}}_R + \mathbf{P} \tag{3.30}$$

The first term of (3.28) [or the first two terms of (3.30)] on the right-hand side (R.H.S.) is called the *mass flux* conveyed by the velocity, whereas the second term corresponds to the *pressure flux* governed by acoustic waves. These fluxes are computed by differentiable polynomials as follows:

$$M_{1/2} = \mathrm{M}^+ + \mathrm{M}^- \tag{3.31}$$

$$\mathrm{M}^\pm = \begin{cases} \frac{1}{2}(M \pm |M|), & if|M| \geq 1 \\ \pm\frac{1}{4}(M \pm 1)^2, & otherwise \end{cases} \tag{3.32}$$

$$p_{1/2} = \mathrm{P}^+ \cdot p_L + \mathrm{P}^- \cdot p_R \tag{3.33}$$

$$\mathrm{P}^\pm = \begin{cases} \frac{1}{2}(1 \pm sign(M)), & if|M| \geq 1 \\ \frac{1}{4}(M \pm 1)^2(2 \mp M), & otherwise \end{cases} \tag{3.34}$$

where "+" refers to the "plus sign" in Eq. (3.32) and also stands for the "left" state traveling in the positive direction (from left to right), whereas "−" is the "minus sign" in Eq. (3.32) and also denotes the "right" state in the negative direction (from right to left). The mass flux splitting function $\mathrm{M}^{\pm}$ is borrowed from van Leer's. This AUSM has a very simple structure, yet is more robust than Roe against the carbuncle. It is also noteworthy that this flux function preserves a stationary contact discontinuity because $M_{1/2} = (M_L + 1)^2/4 - (M_R - 1)^2/4 = 0$ and no mass flux passes through the cell interface if $M_\mathrm{L} = M_\mathrm{R} = 0$ [21].

3.4.4.2 AUSM (U-Splitting)

$$\mathbf{F}_{1/2(AUSM-U)} = \frac{u_{1/2} + |u_{1/2}|}{2}\mathbf{\Phi}_L + \frac{u_{1/2} - |u_{1/2}|}{2}\mathbf{\Phi}_R + \mathbf{P} \tag{3.35}$$

$$\mathbf{\Phi} = (\rho, \rho u, \rho v, \rho H)^T, \mathbf{P} = \left(0, p_{1/2}, 0, 0\right)^T \tag{3.36}$$

$$u_{1/2} = \mathrm{U}^{+} + \mathrm{U}^{-} \tag{3.37}$$

$$\mathrm{U}^{\pm} = \begin{cases} \frac{1}{2}(M \pm |M|)a, & \mathit{if}|M| \geq 1 \\ \pm\frac{1}{4}(M \pm 1)^2 a, & \mathit{otherwise} \end{cases} \tag{3.38}$$

According to [21], U-splitting suppresses the numerical oscillations that appear at discontinuities in M-splitting, at the expense of contact discontinuity preservation ($u_{1/2} \neq 0$ if $u_\mathrm{L} = u_\mathrm{R} = 0$) [23]. As Wada and Liou have pointed out [23], these two variants can be unified if the common speed of sound is used for a_L and a_R (see Sect. 3.6.1).

3.4.5 *Zha–Bilgen*

This flux is also a type of FVS but features its splitting concept [24]. In this flux, the pressure in the energy equation is excluded from the mass flux and inserted into the pressure flux:

$$\mathbf{F}_{1/2(ZB)} = \frac{u_{1/2} + |u_{1/2}|}{2}\mathbf{\Phi}_{L(ZB)} + \frac{u_{1/2} - |u_{1/2}|}{2}\mathbf{\Phi}_{R(ZB)} + \mathbf{P}_{(ZB)} \tag{3.39}$$

$$\mathbf{\Phi}_{(ZB)} = (\rho, \rho u, \rho v, \rho E)^T, \mathbf{P}_{(ZB)} = \left(0, p_{1/2}, 0, (pu)_{1/2}\right)^T \tag{3.40}$$

$$u_{1/2} = \mathrm{U}^{+} + \mathrm{U}^{-} \tag{3.41}$$

$$\mathrm{U}^{\pm} = \begin{cases} \frac{1}{2}(M \pm |M|)a, & \mathit{if} |M| \geq 1 \\ \pm\frac{1}{4}(M \pm 1)^2 a, & \mathit{otherwise} \end{cases} \tag{3.42}$$

$$p_{1/2} = \mathrm{P}^{+} \cdot p_L + \mathrm{P}^{-} \cdot p_R \tag{3.43}$$

$$\mathrm{P}^{\pm} = \begin{cases} \frac{1}{2}(1 \pm \mathit{sign}(M)), & \mathit{if} |M| \geq 1 \\ \frac{1}{4}(M \pm 1)^2 (2 \mp M), & \mathit{otherwise} \end{cases} \tag{3.44}$$

as in AUSM, and (pu) is given as

$$(pu)_{1/2} = (\mathrm{PU})^{+} \cdot p_L + (\mathrm{PU})^{-} \cdot p_R \tag{3.45}$$

$$(\mathrm{PU})^{\pm} = \begin{cases} \frac{u}{2}(1 \pm \mathit{sign}(M)), & \mathit{if} |M| \geq 1 \\ \frac{1}{2}(u \pm a), & \mathit{otherwise} \end{cases} \tag{3.46}$$

3.4.6 Toro–Vázquez

Toro and Vázquez-Cendón further moved the pressure in the mass flux (as a form of internal energy) to the pressure flux, so that only the kinetic energy remained in the mass flux of the energy equation [25]:

$$\mathbf{F}_{1/2(TV)} = \frac{u^*_{1/2} + \left|u^*_{1/2}\right|}{2} \mathbf{\Phi}_{L(TV)} + \frac{u^*_{1/2} - \left|u^*_{1/2}\right|}{2} \mathbf{\Phi}_{R(TV)} + \mathbf{P}_{(TV)} \tag{3.47}$$

$$\mathbf{\Phi}_{(TV)} = \left(\rho, \rho u, \rho v, \frac{1}{2}\rho\left(u^2 + v^2\right)\right)^T, \mathbf{P}_{(TV)} = p^*_{1/2} \cdot \left(0, 1, 0, \frac{\gamma}{\gamma - 1} u^*_{1/2}\right)^T \tag{3.48}$$

$$u^*_{1/2} = \frac{\rho_R(u_R + A_R)u_R - \rho_L(u_L - A_L)u_L - 2(p_R - p_L)}{\rho_R(u_R + A_R) - \rho_L(u_L - A_L)} \tag{3.49}$$

$$\begin{aligned} p^*_{1/2} = & \frac{\rho_R(u_R + A_R)p_L - \rho_L(u_L - A_L)p_R}{\rho_R(u_R + A_R) - \rho_L(u_L - A_L)} \\ & + \frac{1}{2}\frac{\rho_R \rho_L (u_R + A_R)(u_L - A_L)}{\rho_R(u_R + A_R) - \rho_L(u_L - A_L)}(u_R - u_L) \end{aligned} \tag{3.50}$$

$$A = \sqrt{u^2 + 4a^2} \tag{3.51}$$

As can be seen, the *star region* values $u^*{}_{1/2}$ and $p^*{}_{1/2}$ are similar to those in Harten–Lax–van Leer–Contact, HLLC (see Sect. 3.5.4).

The method was developed based on a comparative analysis of the eigenvalues of AUSM (M-splitting) and Zha–Bilgen splittings. The analysis appears informative, but may not be valid inside the numerical shock (where any analytical approach will fail) [26–28].

Other similar FVS-type methods include convective-upwind split-pressure (CUSP) schemes, e.g., E (energy)-CUSP and H (total enthalpy)-CUSP [29]. Interested readers are encouraged to consult the original articles.

3.5 Harten–Lax–van Leer (HLL) Family: HLL, HLLE, HLLEM, HLLC, HLLD, and HLLI

3.5.1 HLL

This flux was named after its developers' names: Harten, Lax, and van Leer [30] (Fig. 3.5). However, there was a "loss of information," not a "loss of contact discontinuity," as claimed by Prof. Bram van Leer at his plenary talk in 2013 ("Four Decades of CFD: Looking Back and Moving Forward—A Symposium Celebrating the Careers of Jameson, Roe and van Leer (JRV Symposium)," June 23, 2013, http://dept.ku.edu/~cfdku/JRV.html). In fact, the HLL (Harten–Lax–van Leer) flux function had two variants: two-wave HLL and three-wave HLL. The former indeed lacks contact resolution, but the latter has it. Nevertheless, only the "two-wave HLL" was later recognized widely as "HLL."

The (two-wave) HLL flux (Fig. 3.6) is simply given by

$$\begin{aligned}\mathbf{F}_{1/2(HLL)} &= \frac{S_R\mathbf{F}_L - S_L\mathbf{F}_R + S_RS_L(\mathbf{Q}_R - \mathbf{Q}_L)}{S_R - S_L} \\ &= \frac{S_R\mathbf{F}_L - S_L\mathbf{F}_R}{S_R - S_L} + \frac{S_RS_L}{S_R - S_L}(\mathbf{Q}_R - \mathbf{Q}_L) \\ &= \frac{1}{2}(\mathbf{F}_L + \mathbf{F}_R) - \frac{1}{2}\frac{S_R + S_L}{S_R - S_L}(\mathbf{F}_R - \mathbf{F}_L) + \frac{S_RS_L}{S_R - S_L}(\mathbf{Q}_R - \mathbf{Q}_L)\end{aligned} \tag{3.52}$$

because of the following (by canceling $\mathbf{Q}^*$):

$$\mathbf{F}_{1/2(HLL)} = \mathbf{F}_L + S_L(\mathbf{Q}^* - \mathbf{Q}_L) \tag{3.53}$$

$$\mathbf{F}_{1/2(HLL)} = \mathbf{F}_R + S_R(\mathbf{Q}^* - \mathbf{Q}_R) \tag{3.54}$$

In addition, by canceling $\mathbf{F}_{1/2}$ from these two equations:

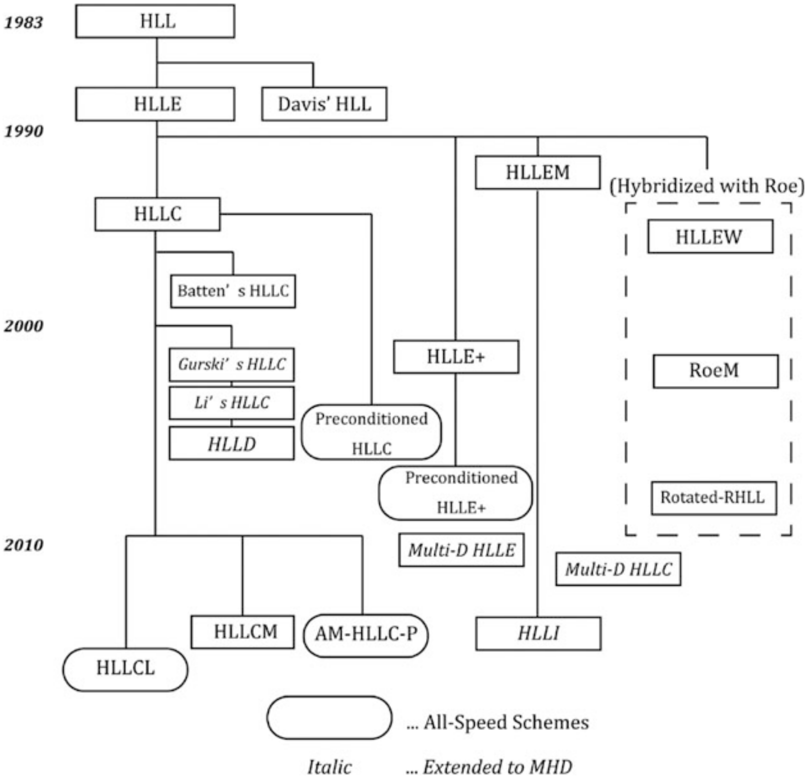

Fig. 3.5 HLL (Harten–Lax–van Leer) family tree

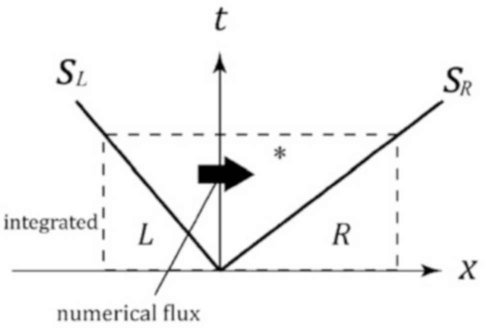

Fig. 3.6 Riemann problem approximated by two-wave HLL

$$\mathbf{Q}^* = \frac{S_R\mathbf{Q}_R - S_L\mathbf{Q}_L - (\mathbf{F}_R - \mathbf{F}_L)}{S_R - S_L} \tag{3.55}$$

As can be seen, the (two-wave) HLL's feature is algorithmic simplicity, although it needs to specify the wave speeds S_L and S_R. To the author, the (S_R-S_L) in the denominator initially looked odd. Such readers, however, may regard it as the weighted average of (S_R) and ($-S_L$), which are both positive.

3.5.2 HLLE

There were ambiguities in the characteristic wave speeds S_L and S_R in HLL. Einfeldt [31] defined them, and this version of HLL is known as HLLE (Harten–Lax–van Leer–Einfeldt).

$$S_L = \min\left(0, \quad u_L - a_L, \quad \widehat{u} - \widehat{a}\right) \tag{3.56}$$

$$S_R = \max\left(0, \quad u_R + a_R, \quad \widehat{u} + \widehat{a}\right) \tag{3.57}$$

These $\widehat{u}$ and $\widehat{a}$ are estimated by the Roe average. Thus, as long as the wave speeds in [31] are employed, the "two-wave HLL" stands for "HLLE."

HLLE is today used as a robust alternate if a contact-resolving flux fails, for instance. Another type of usage is hybridization with the Roe flux, such as HLLEW (HLLE-Wada) by Obayashi and Guruswamy [32], RoeM by Kim et al. [33], and Rotated-Roe-HLL (RHLL) by Nishikawa and Kitamura [34].

3.5.3 HLLEM

After the advent of (two-wave) HLL or HLLE, there were several attempts to recover the entropy wave in HLL. HLLEM (HLLE Modified) by Einfeldt et al. [35] can resolve the contact and boundary layer.

$$\begin{aligned}\mathbf{F}_{1/2(HLLEM)} &= \frac{S_R\mathbf{F}_L - S_L\mathbf{F}_R + S_RS_L(\mathbf{Q}_R - \mathbf{Q}_L)}{S_R - S_L} - \frac{S_RS_L\left(\delta_2\alpha_2\widehat{\mathbf{R}}_2 + \delta_3\alpha_3\widehat{\mathbf{R}}_3\right)}{S_R - S_L} \\ &= \mathbf{F}_{1/2(HLLE)} - \frac{S_RS_L\left(\delta_2\alpha_2\widehat{\mathbf{R}}_2 + \delta_3\alpha_3\widehat{\mathbf{R}}_3\right)}{S_R - S_L}\end{aligned} \tag{3.58}$$

$$\delta_2 = \frac{\widehat{a}}{\widehat{a} + |\overline{u}|} = \delta_3 \tag{3.59}$$

$$\overline{u} = \frac{\max\left(u_R + a_R,\ \ \widehat{u} + \widehat{a}\right) + \min\left(u_L - a_L,\ \ \widehat{u} - \widehat{a}\right)}{2} \tag{3.60}$$

$$\alpha_2 = \widehat{\mathbf{R}}_2^{-1} \cdot \Delta\mathbf{Q}, \alpha_3 = \widehat{\mathbf{R}}_3^{-1} \cdot \Delta\mathbf{Q} \tag{3.61}$$

where $\widehat{\mathbf{R}}_2$ and $\widehat{\mathbf{R}}_3$ are the 2nd and 3rd columns of the eigenmatrix in Eq. (3.6), respectively, and $\widehat{\mathbf{R}}_2^{-1}$ and $\widehat{\mathbf{R}}_3^{-1}$ are the 2nd and 3rd rows of the inverse eigenmatrix. The wave speeds are estimated as in HLLE as

$$S_L = \min\left(0, \quad u_L - a_L, \quad \widehat{u} - \widehat{a}\right) \tag{3.62}$$

$$S_R = \max\left(0, \quad u_R + a_R, \quad \widehat{u} + \widehat{a}\right) \tag{3.63}$$

As pointed out by Einfeldt et al. [35], the HLLEM becomes equivalent to Roe if the smallest and largest eigenvalues of the Roe average matrix are chosen as the wave speeds:

$$S_L = \widehat{u} - \widehat{a} \tag{3.64}$$

$$S_R = \widehat{u} + \widehat{a} \tag{3.65}$$

This modification conferred contact-resolving capability on the HLLE, but the resulting HLLEM is as carbuncle prone as Roe [35]. Nevertheless, interestingly, this HLLEM was recently extended by Balsara et al. to MHD [36], as will be described later.

3.5.4 HLLC

Toro et al. [37] established HLLC (HLL with Contact). In their method, the entropy wave (S_* in Fig. 3.7) is well defined.

The HLLC, which restored this capability from the "two-wave" HLL, is obviously a three-wave solver and has become popular. Nevertheless, it has many variants that differ in the way the contact (the "middle zone" or "star region" between the left and right states) is expressed. The wave speeds can be defined based on the Roe average, arithmetic average, or Batten's choice [38], etc. See [3] for those details.

The values in the *star region* are estimated by the integral of the region in Fig. 3.7. For instance, the normal component of the velocity is

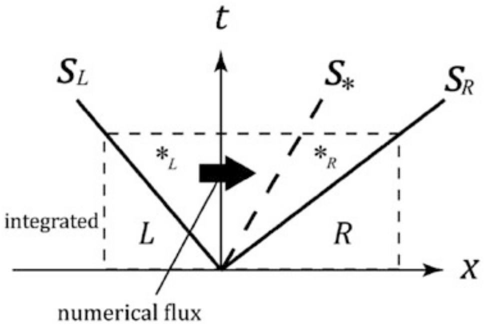

Fig. 3.7 Riemann problem approximated by HLLC

$$S_* = u^* = \frac{p_L - p_R + \rho_L u_L(S_L - u_L) - \rho_R u_R(S_R - u_R)}{\rho_L(S_L - u_L) - \rho_R(S_R - u_R)} \tag{3.66}$$

Because the tangential velocity is unaffected by the shock,

$$v_L^* = v_L, v_R^* = v_R \tag{3.67}$$

and the star region pressure is expressed as

$$\begin{aligned} p_* = p_L^* &= p_L + \rho_L(S_L - u_L)(S_* - u_L) \\ = p_R^* &= p_R + \rho_R(S_R - u_R)(S_* - u_R) \end{aligned} \tag{3.68}$$

although we do not necessarily need p_*, at least for the following flux computation:

$$\mathbf{F}_{1/2(HLLC)} = \begin{cases} \mathbf{F}_L + S_L(\mathbf{Q}_L^* - \mathbf{Q}_L) & \text{if } S_* \geq 0 \\ \mathbf{F}_R + S_R(\mathbf{Q}_R^* - \mathbf{Q}_R) & \text{if } S_* < 0 \end{cases} \tag{3.69}$$

or equivalently,

$$\begin{aligned} \mathbf{F}_{1/2(HLLC)} = {} & \left[\mathbf{F}_L + S_L(\mathbf{Q}_L^* - \mathbf{Q}_L)\right] \frac{S_* + |S_*|}{2S_*} + \left[\mathbf{F}_R + S_R(\mathbf{Q}_R^* - \mathbf{Q}_R)\right] \\ & \times \frac{S_* - |S_*|}{2S_*} \end{aligned} \tag{3.70}$$

where

$$\mathbf{Q}^{*}_{L/R}=\begin{bmatrix}\left(q^{*}_{L/R}\right)_{1}\\\left(q^{*}_{L/R}\right)_{2}\\\left(q^{*}_{L/R}\right)_{3}\\\left(q^{*}_{L/R}\right)_{4}\end{bmatrix}$$

$$=\begin{bmatrix}\rho_{L/R}\left(S_{L/R}-u_{L/R}\right)/\left(S_{L/R}-S_{*}\right)\\\left(q^{*}_{L/R}\right)_{1}\cdot S_{*}\\\left(q^{*}_{L/R}\right)_{1}\cdot v_{L/R}\\\left(q^{*}_{L/R}\right)_{1}\cdot\left\{\left(e_{L/R}/\rho_{L/R}\right)+\left(S_{*}-u_{L/R}\right)\right\}\cdot\left\{S_{*}+\left(\rho_{L/R}/\rho_{L/R}/\left(S_{L/R}-u_{L/R}\right)\right)\right\}\end{bmatrix}\tag{3.71}$$

Owing to its conceptual and mathematical simplicity, HLLC is widely used in many flow simulations. Further comments follow:

- As with HLLEM, it is as prone to the carbuncle as Roe.
- A comparative study was conducted in [39].
- There are further variants such as HLLE+ [40] and all-speed HLLC [41].
- It is expressed in an AUSM-like manner and extended to all-speed in [42].

Among the many flux functions available today, this HLLC [37] is one of the popular methods for the following reasons:

1. It reasonably recognizes the middle zone (p^{*} and u^{*} in Fig. 3.7), including a contact discontinuity, separated by the left and right-running waves (accurate).
2. It requires no iterations (simple), as opposed to the Godunov's exact Riemann solver.
3. It can be extended to low-speed flow problems by controlling the dissipation.

3.5.5 HLLD

This method [43] is a five-wave extended version of HLLC for magnetohydrodynamics (MHD), *not* for gas dynamics. Nevertheless, the author believed it was important to introduce this flux here, because of its rational design concept and popularity in MHD (Sect. 4.3). In MHD, there are seven waves (left fast wave, left Alfvén wave, left slow wave, entropy wave, right slow wave, right Alfvén wave, and right fast wave) to be treated in the Riemann problem, as opposed to three waves in gas dynamics. Among these seven, Miyoshi and Kusano [43] designed HLLD (HLL

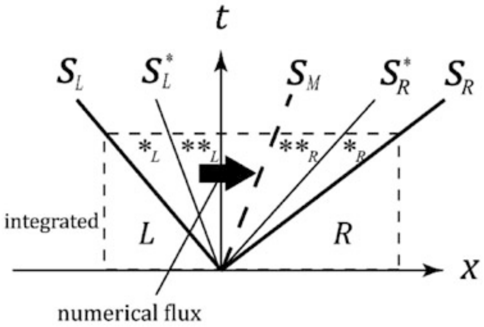

Fig. 3.8 Riemann problem approximated by HLLD

with Discontinuities) to resolve five important waves (the two slow waves were neglected): The fastest wave speeds S_L and S_R are given by the fast waves; the Alfvén speeds (corresponding to acoustic speeds in gas dynamics) are $S^*{}_L$ and $S^*{}_R$; the entropy wave is S_M (Fig. 3.8).

The S_M in HLLD is obtained in the same way as the S_* in HLLC, as long as p is replaced with the global (or total) pressure p_G (or p_T) = $p + 0.5\mathbf{B}^2$ = (gas pressure) + (magnetic pressure).

$$S_M = \frac{-p_{T,L} + p_{T,R} + \rho_L u_{n,L}(S_L - u_{n,L}) - \rho_R u_{n,R}(S_R - u_{n,R})}{\rho_L(S_L - u_{n,L}) - \rho_R(S_R - u_{n,R})} \tag{3.72}$$

$$u^*_{n,L} = u^{**}_{n,L} = u^{**}_{n,R} = u^*_{n,R} = S_M \tag{3.73}$$

$$p^*_T = p^*_{T,L} = p^{**}_{T,L} = p^{**}_{T,R} = p^*_{T,R}$$
$$= \frac{\rho_R(S_R - u_{n,R})p_{T,L} - \rho_L(S_L - u_{n,L})p_{T,R} + \rho_L\rho_R(S_L - u_{n,L})(S_R - u_{n,R})(u_{n,R} - u_{n,L})}{\rho_R(S_R - u_{n,R}) - \rho_L(S_L - u_{n,L})} \tag{3.74}$$

where

$$u^*_{t,L/R} = u_{t,L/R} - B_n B_{t,L/R}\frac{S_M - u_{n,L/R}}{\rho_{L/R}\left(S_{L/R} - u_{n,L/R}\right)\left(S_{L/R} - S_M\right) - B_n^2} \tag{3.75}$$

$$B^*_{t,L/R} = B_{t,L/R}\frac{\rho_{L/R}\left(S_{L/R} - u_{n,L/R}\right)^2 - B_n^2}{\rho_{L/R}\left(S_{L/R} - u_{n,L/R}\right)\left(S_{L/R} - S_M\right) - B_n^2} \tag{3.76}$$

$$e^*_{L/R} = \frac{\left(S_{L/R} - u_{n,L/R}\right)e_{L/R} - p_{T,L/R}u_{n,L/R} + p^*_T S_M + B_n\left(\mathbf{u}_{L/R}\cdot\mathbf{B}_{L/R} - \mathbf{u}^*_{L/R}\cdot\mathbf{B}^*_{L/R}\right)}{S_{L/R} - S_M} \tag{3.77}$$

where the subscripts n and t are the cell-normal and two tangential components, respectively. Furthermore, according to the jump condition,

$$\rho^{**}_{L/R} = \rho^{*}_{L/R} = \rho_{L/R}\frac{S_{L/R} - u_{n,L/R}}{S_{L/R} - S_M} \tag{3.78}$$

$$S^{*}_{L/R} = S_M \mp \frac{|B_n|}{\sqrt{\rho^{*}_{L/R}}} \tag{3.79}$$

$$u^{**}_{t,L} = u^{**}_{t,R} \equiv u^{**}_{t} = \frac{\sqrt{\rho^{*}_{L}}u^{*}_{t,L} + \sqrt{\rho^{*}_{R}}u^{*}_{t,R} + \left(B^{*}_{t,R} - B^{*}_{t,L}\right)sign(B_n)}{\sqrt{\rho^{*}_{L}} + \sqrt{\rho^{*}_{R}}} \tag{3.80}$$

$$B^{**}_{t,L} = B^{**}_{t,R} \equiv B^{**}_{t} = \frac{\sqrt{\rho^{*}_{L}}B^{*}_{t,R} + \sqrt{\rho^{*}_{R}}B^{*}_{t,L} + \sqrt{\rho^{*}_{L}\rho^{*}_{R}}\left(u^{*}_{t,R} - u^{*}_{t,L}\right)sign(B_n)}{\sqrt{\rho^{*}_{L}} + \sqrt{\rho^{*}_{R}}} \tag{3.81}$$

$$e^{**}_{L/R} = e^{*}_{L/R} \mp \sqrt{\rho^{*}_{L/R}}\left(\mathbf{u}^{*}_{L/R}\cdot\mathbf{B}^{*}_{L/R} - \mathbf{u}^{**}_{L/R}\cdot\mathbf{B}^{**}_{L/R}\right)sign(B_n) \tag{3.82}$$

where $|\mathbf{B}| = \sqrt{B_x^2 + B_y^2 + B_z^2}$.

3.5.6 HLLI

By extending HLLEM, Dumbser and Balsara [36] proposed HLLI (HLL with Intermediate waves) in an attempt to resolve intermediate waves both in gas dynamics (three waves) and in MHD (seven waves) (Fig. 3.9):

$$\begin{aligned}\mathbf{F}_{1/2(HLLI)} &= \frac{S_R\mathbf{F}_L - S_L\mathbf{F}_R + S_R S_L(\mathbf{Q}_R - \mathbf{Q}_L)}{S_R - S_L} - \varphi\frac{S_L S_R}{S_R - S_L}\mathbf{R}_*\left(\overline{\mathbf{Q}}\right)\boldsymbol{\delta}_*\left(\overline{\mathbf{Q}}\right)\mathbf{L}_*\left(\overline{\mathbf{Q}}\right)(\mathbf{Q}_R - \mathbf{Q}_L)\\ &= \mathbf{F}_{1/2(HLLE)} - \varphi\frac{S_L S_R}{S_R - S_L}\mathbf{R}_*\left(\overline{\mathbf{Q}}\right)\boldsymbol{\delta}_*\left(\overline{\mathbf{Q}}\right)\mathbf{L}_*\left(\overline{\mathbf{Q}}\right)(\mathbf{Q}_R - \mathbf{Q}_L)\end{aligned} \tag{3.83}$$

$$\boldsymbol{\delta}_*\left(\overline{\mathbf{Q}}\right) = \mathbf{I} - \frac{\boldsymbol{\Lambda}^{-}_{*}}{S_L} - \frac{\boldsymbol{\Lambda}^{+}_{*}}{S_R} \tag{3.84}$$

$$\boldsymbol{\Lambda}^{\pm}_{*} = \frac{1}{2}\left(\boldsymbol{\Lambda}_* \pm |\boldsymbol{\Lambda}_*|\right) \tag{3.85}$$

$$\overline{\mathbf{Q}} = \frac{1}{2}\left(\mathbf{Q}_L + \mathbf{Q}_R\right) \tag{3.86}$$

where the scalar $\varphi \in [0, 1]$ is a flattener variable (whose detailed definition is given in [36]) that responds to the presence of strong shocks (HLL flux for $\varphi = 0$, while HLLI for $\varphi = 1$). In principle, the matrices of the right and left eigenvectors, i.e., $\mathbf{R}_*\left(\overline{\mathbf{Q}}\right)$ and $\mathbf{L}_*\left(\overline{\mathbf{Q}}\right)$, can include the entire MHD eigensystem, which yields a complete Riemann solver. However, if the readers are interested only in improving the contact discontinuity and Alfvén waves, $\mathbf{R}_*\left(\overline{\mathbf{Q}}\right)$ and $\mathbf{L}_*\left(\overline{\mathbf{Q}}\right)$ could contain only the linearly

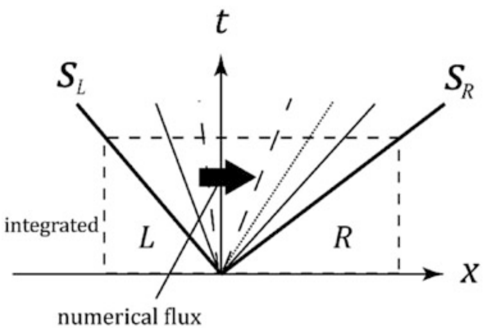

Fig. 3.9 Riemann problem approximated by HLLI

degenerate intermediate right and left eigenvectors so that $\mathbf{\Lambda}_* = \mathbf{\Lambda}_*\left(\overline{\mathbf{Q}}\right)$ is a diagonal matrix of eigenvalues, as detailed in [36].

3.6 Advection Upstream Splitting Method (AUSM) Family: AUSMDV, AUSM+, SHUS, LDFSS, AUSMPW+, AUSM+-up, SLAU, SD-SLAU, SLAU2, and HR-SLAU2

The original AUSM can be regarded as a simpler version of van Leer's FVS. From AUSMD (below), however, the AUSM-family fluxes have developed almost independently of the FVS, although the original idea of splitting the flux into mass flux and pressure flux parts remained. For instance, in AUSMD and later versions, the mass flux part contains "common" speed of sound $a_{1/2}$ between the left and right states, unlike AUSM-M. This is why the original AUSM is excluded from this section in this book. In addition, AUSMD provokes carbuncle-like shock anomalies [23]. Later, many improvements were proposed, such as the "AUSM-family" flux functions (more than 10 variants) as summarized in Fig. 3.10. We shall introduce representative ones below.

3.6.1 AUSMDV

AUSMD (having the FDS nature of contact resolving) and AUSMV (equipped with FVS robustness) are hybridized as AUSMDV based on a pressure gradient, in which the more robust AUSMV is fully used at the detected shock [23].

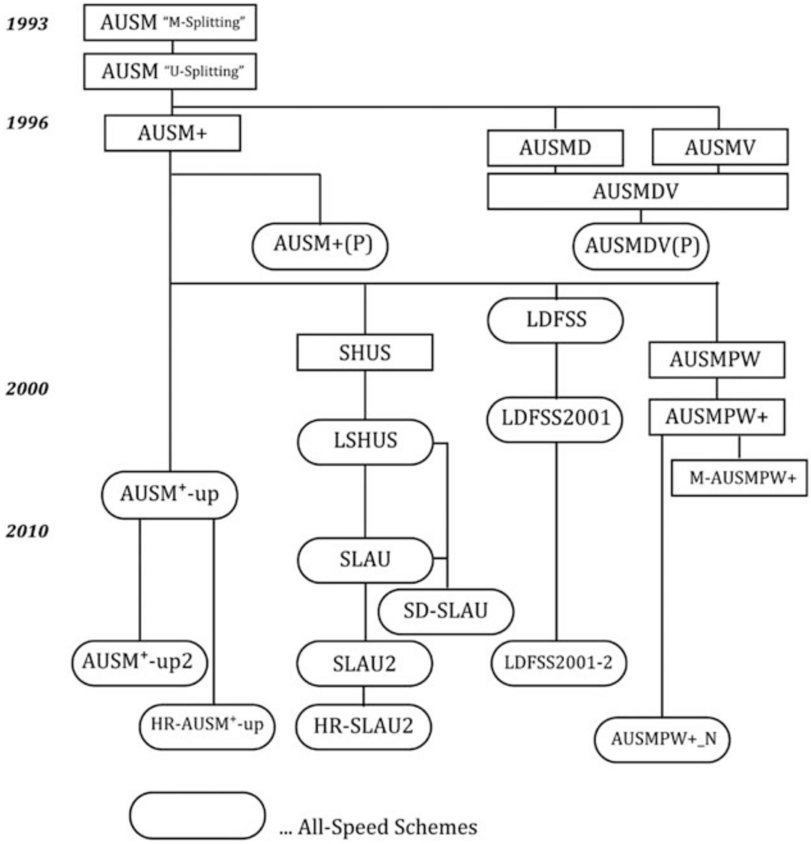

Fig. 3.10 AUSM (Advection Upstream Splitting Method) family tree

3.6.1.1 AUSMD

$$\mathbf{F}_{1/2(AUSMD)} = \frac{\dot{m}_{1/2} + \left|\dot{m}_{1/2}\right|}{2}\mathbf{\Psi}_L + \frac{\dot{m}_{1/2} - \left|\dot{m}_{1/2}\right|}{2}\mathbf{\Psi}_R + \mathbf{P} \tag{3.87}$$

$$\mathbf{\Psi} = (1, u, v, H)^T, \mathbf{P} = \left(0, p_{1/2}, 0, 0\right)^T \tag{3.88}$$

$$\dot{m}_{1/2} = \rho_L \mathrm{U}^+ + \rho_R \mathrm{U}^- \tag{3.89}$$

$$\mathrm{U}^{\pm} = \begin{cases} \dfrac{1}{2}(M \pm |M|)a_{1/2}, & if|M| \geq 1 \\ \pm\dfrac{\alpha^{\pm}}{4}(M \pm 1)^2 a_{1/2} + \dfrac{1-\alpha^{\pm}}{2}(M \pm |M|)a_{1/2}, & otherwise \end{cases} \tag{3.90}$$

$$\alpha^{\pm} = \frac{2(p/\rho)_{L/R}}{(p/\rho)_L + (p/\rho)_R} \tag{3.91}$$

$$a_{1/2} = \max\left(a_L, a_R\right) \tag{3.92}$$

and

$$p_{1/2} = \mathrm{P}^{+} \cdot p_L + \mathrm{P}^{-} \cdot p_R \tag{3.93}$$

$$\mathrm{P}^{\pm} = \begin{cases} \frac{1}{2}(1 \pm sign(M)), & if|M| \geq 1 \\ \frac{1}{4}(M \pm 1)^2(2 \mp M), & otherwise \end{cases} \tag{3.94}$$

Note that the common speed of sound, $a_{1/2}$, is employed at both the "+" and "–" sides. But as with the other FDS, it suffered from the carbuncle problem. Furthermore, AUSMD was extended to two-fluid modeling for multiphase flows by Niu [44].

3.6.1.2 AUSMV

In AUSMV, only the $(\rho u^2)_{1/2}$ term in the normal momentum is changed from

$$\left(\rho u^2\right)_{AUSMD} = \frac{\dot{m}_{1/2} + \left|\dot{m}_{1/2}\right|}{2} u_L + \frac{\dot{m}_{1/2} - \left|\dot{m}_{1/2}\right|}{2} u_R \tag{3.95}$$

to

$$\left(\rho u^2\right)_{AUSMV} = \dot{m}_L u_L + \dot{m}_R u_R \tag{3.96}$$

which is similar to the van Leer FVS. This is more robust against shock anomalies than AUSMD [23].

3.6.1.3 AUSMDV

AUSMD and AUSMV are mixed as follows:

$$(\rho u^2)_{AUSMDV} = \frac{1+s}{2}(\rho u^2)_{AUSMV} + \frac{1-s}{2}(\rho u^2)_{AUSMD} \tag{3.97}$$

with a switching function s of the pressure difference

$$s = \min\left(1,\ K\frac{|p_R - p_L|}{\min\left(p_L, p_R\right)}\right), 0 \le s \le \frac{1}{2} \tag{3.98}$$

with $K = 10$. Moreover, its all-speed extension, “AUSMDV(P),” was proposed in [45].

3.6.1.4 AUSMDV with Shock Fix

AUSMDV is further combined with Hänel, for example, to combat the carbuncle [23]. The shock-normal and shock-parallel directions are solved by different flux functions: (contact-resolving) AUSMDV in the shock-normal direction, and (diffusive) Hänel in the shock-parallel directions to prevent propagation of unphysical information along the numerically captured shock (Fig. 3.11). This strategy is known as “shock fix,” in which the shock and its direction are detected by a sonic-point-based sensor. Thus, for smooth flows or boundary layers, the AUSMDV is recovered. The shock-fixed AUSMDV is one of the robust methods against the shock anomalies (Table 2.2).

3.6.2 AUSM+

As well as Hänel, AUSM+ [46] is designed to preserve the total enthalpy across the shock. This property is regarded as important in hypersonic aeroheating predictions, and is included in our “Hypersonic Heating Computation Tips” [47, 48]. Its formulation is as follows:

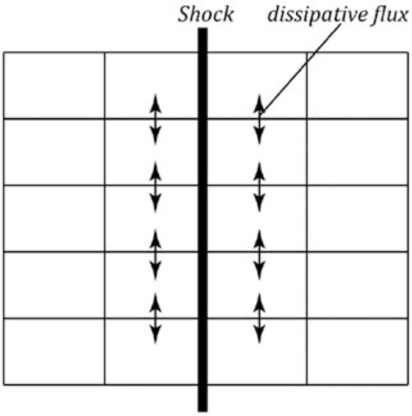

Fig. 3.11 Shock fix

$$\mathbf{F}_{1/2(AUSM+)} = \frac{\dot{m}_{1/2} + \left|\dot{m}_{1/2}\right|}{2}\boldsymbol{\Psi}_L + \frac{\dot{m}_{1/2} - \left|\dot{m}_{1/2}\right|}{2}\boldsymbol{\Psi}_R + \mathbf{P} \tag{3.99}$$

$$\boldsymbol{\Psi} = (1, u, v, H)^T, \mathbf{P} = \left(0, p_{1/2}, 0, 0\right)^T \tag{3.100}$$

$$\dot{m}_{1/2} = \rho_L a_{1/2} \max\left(0, M_{1/2}\right) + \rho_R a_{1/2} \min\left(0, M_{1/2}\right) \tag{3.101}$$

$$M_{1/2} = \mathrm{M}^+ + \mathrm{M}^- \tag{3.102}$$

$$p_{1/2} = \mathrm{P}^+ \cdot p_L + \mathrm{P}^- \cdot p_R \tag{3.103}$$

$$a_{1/2} = \min(\widetilde{a}_L, \widetilde{a}_R), \widetilde{a} = a^{*2} / \max(a^*, |u|) \tag{3.104}$$

$$\mathrm{M}^{\pm} = \begin{cases} \frac{1}{2}(M \pm |M|), & if|M| \geq 1 \\ \pm\frac{1}{4}(M \pm 1)^2 \pm \beta\left(M^2 - 1\right)^2, & otherwise \end{cases} \tag{3.105}$$

$$\mathrm{P}^{\pm} = \begin{cases} \frac{1}{2}(1 \pm sign(M)), & if|M| \geq 1 \\ \frac{1}{4}(M \pm 1)^2(2 \mp M) \pm \alpha M\left(M^2 - 1\right)^2, & otherwise \end{cases} \tag{3.106}$$

where $\alpha = 3/16$ and $\beta = 1/8$ are recommended, and

$$a^{*2} = \frac{2(\gamma - 1)}{(\gamma + 1)}H \tag{3.107}$$

is the critical speed of sound.

Note that the final component of Eq. (3.99) is the total enthalpy H only, as in Hänel. This successfully conserves the total enthalpy due to its direct treatment even across the shock (otherwise, H will be differentiated, and contaminated by a nonzero value of the van Albada limiter, for instance [48]).

This flux is mildly robust against shock anomalies (Table 2.2). However, “expansion shock” is produced unless the numerical speed of sound is modified, or an entropy fix is introduced. Its all-speed extension was formulated as “AUSM+(P)” in [45]. A two-fluid extension for multiphase flows was proposed in [49].

3.6.3 SHUS

Simple High-resolution Upwind Scheme (SHUS) by Shima and Jounouchi [50] has not been published in any journal, but it is popular in Japan. In SHUS, the mass flux of AUSM+ is replaced by Roe’s mass flux (expressed in the Liu–Vinokur form [11]):

$$(\dot{m})_{SHUS} = \frac{1}{2}\left\{(\rho u)^{+} + (\rho u)^{-} - |\overline{u}|\Delta\rho - \frac{|\overline{M}+1| - |\overline{M}-1|}{2}\overline{\rho}\Delta u \right.$$
$$\left. - \frac{|\overline{M}+1| + |\overline{M}-1| - 2|\overline{M}|}{2\overline{c}}\Delta p\right\} \tag{3.108}$$

Liou called this method "AUSM^{+}-R" [51], where "R" stands for Roe (presumably because of this, it can provoke carbuncles). However, it can be used for subsonic flows involving sound waves. Owing to its simplicity and theoretical clarity, SHUS has been used widely, especially in Japan. In addition, its low-speed extended version, LSHUS (Low-dissipative SHUS), was proposed later.

3.6.4 LDFSS

Low-Diffusion Flux Split Scheme (LDFSS) was proposed by Edwards, and later simplified as LDFSS2001 [52]. The key elements of LDFSS2001 scheme are outlined here:

$$\mathbf{F}_{1/2(LDFSS2001)} = \frac{\dot{m}_{1/2} + |\dot{m}_{1/2}|}{2}\boldsymbol{\Psi}_L + \frac{\dot{m}_{1/2} - |\dot{m}_{1/2}|}{2}\boldsymbol{\Psi}_R + \mathbf{P} \tag{3.109}$$

$$\dot{m}^{+} = \rho_L \widetilde{a}_{1/2}\left(\mathrm{M}^{+} - \mathrm{M}^{+}_{1/2}\right), \dot{m}^{-} = \rho_R \widetilde{a}_{1/2}\left(\mathrm{M}^{-} + \mathrm{M}^{-}_{1/2}\right) \tag{3.110}$$

$$\mathrm{M}^{\pm}_{(LDFSS2001)} = \begin{cases} \frac{1}{2}(M \pm |M|), & if |M| \geq 1 \\ \pm\frac{1}{4}(M \pm 1)^2, & otherwise \end{cases} \tag{3.111}$$

$$\begin{aligned} &\mathrm{M}^{+}_{1/2} = f_{1/2}\left(1 - \frac{[\Delta p + \delta|\Delta p|]}{2\rho_L V_{ref}^2}\right), \mathrm{M}^{-}_{1/2} = f_{1/2}\left(1 - \frac{[\Delta p - \delta|\Delta p|]}{2\rho_R V_{ref}^2}\right), \\ &\delta \in [0,4], \Delta p = p_L - p_R \\ &f_{1/2} = \begin{cases} \frac{1}{4}\left[\sqrt{\frac{1}{2}\left(M_L^2 + M_R^2\right)} - 1\right]^2, & if |M_L| < 1, \ |M_R| < 1 \\ 0, & otherwise \end{cases} \end{aligned} \tag{3.112}$$

where the author chose $\delta = 1$ or 4, for instance, and

$$p_{1/2(LDFSS2001)} = \frac{p_L + p_R}{2} + \frac{\mathrm{P}^{+} - \mathrm{P}^{-}}{2}(p_R - p_L) + \overline{\rho} V_{ref}^2(\mathrm{P}^{+} + \mathrm{P}^{-} - 1) \tag{3.113}$$

$$\mathrm{P}^{\pm} = \begin{cases} \frac{1}{2}(1 \pm sign(M)), & if|M| \geq 1 \\ \frac{1}{4}(M \pm 1)^2(2 \mp M), & otherwise \end{cases} \tag{3.114}$$

where the cell-interfacial speed of sound, $\widetilde{a}_{1/2}$, the reference velocity, V_{ref}, and other quantities are as follows:

$$M_{L/R} = u^{\pm}/\widetilde{a}_{1/2}, \widetilde{a}_{1/2} = \sqrt{\widetilde{a}_L \cdot \widetilde{a}_R}, \widetilde{a}_{L/R} = \frac{\sqrt{u^{\pm^2}\left(1 - M_{ref}^2\right)^2 + 4V_{ref}^2}}{1 + M_{ref}^2} \tag{3.115}$$

$$\begin{aligned} M_{ref}^2 &= V_{ref}^2/\tilde{a}_{1/2}{}^2, \\ V_{ref}^2 &= \min\left(a_{1/2}{}^2, \max\left(|\vec{V}|^2, V_\infty^2\right)\right), \\ |\vec{V}|^2 &= u^2 + v^2 \end{aligned} \tag{3.116}$$

$$a_{1/2} = \min\left(a_L, a_R\right), a_{L/R} = a^{*2}/\max\left(a^*, \left|u^{\pm}\right|\right), a^{*2} = \frac{2(\gamma - 1)}{(\gamma + 1)}H \tag{3.117}$$

where the uniform velocity V_∞ should be specified by the user. As can be seen, the numerical speed of sound is scaled to the local velocity order at low-speed flows (Eq. (3.115)). Further, note that in the derivation of Eq. (3.113), the pressure flux (Eq. (3.103)) such as in AUSM+ was first rewritten as

$$\begin{aligned} p_{1/2} &= \mathrm{P}^+ \cdot p_L + \mathrm{P}^- \cdot p_R \\ &= \frac{p_L + p_R}{2} + \frac{\mathrm{P}^+ - \mathrm{P}^-}{2}(p_L - p_R) + \frac{p_L + p_R}{2}(\mathrm{P}^+ + \mathrm{P}^- - 1) \\ &\approx \frac{p_L + p_R}{2} + \frac{\mathrm{P}^+ - \mathrm{P}^-}{2}(p_L - p_R) + \overline{\rho a}^2(\mathrm{P}^+ + \mathrm{P}^- - 1) \end{aligned} \tag{3.118}$$

using the isentropic relation, after which the dissipation term (the last term) was scaled as $\overline{\rho a}^2 \rightarrow \bar{\rho} V_{ref}^2$. This idea has also been employed in SLAU [53].

3.6.5 AUSMPW+

Prof. Chongam Kim's group established AUSMPW (AUSM by Pressure-based Weight-function)+ [54], by blending AUSM+ and AUSMD, and by taking multidimensional effects into account as illustrated in Fig. 3.12.

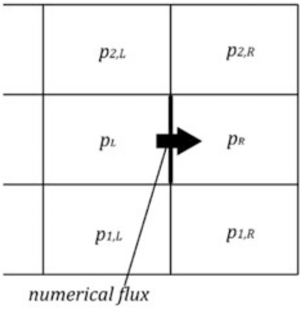

Fig. 3.12 Cell interface and pressure at the surrounding cells (in AUSMPW+ and RoeM)

$$\mathbf{F}_{1/2(AUSMPW+)} = \overline{\mathrm{M}}^{+} a_{1/2}\mathbf{\Phi}_L + \overline{\mathrm{M}}^{-} a_{1/2}\mathbf{\Phi}_R + \mathbf{P} \tag{3.119}$$

$$\mathbf{\Phi} = (\rho, \rho u, \rho v, \rho H)^T, \mathbf{P} = \left(0, p_{1/2}, 0, 0\right)^T \tag{3.120}$$

If $m_{1/2} = \mathrm{M}^+ + \mathrm{M}^- \geq 0$,

$$\begin{aligned} \overline{\mathrm{M}}^{+} &= \mathrm{M}^{+} + \mathrm{M}^{-} \cdot [(1-w)\cdot(1+f_R) - f_L], \\ \overline{\mathrm{M}}^{-} &= \mathrm{M}^{-} \cdot w \cdot (1+f_R) \end{aligned} \tag{3.121}$$

otherwise,

$$\begin{aligned} \overline{\mathrm{M}}^{+} &= \mathrm{M}^{+} \cdot w \cdot (1+f_L), \\ \overline{\mathrm{M}}^{-} &= \mathrm{M}^{-} + \mathrm{M}^{+} \cdot [(1-w)\cdot(1+f_L) - f_R] \end{aligned} \tag{3.122}$$

where

$$w = 1 - \min\left(\frac{p_L}{p_R}, \frac{p_R}{p_L}\right)^3 \tag{3.123}$$

$$f_{L/R} = \begin{cases} \left(\dfrac{p_{L/R}}{p_S} - 1\right) \min\left(1, \frac{\min\left(p_{1,L}, p_{1,R}, p_{2,L}, p_{2,R}\right)}{\min\left(p_L, p_R\right)}\right)^2, & \text{if } p_S \neq 0, \\ 0, & \text{otherwise} \end{cases} \tag{3.124}$$

$$p_S = p_{1/2} = \mathrm{P}^{+} \cdot p_L + \mathrm{P}^{-} \cdot p_R \tag{3.125}$$

and as in AUSM+,

$$\mathrm{M}^{\pm} = \begin{cases} \frac{1}{2}(M \pm |M|), & if |M| \geq 1 \\ \pm\frac{1}{4}(M \pm 1)^2 \pm \beta\left(M^2 - 1\right)^2, & otherwise \end{cases} \tag{3.126}$$

$$\mathrm{P}^{\pm} = \begin{cases} \frac{1}{2}(1 \pm sign(M)), & if |M| \geq 1 \\ \frac{1}{4}(M \pm 1)^2(2 \mp M) \pm \alpha M\left(M^2 - 1\right)^2, & otherwise \end{cases} \tag{3.127}$$

where $\alpha = 0$ or 3/16, $\beta = 0$ are recommended. The interfacial speed of sound is given multidimensionally as

$$a_{1/2} = \begin{cases} \dfrac{a_s^2}{\max\left(|u_L|, a_s\right)} & if \frac{1}{2}(u_L + u_R) > 0 \\ \dfrac{a_s^2}{\max\left(|u_R|, a_s\right)} & if \frac{1}{2}(u_L + u_R) < 0 \end{cases} \tag{3.128}$$

$$a_s^2 = \frac{2(\gamma - 1)}{(\gamma + 1)} H_{normal} \tag{3.129}$$

$$H_{normal} = \frac{1}{2}\left(H_L - \frac{v_L^2}{2} + H_R - \frac{v_R^2}{2}\right) \tag{3.130}$$

where H_{normal} is the total enthalpy H excluding the shock-tangential velocity contribution, v_L and v_R, so that an oblique shock is captured exactly (Fig. 3.13). As a result, the above Mach number M is calculated using this $a_{1/2}$. It is known that a shock-capturing method suffers from wiggles at the shock, especially when the shock passes through the cell interface diagonally. This behavior is partially because most numerical fluxes treat the cell interface in a 1D manner, i.e., without considering directions other than the normal direction to the interface. Therefore, multidimensional considerations such as in AUSMPW+ help to suppress those oscillations at the shock. In addition, this flux also maintains the total enthalpy. It can be seen that multidimensional dissipation is incorporated in Eq. (3.124), which is considered to play a critical role in suppressing carbuncles. In fact, in [55], this effect was intentionally removed by preparing another version (for experimental purposes):

$$f_{L/R} = \begin{cases} \dfrac{p_{L/R}}{p_S} - 1, & if\ p_S \neq 0, \\ 0, & otherwise \end{cases} \tag{3.131}$$

where $p_{\mathrm{L}} = p_{1,\mathrm{L}} = p_{2,\mathrm{L}}$ and $p_{\mathrm{R}} = p_{1,\mathrm{R}} = p_{2,\mathrm{R}}$ were assumed. This version indeed exhibited a higher rate of emergence of shock anomalous solutions. Further improvements have been proposed, such as [56] for "M-AUSMPW+", [57] for multiphase flows, [58, 59] for MHD, and "AUSMPW+_N" in [60].

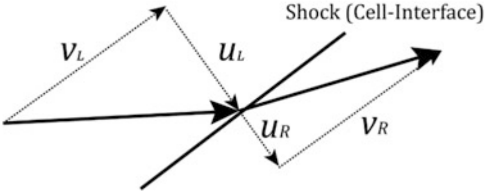

Fig. 3.13 Oblique shock capturing in AUSMPW+

3.6.6 AUSM$^+$-up

AUSM$^+$-up [61], as a sequel to AUSM$^+$ with the additional "*u* (velocity)" and "*p* (pressure)" based dissipation terms, is expressed as follows:

$$\mathbf{F}_{1/2(AUSM+-up)} = \frac{\dot{m}_{1/2} + \left|\dot{m}_{1/2}\right|}{2}\boldsymbol{\Psi}_L + \frac{\dot{m}_{1/2} - \left|\dot{m}_{1/2}\right|}{2}\boldsymbol{\Psi}_R + \mathbf{P} \tag{3.132}$$

$$\boldsymbol{\Psi} = (1, u, v, H)^T, \mathbf{P} = \left(0, p_{1/2}, 0, 0\right)^T \tag{3.133}$$

$$\dot{m}_{1/2} = \rho_L a_{1/2} \max\left(0, M_{1/2}\right) + \rho_R a_{1/2} \min\left(0, M_{1/2}\right) \tag{3.134}$$

$$M_{1/2} = \mathrm{M}^+ + \mathrm{M}^- + M_p \tag{3.135}$$

$$M_p = -\frac{K_p}{f_a} \max\left(1 - \sigma\overline{M}^2, 0\right) \frac{p_R - p_L}{\overline{\rho} a_{1/2}^2}, \overline{\rho} = \frac{\rho_L + \rho_R}{2} \tag{3.136}$$

$$p_{1/2} = \mathrm{P}^+|_\alpha \cdot p_L + \mathrm{P}^-|_\alpha \cdot p_R + p_u \tag{3.137}$$

$$p_u = -K_u \cdot \mathrm{P}^+ \cdot \mathrm{P}^- \cdot (\rho_L + \rho_R) \cdot \left(f_a a_{1/2}\right) \cdot (u^- - u^+) \tag{3.138}$$

$$\left.\begin{aligned} a_{1/2} &= \min(\widetilde{a}_L, \widetilde{a}_R), \\ \widetilde{a}_L &= a^{*2}/\max(a^*, u_L), \widetilde{a}_R = a^{*2}/\max(a^*, -u_R) \end{aligned}\right\} \tag{3.139}$$

$$a^{*2} = \frac{2(\gamma - 1)}{(\gamma + 1)} H \tag{3.140}$$

$$\mathrm{M}^\pm = \begin{cases} \frac{1}{2}(M \pm |M|), & if|M| \geq 1 \\ \pm\frac{1}{4}(M \pm 1)^2 \pm \beta\left(M^2 - 1\right)^2, & otherwise \end{cases} \tag{3.141}$$

$$\mathrm{P}^\pm = \begin{cases} \frac{1}{2}(1 \pm sign(M)), & if|M| \geq 1 \\ \frac{1}{4}(M \pm 1)^2(2 \mp M) \pm \alpha M\left(M^2 - 1\right)^2, & otherwise \end{cases} \tag{3.142}$$

where $K_p = 0.25$, $K_u = 0.75$, $\sigma = 1.0$, and

$$\alpha = \frac{3}{16}\left(-4 + 5f_a^2\right), \beta = \frac{1}{8} \tag{3.143}$$

$$f_a(M_o) = M_o \cdot (2 - M_o) \tag{3.144}$$

$$M_o{}^2 = \min\left(1, \max\left(\overline{M}^2, M_{co}^2\right)\right) \tag{3.145}$$

$$\overline{M}^2 = \frac{u_L^2 + u_R^2}{2a_{1/2}^2} \tag{3.146}$$

The cutoff Mach number, M_{co}, is a user-specified parameter, typically on the order of the free-stream Mach number, M_∞.

Here are the features of AUSM$^+$-up:

- The numerical speed of sound (Eq. (3.139)) is slightly different from that in AUSM$^+$ (Eq. (3.104)). The only difference is the sign, but with this simple modification, AUSM$^+$-up dramatically suppressed the advent of the "expansion shock."
- The other parts are the same as AUSM$^+$ if $M > 1$.
- At $M < 1$, however, α approaches $-3/4$ as $M \rightarrow 0$ and $f_a \rightarrow 2M_{\mathrm{o}}$. As a result, the added dissipation terms in both the mass flux and pressure flux are reduced.

These additional terms improve the solutions at low speeds. f_d has a "cutoff Mach number" inherited from the preconditioning matrix. An analysis of these terms is found in [62].

Let us close with a few more comments on AUSM$^+$-up. A volcano problem (in which temperature rises by colliding flows) [63, 64] was remedied by solving the entropy equation rather than the standard energy equation of AUSM$^+$-up. In addition, Pandare and Luo recently proposed AUSM$^+$-upf [65] for stable multiphase-flow computations.

3.6.7 SLAU

Simple Low-dissipation AUSM (SLAU) by Shima and Kitamura [53] is now presented:

$$\boldsymbol{F}_{SLAU} = \frac{\dot{m} + |\dot{m}|}{2}\boldsymbol{\Psi}^+ + \frac{\dot{m} - |\dot{m}|}{2}\boldsymbol{\Psi}^- + \mathbf{P} \tag{3.147}$$

$$\boldsymbol{\Psi} = (1, \quad u, \quad v, \quad H)^T, \quad \mathbf{P} = \left(0, \quad p_{1/2}, \quad 0, \quad 0\right)^T \tag{3.148}$$

and the mass flux is given by

$$(\dot{m})_{SLAU} = \frac{1}{2}\left\{\rho_L\left(u_L + \left|\overline{V}_n\right|^+\right) + \rho_R\left(u_R - \left|\overline{V}_n\right|^-\right) - \frac{\chi}{a_{1/2}}\Delta p\right\} \tag{3.149}$$

$$\left|\overline{V}_n\right|^+ = (1-g)\left|\overline{V}_n\right| + g|u_L|, \left|\overline{V}_n\right|^- = (1-g)\left|\overline{V}_n\right| + g|u_R| \tag{3.150}$$

$$\left|\overline{V}_n\right| = \frac{\rho_L|u_L| + \rho_R|u_R|}{\rho_L + \rho_R} \tag{3.151}$$

$$g = -\max\left[\min\left(M_L, 0\right), -1\right] \cdot \min\left[\max\left(M_R, 0\right), 1\right] \in [0, 1] \tag{3.152}$$

where

$$\chi = \left(1 - \overset{\frown}{M}\right)^2 \tag{3.153}$$

$$\overset{\frown}{M} = min\left(1.0, \frac{1}{a_{1/2}}\sqrt{\frac{\boldsymbol{u}_L{}^2 + \boldsymbol{u}_R{}^2}{2}}\right) \tag{3.154}$$

$$M = \frac{u}{a_{1/2}} \tag{3.155}$$

$$a_{1/2} = \overline{a} = \frac{a_L + a_R}{2} \tag{3.156}$$

Then, the pressure flux, derived as for LDFSS, is

$$\begin{aligned} p_{1/2(SLAU)} = {} & \frac{p_L + p_R}{2} + \frac{\mathrm{P}^+|_{\alpha=0} - \mathrm{P}^-|_{\alpha=0}}{2}(p_L - p_R) + (1-\chi) \\ & \times \left(\mathrm{P}^+|_{\alpha=0} + \mathrm{P}^-|_{\alpha=0} - 1\right)\frac{p_L + p_R}{2} \end{aligned} \tag{3.157}$$

$$\mathrm{P}^{\pm}\big|_{\alpha} = \begin{cases} \frac{1}{2}(1 \pm sign(M)), & if|M| \geq 1 \\ \frac{1}{4}(M \pm 1)^2(2 \mp M) \pm \alpha M\left(M^2 - 1\right)^2, & otherwise \end{cases} \tag{3.158}$$

The features of SLAU are as follows:

Pros

- The dissipation terms both in the mass flux, Eq. (3.149), and in the pressure flux, Eq. (3.157), are controlled by χ in Eq. (3.153): as the Mach number tends to zero asymptotically, $\chi \to 1 - 2\widehat{M}$, and the last term, $\left(-\frac{\Delta p}{\overline{a}}\right)$, which is small at low Mach flows due to $\frac{1}{\overline{a}}$, is fully activated in the mass flux, while the last term in the pressure flux is scaled by $\left[2\widehat{M}\right]$. On the other hand, $\chi = 0$ if $\widehat{M} \geq 1$, and the original form of the pressure flux is recovered when the last term is used. This is desirable because the pressure difference term in the mass flux is known to provoke the carbuncle phenomenon at supersonic speeds [51].

- Thanks to the multidimensional velocity consideration in Eq. (3.154), this method eliminates the need for the cutoff Mach number. This is a very favorable feature, particularly in flows with no uniform velocity, e.g., internal flows. This parameter-free nature distinguishes SLAU from the other preceding flux functions.
- The g function in Eq. (3.152) successfully suppressed the "expansion shocks."
- SLAU is as robust as AUSM^{+} against the carbuncle, and with a smoother representation of the shock (i.e., with weaker wiggles).

Cons

- SLAU still exhibits shock anomalies under certain conditions.
- Because the last term in the pressure flux is based on the perfect gas assumption, it is not straightforward to extend SLAU to general fluids.

SLAU has been used in many aerodynamic applications, such as the Epsilon Launch Vehicle (Japanese solid-fueled rocket) [66–68].

3.6.8 SD-SLAU

Shock-Detecting SLAU by Shima and Kitamura was designed in [69]. It combines SLAU and SHUS using an original shock detector based on pressure. In SD-SLAU, the shock-normal direction is solved by SLAU, while SHUS is used in the shock-tangential direction to suppress multidimensional wiggles (or sometimes called "noises") that are especially seen in oblique shocks.

The motivation behind the development of SD-SLAU was that while SLAU was more robust against the carbuncle than SHUS, it exhibited wiggles at shocks *not* aligned to the grid lines. As a result, the mass flux in SLAU,

$$(\dot{m})_{SLAU} = \frac{1}{2}\left\{\rho_L\left(u_L + \left|\overline{V}_n\right|^{+}\right) + \rho_R\left(u_R - \left|\overline{V}_n\right|^{-}\right) - \frac{\chi}{\overline{a}}\Delta p\right\} \tag{3.159}$$

has been replaced with the following form in SD-SLAU:

$$(\dot{m})_{SD-SLAU} = \frac{1}{2}\left\{\rho_L\left(u_L + \left|\overline{V}_n\right|^{+}\right) + \rho_R\left(u_R - \left|\overline{V}_n\right|^{-}\right) - \frac{\theta}{\overline{a}}\Delta p\right\} \tag{3.160}$$

where

$$\theta = \min\left(1, \left(\frac{C_{SD2}|\Delta p|/\overline{p} + C_{SD1}}{|\Delta p|_{\max}/\overline{p} + C_{SD1}}\right)^2\right) \cdot \max(0, 1-|M|) \tag{3.161}$$

$$|M| = \left|\overline{V}_n\right|/a_{1/2} \tag{3.162}$$

$$\overline{p} = \frac{1}{2}(p_L + p_R), \Delta p = p_R - p_L \tag{3.163}$$

$$|\Delta p|_{\max} = \max\left[|\Delta p|, \max_j \left|\Delta p_j\right|\right] \tag{3.164}$$

$$\left|\overline{V}_n\right|^+ = (1-g)\left|\overline{V}_n\right| + g|u_L|, \left|\overline{V}_n\right|^- = (1-g)\left|\overline{V}_n\right| + g|u_R| \tag{3.165}$$

$$\left|\overline{V}_n\right| = \frac{\rho_L|u_L| + \rho_R|u_R|}{\rho_L + \rho_R} \tag{3.166}$$

$$g = -\max\left[\min(M_L, 0), -1\right] \cdot \min\left[\max(M_R, 0), 1\right] \in [0, 1] \tag{3.167}$$

because we sought

$$\theta \approx \begin{cases} 0 & \text{near and parallel to the shock (SHUS)} \\ 1 & \text{otherwise (SLAU)} \end{cases} \tag{3.168}$$

where θ is defined at a cell interface, and $C_{SD1} = 0.1$ and $C_{SD2} = 10$ are empirically determined coefficients.

Equation (3.164) finds the maximum pressure difference between the current cell and its surrounding cells. Then, if $|\Delta p|_{\max}$ is much bigger than $|\Delta p|$, it is assumed that there is a shock around the current cell, but not along the interface (i.e., L and R) at which the numerical flux is to be calculated. In this case, θ approaches zero (“near and parallel to the shock”). On the other hand, if both $|\Delta p|_{\max}$ and $|\Delta p|$ are larger than the pressure differences elsewhere, this indicates that the shock exists between L and R, and θ becomes unity. If both $|\Delta p|_{\max}$ and $|\Delta p|$ are very small, C_{SD1} will be dominant, and θ will again become unity. *This shock detector is unique in the sense that it recognizes not only the shock itself, but also its direction.* The pressure flux is common to SLAU.

Consequently, SD-SLAU successfully eliminates these wiggles effectively while maintaining the solution quality of SLAU. This achievement is important because the multidimensional effects have been demonstrated to suppress multidimensional shock-related oscillations, although this method still exhibits shock anomalies in certain cases.

3.6.9 SLAU2, AUSM$^+$-up2, and LDFSS2001-2

SLAU2 was proposed by Kitamura and Shima [70] to enhance the robustness of SLAU against shock anomalies. They first surveyed how the numerical speed of sound, $a_{1/2}$, inside the shock, which is defined only numerically (Fig. 2.2), affected the responses of flux functions to the shock capturing. $a_{1/2}$ was originally defined as the arithmetic mean of the a of both sides,

$$a_{1/2} = \overline{a} = \frac{a_L + a_R}{2}, \tag{3.169}$$

in SLAU, merely because it was not believed to have a significant impact on the solutions in the AUSM family of fluxes [46, 71]. However, after changing the definition to the geometric mean, Roe average, AUSM$^+$ manner, and AUSM$^+$-up manner, the authors discovered that the smaller $a_{1/2}$ is, the better the shock is captured without oscillations/instabilities for SLAU, particularly at high Mach flows, which was contrary to our past expectations. This observation turned out to be very important, because the pressure flux of SLAU, for instance, was

$$\begin{aligned} p_{1/2(SLAU)} = & \frac{p_L + p_R}{2} + \frac{\mathrm{P}^+|_{\alpha=0} - \mathrm{P}^-|_{\alpha=0}}{2}(p_L - p_R) + (1-\chi) \\ & \times \left(\mathrm{P}^+|_{\alpha=0} + \mathrm{P}^-|_{\alpha=0} - 1\right)\frac{p_L + p_R}{2} \end{aligned} \tag{3.157}$$

and $a_{1/2}$ belonged to its dissipation term:

$$\chi = \left(1 - \widehat{M}\right)^2 \tag{3.153}$$

$$\widehat{M} = min\left(1.0, \frac{1}{a_{1/2}}\sqrt{\frac{\boldsymbol{u}_L{}^2 + \boldsymbol{u}_R{}^2}{2}}\right) \tag{3.154}$$

Thus, a small $a_{1/2}$ implies a large $(1-\chi) = 2\widehat{M} - \widehat{M}^2$ and a large dissipation. After reviewing this term, we also realized that this dissipation term cannot grow at high Mach numbers, because $\widehat{M}$ is bounded by unity.

3.6.9.1 SLAU2

Considering those two observations, the dissipation term of the pressure flux was modified from SLAU to

$$p_{1/2(SLAU2)} = \frac{p_L + p_R}{2} + \frac{P^+|_{\alpha=0} - P^-|_{\alpha=0}}{2}(p_L - p_R) + \sqrt{\frac{\boldsymbol{u}_L{}^2 + \boldsymbol{u}_R{}^2}{2}} \cdot \left(P^+|_{\alpha=0} + P^-|_{\alpha=0} - 1\right)\overline{\rho} a_{1/2} \tag{3.170}$$

$$\overline{\rho} = \frac{\rho_L + \rho_R}{2} \tag{3.171}$$

The other formulas are unaltered from SLAU. This single modification greatly improved SLAU2's robustness against shock anomalies (Table 2.2).

After this modification, the numerical dissipation is proportional to the local Mach number at the shock (= *only inside the numerically expressed captured shock*) even at supersonic speeds, whereas it was kept constant in SLAU. *The key idea is that the internal shock structure is only a numerical artifact, and hence, it should be controlled only numerically, not by (invalid) mathematical or physical means* (Fig. 2.2). Furthermore, for the resulting SLAU2, the choice of $a_{1/2}$ has minor effects on the solution (because the dissipation is already large enough to suppress the anomalies), and thus, $a_{1/2} = \overline{a} = \frac{a_L + a_R}{2}$ is still recommended in SLAU2. A detailed explanation is found in the original literature [70].

In addition, this form facilitates extensions of SLAU2 to other fluids such as supercritical fluids (SLAU's dissipation was based on the perfect gas equation of state (EoS), whereas that of SLAU2 is free of such a restriction).

SLAU2 is now widely used all over the world, such as SU2 (Stanford University Unstructured) code [72], FaSTAR [73], LS-FLOW [74], and their users. The author sincerely appreciates all those users/practitioners.

3.6.9.2 AUSM$^+$-up2 and LDFSS2001-2

AUSM$^+$-up2 and LDFSS2001-2 are also realized by simply adopting SLAU2's pressure flux instead of that of AUSM$^+$-up and LDFSS2001, respectively. They are very shock-robust methods too.

$$\begin{aligned} p_{1/2(AUSM+-up2)} &= p_{1/2(LDFSS2001-2)} = p_{1/2(SLAU2)} \\ &= \frac{p_L + p_R}{2} + \frac{P^+|_{\alpha=0} - P^-|_{\alpha=0}}{2}(p_L - p_R) \\ &\quad + \sqrt{\frac{\boldsymbol{u}_L{}^2 + \boldsymbol{u}_R{}^2}{2}} \cdot \left(P^+|_{\alpha=0} + P^-|_{\alpha=0} - 1\right)\overline{\rho} a_{1/2} \end{aligned} \tag{3.172}$$

3.6.10 HR-SLAU2 and HR-AUSM⁺-Up

3.6.10.1 HR-SLAU2

In High-Resolution SLAU2 by Kitamura and Hashimoto [62], the pressure flux of SLAU2 was further modified (i.e., reduced only at subsonic speeds) as follows:

$$p_{1/2(HR-SLAU2)} = \frac{p_L + p_R}{2} + \frac{P^+|_{\alpha=0} - P^-|_{\alpha=0}}{2}(p_L - p_R) + \gamma_{HR} \cdot \sqrt{\frac{\boldsymbol{u}_L{}^2 + \boldsymbol{u}_R{}^2}{2}} \cdot \left(P^+|_{\alpha=0} + P^-|_{\alpha=0} - 1\right)\overline{\rho} a_{1/2} \tag{3.173}$$

where

$$\gamma_{HR} = \max\left(\gamma_{\min}, \gamma_2, \gamma_w\right) \tag{3.174}$$

and $\gamma_{\min}$ is the lower bound, $\gamma_{\min} = 0.2$. Then γ_2 is given by

$$\gamma_2 = \begin{cases} 1 & \phi_{face} \geq 120^\circ \\ 1 - f_d \cdot \left[\frac{2}{3}\cos\left(\phi_{face}\right) + \frac{1}{3}\right] & 0^\circ \leq \phi_{face} < 120^\circ \end{cases} \tag{3.175}$$

where ϕ_{face} is the angle between the $(\boldsymbol{r}_{ij} - \boldsymbol{r}_i)$ and $(\boldsymbol{r}_j - \boldsymbol{r}_{ij})$ vectors ($\boldsymbol{r}_{ij}$, $\boldsymbol{r}_i$, and $\boldsymbol{r}_j$ are the position vectors of the cell-interface center ij, the cell center i, and the cell center j, respectively) (Fig. 3.14). If these three points are located along a single straight line, angle ϕ_{face} is zero (e.g., on 1D or Cartesian grids), and then γ_2 also becomes zero (if $f_d = 1$). When ϕ_{face} is larger than 120°, the original SLAU2 flux is recovered. Note that f_d is the DDES parameter [75], but it is simply set as unity in inviscid or laminar flows. The value γ_w, called the "wiggle detector" [76], is unity when the following relations are satisfied (otherwise, it is zero):

$$\left[(\nabla\phi)_{ij}^{L} \cdot \mathbf{n}_{ij}\right] \cdot \left[(\nabla\phi)_c \cdot \mathbf{n}_{ij}\right] < 0 \tag{3.176}$$

$$\left[(\nabla\phi)_{ij}^{R} \cdot \mathbf{n}_{ij}\right] \cdot \left[(\nabla\phi)_c \cdot \mathbf{n}_{ij}\right] < 0 \tag{3.177}$$

where $\phi = p$ and $(\nabla\phi)_c \cdot \mathbf{n}_{ij} = (\phi_j - \phi_i)/|\mathbf{r}_j - \mathbf{r}_i|$.

On 1D or Cartesian grids, these equations are simplified to

$$\phi_1 \equiv (\phi_i - \phi_{i-1}) \cdot \left(\phi_{i+1} - \phi_i\right) < 0 \tag{3.178}$$

$$\phi_2 \equiv \left(\phi_{i+2} - \phi_{i+1}\right) \cdot \left(\phi_{i+1} - \phi_i\right) < 0 \tag{3.179}$$

In other words, γ_w is given by

Fig. 3.14 Cell geometric properties for HR-SLAU2

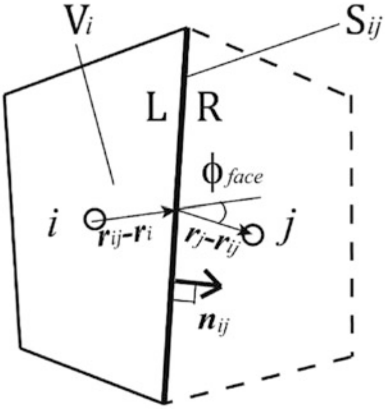

$$\gamma_w = \frac{1 - sign(\min(\phi_1, \phi_2))}{2} \tag{3.180}$$

The above formula is discontinuous at $\phi_1 = 0$ or $\phi_2 = 0$, and thus, smooth functions such as

$$\gamma_w = \frac{1 - \tanh(5\pi \min(\phi_1, \phi_2))}{2} \tag{3.181}$$

would be an alternative option for better convergence, similarly to [77]. This idea was inspired by the work by Winkler et al. [78], in which the dissipation term in the Roe flux was reduced at subsonic flows.

3.6.10.2 HR-AUSM$^+$-up

HR-AUSM$^+$-up is established if the same

$$\gamma_{HR} = \max(\gamma_{\min}, \gamma_2, \gamma_w) \tag{3.174}$$

is multiplied by the dissipation term of the pressure flux of AUSM$^+$-up,

$$p_{1/2(AUSM+-up)} = \mathrm{P}^+|_\alpha \cdot p_L + \mathrm{P}^-|_\alpha \cdot p_R + p_u \tag{3.137$'$}$$

to

$$p_{1/2(HR-AUSM+-up)} = \mathrm{P}^+|_\alpha \cdot p_L + \mathrm{P}^-|_\alpha \cdot p_R + \gamma_{HR} \cdot p_u \tag{3.182}$$

If $M_{co} = M_\infty$ (this is the typical setting), for $M_\infty > 1$, f_a is unity according to Eqs. (3.144)–(3.145), $M_p \approx 0$ from Eq. (3.136), and $p_u = 0$ from Eq. (3.142). Hence, the resulting flux corresponds to the AUSM$^+$ flux [46] at supersonic speeds, apart from the definition of the interfacial sound speed [71] in Eqs. (3.139)–(3.140). At low speeds, on the other hand, Eq. (3.137) can be approximated as

$$p_{1/2(AUSM+-up)} \to \frac{p_L + p_R}{2} + O\left(M_{\mathrm{co}}{}^2\right) \cdot \frac{15}{16} \cdot (M_L p_L - M_R p_R) - O(M_{\mathrm{co}}) \cdot K_u \cdot \frac{1}{4} \cdot 2\overline{\rho} \cdot a_{1/2}^2 \cdot (M_R - M_L) \tag{3.183}$$

where, on the R.H.S., the first term is the central difference, the second term produces the $O(M_{\mathrm{co}}{}^2)$ dissipation, and the third term is the $O(M_{\mathrm{co}})$ dissipation (details are found in [62]). HR-AUSM$^+$-up has γ_{HR} times dissipation according to the last term.

3.7 Others: Rotated Roe-HLL and Genuinely Multidimensional Splitting

Among the many hybridization technologies, we will introduce one of examples, i.e., rotated-hybrid flux functions. The rotated Riemann solver was first proposed by Ren and Sun [79], who decomposed the Roe solver into two directions and used it in different ways. We will also briefly introduce recently published, what is called "genuinely multidimensional" methods, stemming from a staggered-grid approach often adopted in MHD.

3.7.1 Rotated Roe-HLL (RHLL)

Inspired by Ren's work [79], Nishikawa and Kitamura [33] developed a family of rotated-hybrid Riemann solvers: Rotated Roe-HLL (RHLL) and Rotated Roe-Rusanov (RR). It is argued that which class of methods (Roe or HLL) should be chosen in which direction with respect to the shock (normal or parallel). By contrast with the shock fix in AUSMDV [23] or other similar ideas, these methods [33] employ the (contact-resolving) Roe in the shock-*parallel* direction, whereas the (more diffusive) HLL or Rusanov is employed in the shock-*perpendicular* direction to directly suppress the carbuncle from the beginning (Fig. 3.15). A similar idea was later adopted, e.g., in [80].

Let us briefly explain Rotated-RHLL here. Because

$$\mathbf{F}_{1/2(HLL)} = \frac{1}{2}(\mathbf{F}_L + \mathbf{F}_R) - \frac{1}{2}\frac{S_R + S_L}{S_R - S_L}(\mathbf{F}_R - \mathbf{F}_L) + \frac{S_R S_L}{S_R - S_L}(\mathbf{Q}_R - \mathbf{Q}_L) \tag{3.52}$$

and

Fig. 3.15 Schematic of Rotated Roe-HLL (RHLL)

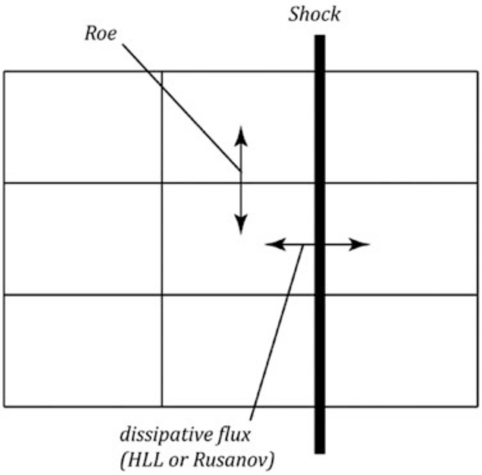

$$\mathbf{F}_{1/2(Roe)} = \frac{1}{2}(\mathbf{F}_L + \mathbf{F}_R) - \frac{1}{2}\widehat{\mathbf{R}}\left|\widehat{\mathbf{\Lambda}}\right|\widehat{\mathbf{L}}\mathbf{\Delta Q} \tag{3.4}$$

the following hybrid flux can be constructed:

$$\begin{aligned}\mathbf{F}_{1/2(Rotated-RHLL)} &= \alpha_1 \mathbf{F}_{1/2(HLL)}(\mathbf{n}_1) + \alpha_2 \mathbf{F}_{1/2(Roe)}(\mathbf{n}_2) \\ &= \frac{1}{2}(\mathbf{F}_L + \mathbf{F}_R) \\ &-\frac{\alpha_1}{2}\frac{S_R + S_L}{S_R - S_L}(\mathbf{F}_R - \mathbf{F}_L) + \frac{\alpha_1 S_R S_L}{S_R - S_L}(\mathbf{Q}_R - \mathbf{Q}_L) \\ &-\frac{\alpha_2}{2}\widehat{\mathbf{R}}\left|\widehat{\mathbf{\Lambda}}\right|\widehat{\mathbf{L}}\mathbf{\Delta Q} \\ &\mathbf{=} \frac{S_R \mathbf{F}_L + S_L \mathbf{F}_R}{S_R - S_L} - \frac{1}{2}\sum_k \left|\widehat{s}^k_{RHLL}\right| \widehat{w}^k_{n2} \widehat{\mathbf{r}}^k_{n2}\end{aligned} \tag{3.184}$$

$$\left|\widehat{s}^k_{RHLL}\right| = \alpha_2 \left|\widehat{\lambda}^k_{n2}\right| - \frac{\alpha_2 (S_R + S_L)\widehat{\lambda}^k_{n2} + 2\alpha_1 S_R S_L}{S_R - S_L} \tag{3.185}$$

where $\widehat{w}^k$ is the wave strength, $\widehat{\mathbf{r}}^k$ is the k-th column of $\widehat{\mathbf{R}}$, $\mathbf{n} = \alpha_1 \mathbf{n}_1 + \alpha_2 \mathbf{n}_2$ (satisfying $\mathbf{n}_1 \cdot \mathbf{n}_2 = 0$, $\|\mathbf{n}_1\| = \|\mathbf{n}_2\| = 1$, $\alpha_1 = \mathbf{n} \cdot \mathbf{n}_1 \geq 0$, $\alpha_2 = \mathbf{n} \cdot \mathbf{n}_2 \geq 0$), and the normal vectors are defined according to the velocity difference

$$\mathbf{n}_1 = \begin{cases} \dfrac{\Delta \mathbf{u}}{\|\Delta \mathbf{u}\|} & if \|\Delta \mathbf{u}\| > \epsilon \\ \mathbf{n} & otherwise \end{cases} \tag{3.186}$$

where $\Delta\mathbf{u} = (\Delta u, \Delta v) = (u_R - u_L, v_R - v_L)$, $\|\Delta\mathbf{u}\| = \sqrt{\Delta u^2 + \Delta v^2}$, and ϵ is a small number.

The flux becomes fully identical to the HLL flux only if $\alpha_1 = 1$, i.e., if the velocity difference vector is perfectly aligned with the cell-face normal. Therefore, the resulting rotated-hybrid flux is generally much less dissipative than the HLL flux. This is different from RoeM [33], in which the Roe flux is switched to the HLLE flux at the shocks detected by pressure, or a similar idea by Quirk [81]. Consequently, the Rotated-RHLL successfully eliminated shock anomalies in Roe (Entropy fix) and even in HLLE (Table 2.2).

3.7.2 Genuinely Multidimensional Splitting

Multidimensional flux functions have been proposed in recent publications, especially in MHD computational papers. This is probably because of the staggered mesh commonly used between the genuinely multidimensional flux and the divergence treatment in MHD. In this genuinely multidimensional splitting, values at both the centers and corners of cell-interfaces are considered. This treatment reportedly helps to stabilize the solutions, as found in [82–86].

References

1. Godunov, S.K.: A finite difference method for the numerical computation of discontinuous solutions of the equations of fluid dynamics. Mat. Sb. **47**, 271 (1959)
2. Hirsch, C.: Numerical Computation of Internal and External Flows, Vol. 2: Computational Methods for Inviscid and Viscous Flows (Wiley Series in Numerical Methods in Engineering). Wiley (1990). ISBN 978-0471924524
3. Toro, E.F.: Riemann Solvers and Numerical Methods for Fluid Dynamics: A Practical Introduction, 3rd edn. Springer-Verlag, Berlin Heidelberg (2009). ISBN 978-3540252023
4. Laney, C.B.: Computational Gas Dynamics. Cambridge University Press, New York, NY (1998. ISBN 9780511605604). https://doi.org/10.1017/CBO9780511605604
5. Masatsuka, K.: I Do Like CFD, Vol. 1: Governing Equations and Exact Solutions (2009) (self-published).
6. Jameson, A.: Origins and further development of the Jameson–Schmidt–Turkel scheme. AIAA J. **55**(5), 1487–1510 (2017). https://doi.org/10.2514/1.J055493
7. Rusanov, V.V.: Calculation of interaction of non-steady shock waves with obstacles. J. Comput. Math. Phys. USSR. **1**, 267–279 (1961)
8. Roe, P.L.: Approximate Riemann solvers, parameter vectors and difference schemes. J. Comput. Phys. **43**, 357–372 (1981)
9. Harten, A.: High resolution schemes for hyperbolic conservation laws. J. Comput. Phys. **49**, 357 (1983)
10. Lin, H.C.: Dissipation additions to flux-difference splitting. J. Comput. Phys. **117**, 20–17 (1995)
11. Liu, Y., Vinokur, M.: Upwind algorithms for general thermo-chemical nonequilibrium flows. In: AIAA Paper 89-0201 (1989)

12. Weiss, J.M., Smith, W.A.: Preconditioning applied to variable and constant density flows. AIAA J. **33**(11), 2050–2057 (1995)
13. Turkel, E.: Preconditioning technique in computational fluid dynamics. Annu. Rev. Fluid Mech. **31**, 385–416 (1999)
14. Kitamura, K., Shima, E., Fujimoto, K., Wang, Z.J.: Performance of low-dissipation Euler fluxes and preconditioned LU-SGS at low speeds. Commun. Comput. Phys. **10**(1), 90–119 (2011). https://doi.org/10.4208/cicp.270910.131110a
15. Li, X.S., Gu, C.W.: An all-speed Roe-type scheme and its asymptotic analysis of low Mach number behavior. J. Comput. Phys. **227**, 5144–5159 (2008)
16. Osher, S., Chakravarthy, S.: Upwind schemes and boundary conditions with applications to Euler equations in general geometries. J. Comput. Phys. **50**, 447–481 (1983)
17. Engquist, B., Osher, S.: One sided difference approximations for nonlinear conservation laws. Math. Comput. **36**(154), 321–351 (1981)
18. Steger, J.L., Warming, R.F.: Flux vector splitting of the inviscid gas-dynamic equations with application to finite-difference methods. J. Comput. Phys. **40**(2), 263–293 (1981)
19. van Leer, B.: Flux-vector splitting for the Euler equations. Lect. Notes Phys. **170**, 507–512 (1982)
20. Hänel, D., Schwane, R., Seider, G.: On the accuracy of upwind schemes for the solution of the Navier–Stokes equations. In: AIAA Paper 1987-1105 (1987)
21. Liou, M.-S.: On a new class of flux splittings. Lect. Notes Phys. **414**, 115–119 (1993)
22. Liou, M., Steffen Jr., C.J.: A new flux splitting scheme. J. Comput. Phys. **107**(1), 23–39 (1993). https://doi.org/10.1006/jcph.1993.1122
23. Wada, Y., Liou, M.S.: An accurate and robust flux splitting scheme for shock and contact discontinuities. SIAM J. Sci. Comput. **18**(3), 633–657 (1997). https://doi.org/10.1137/S1064827595287626
24. Zha, G.C., Bilgen, E.: Numerical solutions of Euler equations by using a new flux vector splitting scheme. Int. J. Numer. Methods Fluids. **17**, 115–144 (1993)
25. Toro, E.F., Vázquez-Cendón, M.E.: Flux splitting schemes for the Euler equations. Comput. Fluids. **70**, 1–12 (2012)
26. Barth, T.J.: Some Notes on Shock-Resolving Flux Functions Part 1: Stationary Characteristics. NASA TM-101087 (1989)
27. Chauvat, Y., Moschetta, J.M., Gressier, J.: Shock wave numerical structure and the carbuncle phenomenon. Int. J. Numer. Methods Fluids. **47**(8–9), 903–909 (2005)
28. Robinet, J., Gressier, J., Casalis, G., Moschetta, J.: Shock wave instability and the carbuncle phenomenon: same intrinsic origin? J. Fluid Mech. **417**(1), 237–263 (2000)
29. Jameson, A.: Analysis and Design of Numerical Schemes for gas dynamics II: artificial diffusion and discrete shock structure. J. Comput. Fluid Dyn. **5**, 1–38 (1995)
30. Harten, A., Lax, P.D., van Leer, B.: On upstream differencing and Godunov-type schemes for hyperbolic conservation Laws. SIAM Rev. **25**(1), 35–61 (1983)
31. Einfeldt, B.: On Godunov-type methods for gas dynamics. SIAM J. Numer. Anal. **25**(2), 294–318 (1988). https://doi.org/10.1137/0725021
32. Obayashi, S., Guruswamy, G.P.: Convergence acceleration of an aeroelastic Navier-Stokes solver. AIAA J. **33**(6), 1134–1141 (1995)
33. Kim, S.S., Kim, C., Rho, O.H., Hong, S.K.: Cures for the shock instability: development of a shock-stable Roe scheme. J. Comput. Phys. **185**(2), 342–374 (2003)
34. Nishikawa, H., Kitamura, K.: Very simple, carbuncle-free, boundary-layer-resolving, rotated-hybrid Riemann solvers. J. Comput. Phys. **227**(4), 2560–2581 (2008). https://doi.org/10.1016/j.jcp.2007.11.003
35. Einfeldt, B., Munz, C.D., Roe, P.L., Sjogreen, B.: On Godunov-type methods near low density. J. Comput. Phys. **92**, 273–295 (1991)
36. Dumbser, M., Balsara, D.S.: A new efficient formulation of the HLLEM Riemann solver for general conservative and non-conservative hyperbolic systems. J. Comput. Phys. **304**, 275–319 (2016)

37. Toro, E.F., Spruce, M., Speares, W.: Restoration of the contact surface in the HLL-Riemann solver. Shock Waves. **4**(1), 25–34 (1994). https://doi.org/10.1007/BF01414629
38. Batten, P., Clarke, N., Lambert, C., Causon, D.M.: On the choice of Wavespeeds for the HLLC Riemann solver. SIAM J. Sci. Comput. **18**, 1553–1570 (1997)
39. Shen, Z., Ren, J., Cui, X.: On the carbuncle instability of the HLLE-type solvers. IOP Conf. Ser. J. Phys. Conf. Ser. **1290**, 012026 (2019). https://doi.org/10.1088/1742-6596/1290/1/012026
40. Park, S.H., Lee, J.E., Kwon, J.H.: Preconditioned HLLE method for flows at all Mach numbers. AIAA J. **44**(11), 2645–2653 (2006). https://doi.org/10.2514/1.12176
41. Luo, H., Baum, J.D., Löhner, R.: Extension of Harten-Lax-van Leer scheme for flows at all speeds. AIAA J. **43**(6), 1160–1166 (2005). https://doi.org/10.2514/1.7567
42. Kitamura, K., Shima, E.: AUSM-like expression of HLLC and its all-speed extension. Int. J. Numer. Methods Fluids. **92**, 246–265 (2020). https://doi.org/10.1002/fld.4782
43. Miyoshi, T., Kusano, K.: A multi-state HLL approximate Riemann solver for ideal magnetohydrodynamics. J. Comput. Phys. **208**, 315–344 (2005)
44. Niu, Y.-Y., Lin, Y.-C., Chang, C.-H.: A further work on multi-phase two-fluid approach for compressible multi-phase flows. Int. J. Numer. Methods Fluids. **58**, 879–896 (2008)
45. Edwards, J.R., Liou, M.-S.: Low-diffusion flux-splitting methods for flows at all speeds. AIAA J. **36**(9), 1610–1617 (1998)
46. Liou, M.S.: A sequel to AUSM: AUSM+. J. Comput. Phys. **129**, 364–382 (1996)
47. Kitamura, K., Shima, E., Nakamura, Y., Roe, P.: Evaluation of Euler fluxes for hypersonic heating computations. AIAA J. **48**(4), 763–776 (2010)
48. Kitamura, K.: Assessment of SLAU2 and other flux functions with slope limiters in hypersonic shock-interaction heating. Comput. Fluids. **129**, 134–145 (2016). https://doi.org/10.1016/j.compfluid.2016.02.006
49. Paillère, H., Corre, C., Cascales, J.R.G.: On the extension of the AUSM+ scheme to compressible two-fluid models. Comput. Fluids. **32**, 891–916 (2003)
50. Shima, E.: Role of CFD in aeronautical engineering (No.14) — AUSM type upwind schemes. NAL-SP30. In: Proceedings of 13th NAL Symposium on Aircraft Computational Aerodynamics, pp. 41–46 (1996)
51. Liou, M.: Mass flux schemes and connection to shock instability. J. Comput. Phys. **160**(2), 623–648 (2000)
52. Edwards, J.R.: Towards unified CFD simulation of real fluid flows. In: AIAA Paper 2001-2524 (2001)
53. Shima, E., Kitamura, K.: Parameter-free simple low-dissipation AUSM-family scheme for all speeds. AIAA J. **49**(8), 1693–1709 (2011). https://doi.org/10.2514/1.55308
54. Kim, K.H., Kim, C., Rho, O.H.: Methods for the accurate computations of hypersonic flows I. AUSMPW+ scheme. J. Comput. Phys. **174**, 38–80 (2001)
55. Kitamura, K., Roe, P., Ismail, F.: Evaluation of Euler fluxes for hypersonic flow computations. AIAA J. **47**, 44–53 (2009). https://doi.org/10.2514/1.33735
56. Kim, K.H., Kim, C.: Accurate, efficient and monotonic numerical methods for multi-dimensional compressible flows, part I: spatial discretization. J. Comput. Phys. **208**, 527–569 (2005)
57. Ihm, S.-W., Kim, C.: Computations of homogeneous-equilibrium two-phase flows with accurate and efficient shock-stable schemes. AIAA J. **46**, 3012–3037 (2008)
58. Han, S.H., Lee, J.I., Kim, K.H.: Accurate and robust pressure weight advection upstream splitting method for magnetohydrodynamics equations. AIAA J. **47**(4), 970–981 (2009)
59. Kitamura, K., Balsara, D.S.: Hybridized SLAU2–HLLI and hybridized AUSMPW+–HLLI Riemann solvers for accurate, robust, and efficient magnetohydrodynamics (MHD) simulations, part I: one-dimensional MHD. Shock Waves. **29**, 611–627 (2019)
60. Kim, H., Choe, Y., Kim, H., Min, D., Kim, C.: Methods for compressible multiphase flows and their applications. Shock Waves. **29**, 235–261 (2019)

61. Liou, M.-S.: A sequel to AUSM, part II: AUSM+-up for all speeds. J. Comput. Phys. **214**, 137–170 (2006)
62. Kitamura, K., Hashimoto, A.: Reduced dissipation AUSM-family fluxes: HR-SLAU2 and HR-AUSM+-up for high resolution unsteady flow simulations. Comput. Fluids. **126**, 41–57 (2016)
63. Liou, M.: Unresolved problems by shock capturing: taming the overheating problem. In: 7th International Conference on Computational Fluid Dynamics, Paper 2012-2203, Big Island, Hawaii (2012)
64. Liou, M.: The root cause of the overheating problem. AIAA 2017-4107, 23rd AIAA Computational Fluid Dynamics Conference, 5–9 June 2017. Denver, CO
65. Pandare, A.K., Luo, H.: A robust and efficient finite volume method for compressible inviscid and viscous two-phase flows. J. Comput. Phys. **371**, 67–91 (2018)
66. Kitamura, K., Nonaka, S., Kuzuu, K., Aono, J., Fujimoto, K., Shima, E.: Numerical and experimental investigations of epsilon launch vehicle aerodynamics at Mach 1.5. J. Spacecr. Rocket. **50**(4), 896–916 (2013). https://doi.org/10.2514/1.A32284
67. Kawauchi, K., Harada, T., Kitamura, K., Nonaka, S.: Experimental and numerical investigations of slender body side force with asymmetric protuberances. J. Spacecr. Rocket. **56**(5), 1346–1357 (2019). https://doi.org/10.2514/1.A34439
68. Aogaki, T., Kitamura, K., Nonaka, S.: High angle-of-attack pitching moment characteristics of slender-bodied reusable rocket. J. Spacecr. Rocket. **55**(6), 1476–1489 (2018). https://doi.org/10.2514/1.A34211
69. Shima, E., Kitamura, K.: Multidimensional numerical noise from captured shockwave and its cure. AIAA J. **51**(4), 992–998 (2013). https://doi.org/10.2514/1.J052046
70. Kitamura, K., Shima, E.: Towards shock-stable and accurate hypersonic heating computations: a new pressure flux for AUSM-family schemes. J. Comput. Phys. **245**, 62–83 (2013)
71. Liou, M.S., Edwards, J.R.: Numerical speed of sound and its application to schemes of all speeds. In: NASA TM-1999-09286, 1999; AIAA Paper 99-3268-CP (1999)
72. Molina, E., Zhou, B.Y., Alonso, J.J., Righi M., Silva, R.G.: Flow and noise predictions around tandem cylinders using DDES approach with SU2. AIAA 2019-0326, AIAA Scitech 2019 Forum, 7–11 January 2019, San Diego, CA
73. Hashimoto, A., Murakami, K., Aoyama, T., Ishiko, K., Hishida, M., Sakashita, M., Lahur, P.: Toward the Fastest Unstructured CFD Code 'FaSTAR'. AIAA-2012-1075 (2012)
74. Kitamura, K., Fujimoto, K., Shima, E., Kuzuu, K., Wang, Z.J.: Validation of an arbitrary unstructured CFD code for aerodynamic analyses. Trans. JSASS. **53**(182), 311–319 (2011)
75. Spalart, P.R., Deck, S., Shur, M.L., Squires, K.D., Strelets, M.K., Travin, A.: A new version of detached-Eddy simulation, resistant to ambiguous grid densities. Theor. Comput. Fluid Dyn. **20**, 181–195 (2006)
76. Mohamed, K., Nadarajah, S., Paraschivoiu, M.: Detached-Eddy simulation of a wing tip vortex at dynamic stall conditions. J. Aircraft. **46**(4), 1302–1313 (2009)
77. Kitamura, K., Shima, E.: Simple and parameter-free second slope limiter for unstructured grid aerodynamic simulations. AIAA J. **50**(6), 1415–1426 (2012)
78. Winkler, C.M., Dorgany, A.J. and Mani, M.: A reduced dissipation approach for unsteady flows on unstructured grids. AIAA 2012-0570 (2012)
79. Ren, Y., Sun, Y.: A multi-dimensional upwind scheme for solving Euler and Navier–Stokes equations. J. Comput. Phys. **219**(1), 391–403 (2006). https://doi.org/10.1016/j.jcp.2006.03.018
80. Kim, S.D., Lee, B.J., Lee, H.J., Jeung, I.-S.: Realization of contact resolving approximate Riemann solvers for strong shock and expansion flows. Int. J. Numer. Methods Fluids. **62**, 1107–1133 (2010)
81. Quirk, J.J.: A contribution to the great Riemann solver debate. Int. J. Numer. Methods Fluids. **18**(6), 555–574 (1994). https://doi.org/10.1002/fld.1650180603
82. Balsara, D.S.: Multidimensional HLLE Riemann solver: application to Euler and magnetohydrodynamic flows. J. Comput. Phys. **229**(6), 1970–1993 (2010). https://doi.org/10.1016/j.jcp.2009.11.018

83. Balsara, D.S.: A two-dimensional HLLC Riemann solver for conservation Laws: application to Euler and magnetohydrodynamic flows. J. Comput. Phys. **231**(22), 7476–7503 (2012). https://doi.org/10.1016/j.jcp.2011.12.025
84. Chen, Z., Huang, X., Ren, Y., Zhou, M.: General procedure for Riemann solver to eliminate carbuncle and shock instability. AIAA J. **55**(6), 2002–2015 (2017)
85. Chen, Z., Huang, X., Ren, Y., Xie, Z., Zhou, M.: Mechanism-derived shock instability elimination for Riemann-solver-based shock-capturing scheme. AIAA J. **56**(9), 3636–3651 (2018)
86. Sanders, R., Morano, E., Druguetz, M.C.: Multidimensional dissipation for upwind schemes: stability and applications to gas dynamics. J. Comput. Phys. **145**(2), 511–537 (1998)

Chapter 4
Numerical Flux Functions Extended to Real Fluids

Abstract This chapter will describe the extensions of the AUSM-family fluxes (specifically, SLAU2) to real fluids of *multiphase flows*, *supercritical fluids*, and *magnetohydrodynamics (MHD)*, where the governing equations and/or their discretizations differ from those for the perfect gas. These fluids are of great importance to physics and industries, but call for special care due to the changes in the equations. Some readers may wonder why the author appears to have a preference for the AUSM family. Here is a list of primary reasons:

1. They are robust and accurate for resolving shock waves at *high speeds*.
2. All-speed variants (e.g., AUSM^{+}-up, SLAU2) are available that are applicable to *low speeds*.
3. No differentiation of a flux function or its Eigenstructure is required, which allows its straightforward application to the complex equation-of-state (EoS) of *multiphase flows*, *supercritical fluids*, or *MHD*.

In this order, the applications will be introduced and numerically demonstrated in this chapter. Let us remark that as the readers will soon realize, it is customary to treat fluids other than the perfect gas by the dimensional form of the governing equations, in contrast with the non-dimensional expression that is common in gas dynamics CFD.

Keywords Multiphase flow · Supercritical fluid · Magnetohydrodynamics (MHD)

4.1 Multiphase Flows

4.1.1 Multiphase Flows: Their Concept and Various Treatments

The AUSM-family fluxes have been extended to multiphase flows as shown in *italic characters* in Fig. 4.1. Here, our primary focus will be on the left half of the figure, i.e., SLAU2, AUSM^{+}-up, and their variants. Before going into their details, let us

K. Kitamura, *Advancement of Shock Capturing Computational Fluid Dynamics Methods*, https://doi.org/10.1007/978-981-15-9011-5_4

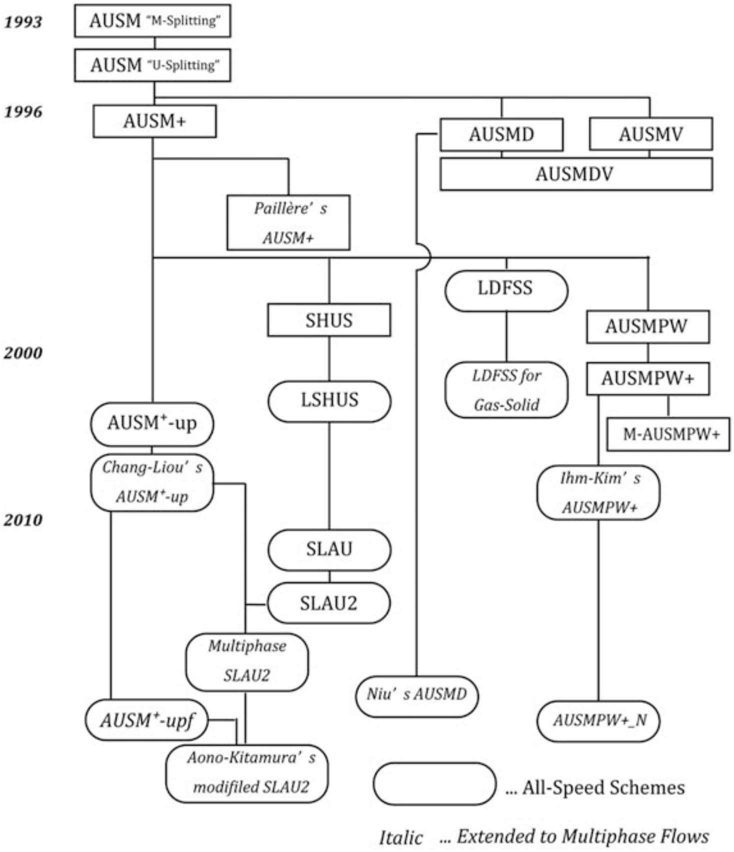

Fig. 4.1 AUSM family tree for multiphase flows

first introduce two confusing terms: "multifluid" flow and "multiphase" flow. Multifluid flow contains fluids of different phases, such as a liquid and gas, and each cell is labeled as either of these only; on the other hand, multiphase flow allows a mixture of liquid and gas, such as liquid-contained gas and gas-contained liquid (Fig. 4.2) [1]. This difference vanishes if infinitesimally small cells are prepared where all the air bubbles, water droplets, and their interfaces are resolved. In practice, however, their sizes can change with time, and/or should be extremely small at their initial phase (i.e., birth stage of a bubble). This situation often arises as a form of cavitation [2], creating many undesirable bubbles around blades operating within the liquid, e.g., the liquid rocket engine [3–5]. Here we will focus on multiphase flows.

Many concepts and methods are used to treat multiphase flows numerically. Let us briefly review some recent representative multiphase-flow computations for a wide range of applications [6–20], such as cavitation over underwater airfoils and propellers, rocket engine turbopumps (aerospace or naval engineering), kidney stone

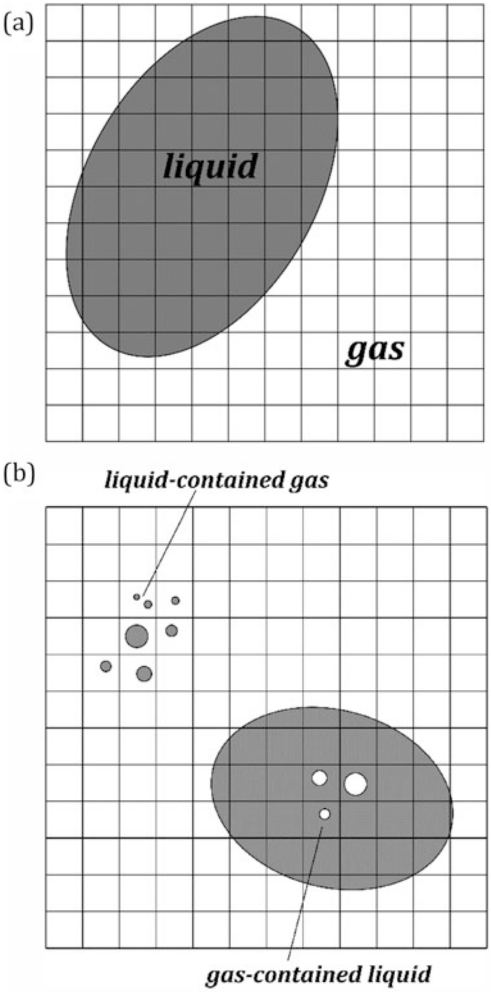

Fig. 4.2 (**a**) Multifluid and (**b**) multiphase flows

removal by a shock (medical), detonation (mechanical), and cooling system in a nuclear reactor at high pressure (nuclear). Two approaches can be delineated in terms of treating phase interfaces: first, the interface-sharpening methods (level set, front tracking, or volume of fluid) and second, the interface-capturing methods (one-fluid or two-fluid modeling) (see Fig. 4.3). The former methods employ an additional step to recognize the location of the interface and impose a numerically smoothed representation of jumps across the interface. Thus, it is accurate in dealing with a single bubble, but will be too expensive when applied to a group of bubbles. What is more, it cannot track the creation or collapse of such phase interfaces. The latter method, on the other hand, captures interface discontinuities as a part of the numerical solution, but the jumps are smeared over a number of mesh points, largely depending on the numerical flux functions and order of accuracy in discretization.

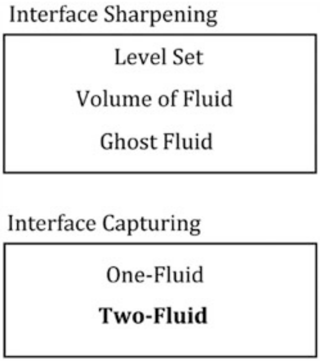

Fig. 4.3 Interface-sharpening and interface-capturing methods for multiphase flows

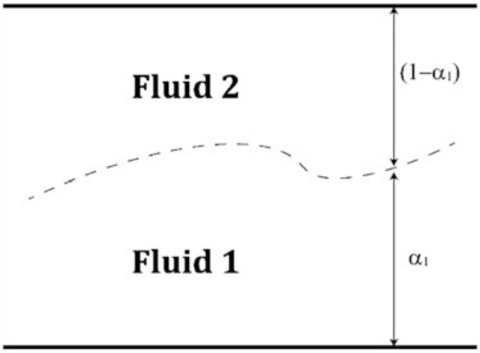

Fig. 4.4 Stratified flow concept

Because "tracking" devices are not used, the interface-capturing approach is "the most practical approach" for dealing with complex geometries like turbopumps, as stated in [21], and it is also able to deal with the dynamic creation of cavitation [1]. As one-fluid modeling is shown to be inadequate for accurate reproduction of cavitation dynamics, we chose two-fluid modeling, which allows each fluid to possess its own physical variables except for pressure. The one-fluid counterpart, on the other hand, deals with the averaged (mixture) density and other common variables such as velocity, but causing difficulties when velocities of gas and liquid phases are different [16]. In other words, the two-fluid modeling (6-equation) approach, in which the governing equations for each phase are solved under the pressure equilibrium assumption between the phases, is employed in the FVM framework of the compressible flow in this section.

Two-fluid modeling is one of the promising approaches for multiphase flows, and is based on the stratified flow concept (Fig. 4.4), in which one fluid and the other fluid coexist in a single cell in a stratified manner. This concept is generalized to the FVM as in Fig. 4.5. One can then realize a gap in the volume fractions between the left and right sides of the cell interface (Fig. 4.5). At this gap, the numerical flux function is used to compute the flux through it.

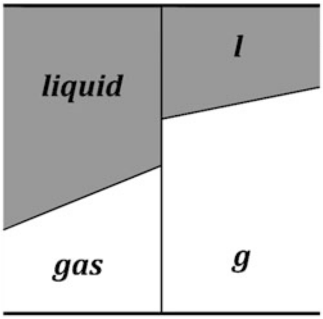

Fig. 4.5 Liquid–gas stratified flow schematic

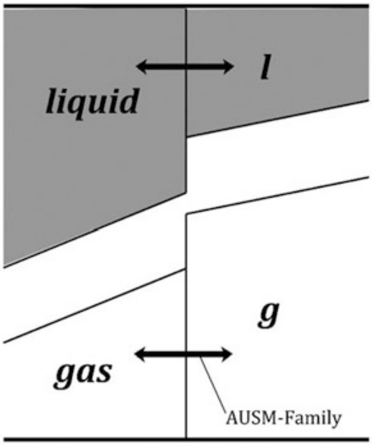

Fig. 4.6 Single AUSM family (SLAU2)

As surveyed thoroughly in [22], as long as the single AUSM-type flux is used (Fig. 4.6), the computations are not robust enough against strong pressure jumps [23]. Chang and Liou [23] proposed a hybridization of Godunov's exact Riemann solver used only for the gas–liquid (or liquid–gas) interface and the AUSM-type flux for the rest (Fig. 4.7). The authors extended this idea to SLAU2 and other AUSM-type fluxes [22]. This section will primarily review the two-fluid-extended SLAU2 and its performance for selected multiphase-flow problems. Note that, of course, this two-fluid solver can treat multifluid and multicomponent flows, where flows of different specific heats, for instance, are solved, such as Helium-bubble/air-shock interaction [24–27].

Fig. 4.7 Godunov/AUSM family (SLAU2)

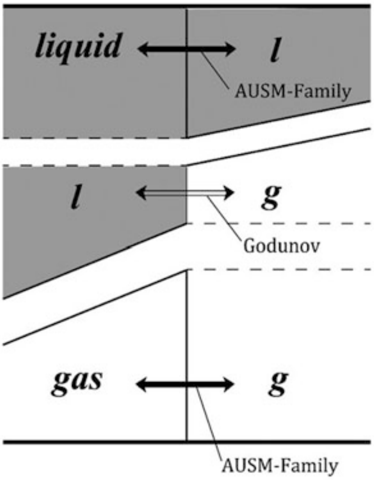

4.1.2 Governing Equations of Two-Fluid Modeling for Multiphase Flows

The 2-D compressible Euler equations are written in two-fluid modeling (also known as effective-fluid modeling, EFM) as

$$\frac{\partial \mathbf{Q}_k}{\partial t} + \frac{\partial \mathbf{E}_k}{\partial x} + \frac{\partial \mathbf{F}_k}{\partial y} = \mathbf{P}_k^{\text{int}} + \mathbf{S}_k, k = 1,2 \tag{4.1}$$

$$\mathbf{Q}_k = \begin{bmatrix} \alpha\rho \\ \alpha\rho u \\ \alpha\rho v \\ \alpha\rho E \end{bmatrix}_k, \mathbf{E}_k = \begin{bmatrix} \alpha\rho u \\ \alpha\rho u^2 + \alpha p \\ \alpha\rho uv \\ \alpha\rho uH \end{bmatrix}_k, \mathbf{F}_k = \begin{bmatrix} \alpha\rho v \\ \alpha\rho vu \\ \alpha\rho v^2 + \alpha p \\ \alpha\rho vH \end{bmatrix}_k,$$

$$\mathbf{P}_k^{\text{int}} = \begin{bmatrix} 0 \\ p^{\text{int}} \dfrac{\partial \alpha}{\partial x} \\ p^{\text{int}} \dfrac{\partial \alpha}{\partial y} \\ -p^{\text{int}} \dfrac{\partial \alpha}{\partial t} \end{bmatrix}_k, \mathbf{S}_k = \begin{bmatrix} 0 \\ \alpha\rho g_x \\ \alpha\rho g_y \\ \alpha\rho g_x u + \alpha\rho g_y v \end{bmatrix}_k \tag{4.2}$$

$$\alpha_g + \alpha_l = 1 \tag{4.3}$$

$$p_g = p_l \equiv p \tag{4.4}$$

$$p_g^{\text{int}} = p_l^{\text{int}} \equiv p^{\text{int}} \tag{4.5}$$

$$p^{\text{int}} = p - \delta p^* \tag{4.6}$$

where α is the volume fraction of a fluid, ρ is the density, u and v are the velocity components in Cartesian coordinates, E is the total energy per unit mass [$E = e + (p/\rho)$, e being the internal energy], H is the total enthalpy [$H = E + (p/\rho)$], p is the pressure, and g_x and g_y are the x- and y-components of the gravity vector (of magnitude 9.8 m/s^2: *Note that all the values are expressed dimensionally in this section* as is typically done in the relevant papers, but in contrast with single-phase papers). Because we treat only gas–liquid systems in this study, $k = 1, 2$ stands for $k = g, l$, where g represents gas and l represents liquid. As in single-fluid equations, $\mathbf{Q}$ is the conservative-variable vector; $\mathbf{E}$ and $\mathbf{F}$ are the inviscid flux vectors in the x- and y-directions, respectively, apart from the fact that α included; p_k^{int} is the so-called (phase-) interface pressure, and $\mathbf{S}_k$ is the source term containing the gravity force considered, for instance, in the "Faucet" problem [28]. Equation (4.3) expresses the compatibility relation for volume fractions, Eqs. (4.4) and (4.5) assume a pressure equilibrium, and Eq. (4.6) gives the interface pressure, p^{int}, expressed as a departure from p by δp^* (described in Sect. 4.1.4). Now we have 14 unknowns [α, ρ, u, v, e, p, p^{int}]$_k$, that are closed by 12 equations [Eqs. (4.1)–(4.6)] and two EoSs (equations of state) explained later in Sect. 4.1.5.

4.1.3 Stratified Flow Model and Discretization

We follow the concept of a stratified flow model, first proposed by Stewart and Wendroff [29] (Fig. 4.4) and refined later by Chang and Liou [23] and Liou et al. [30], for constructing a discrete model. Hence, it is clear that the interfacial pressure p^{int} must work only within each computation cell. In addition, the volume fractions are assumed to be continuous within the cell but are allowed to jump at the cell boundaries (Figs. 4.5 and 4.8). The discretized form of Eq. (4.1), in the 1D form for illustrative purposes, is expressed as

$$\begin{aligned} &\frac{V_j}{\Delta t}\Delta\mathbf{Q}_j + \mathbf{E}_{j+1/2}S_{j+1/2} - \mathbf{E}_{j-1/2}S_{j-1/2} \\ &= p_j^{\text{int}}\begin{bmatrix} 0 \\ \alpha_{j+1/2,L} - \alpha_{j-1/2,R} \\ \dfrac{V_j\left(\alpha_j^{n+1} - \alpha_j^n\right)}{\Delta t} \end{bmatrix} + \mathbf{S}_j \end{aligned} \tag{4.7}$$

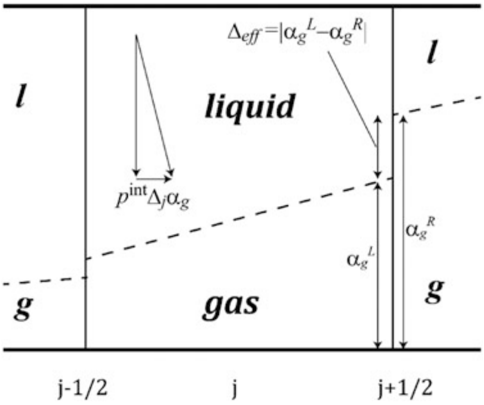

Fig. 4.8 Discretized, stratified flow concept

where the phase-subscript k is omitted. V_j is the volume of cell j (which is the cell index), and $S_{j+1/2}$ is the area of the interface between cells j and $j+1$. All cell-interface variables (such as $\alpha_{j+1/2,\ L}$) are calculated by the spatially second-order accurate MUSCL interpolation [31] with van Albada's limiter [32].

4.1.4 Interface Pressure

The interface pressure, p^{int}, introduced by Stuhmiller [33], working at a phase interface *within* a cell is expressed, according to Liou et al. (Fig. 4.8) [30], as

$$p^{\mathrm{int}} = p - \delta p^* \tag{4.6}$$

and for a gas–liquid system,

$$\delta p^* = \sigma \frac{\alpha_g \alpha_l \rho_g \rho_l}{\alpha_g \rho_l + \alpha_l \rho_g} \left| \mathbf{u}_l - \mathbf{u}_g \right|^2 \tag{4.8}$$

which is simplified, after assuming $\rho_l >> \rho_g$ and (α_l, α_g) are finite, as

$$\delta p^* = C_p^* \alpha_l \rho_g \left| \mathbf{u}_l - \mathbf{u}_g \right|^2 \tag{4.9}$$

We will make use of the simplified form of Eq. (4.9) with $C_p^* = 2.0$. Furthermore, to prevent p^{int} from deviating too much from the static pressure p, a limit is imposed so that δp^* does not exceed a fraction of p:

$$\delta p^* = \min\left(\delta p^*, \varepsilon_p p\right) \tag{4.10}$$

where the value of $\varepsilon_p = 0.01$ was suggested in [23].

4.1.5 Equation of State (EoS)

We adopted the stiffened-gas model proposed by Harlow and Amsden [34] as the EoS:

$$p_k = \rho_k \frac{\gamma_k - 1}{\gamma_k} C_{pk} T_k - p_{k\infty} \tag{4.11}$$

$$e_k = \frac{C_{pk}}{\gamma_k} T_k + \frac{p_{k\infty}}{\rho_k} \tag{4.12}$$

$$a_k = \left(\frac{\gamma_k (p_k + p_{k\infty})}{\rho_k} \right)^{1/2} \tag{4.13}$$

where e_k is the internal energy per unit mass of fluid k, and a_k is the speed of sound. The standard ideal gas becomes a subset of the stiffened gas, and hence it is used to describe both gas and liquid states, but with different parameter values (Note: these values vary in the literature) [30]:

$$\gamma_g = 1.4, C_{pg} = 1004.5[\mathrm{J/(kg\ K)}], p_{g\infty} = 0[\mathrm{Pa}](\mathrm{air})$$

$$\gamma_l = 2.8, C_{pl} = 4186[\mathrm{J/(kg\ K)}], p_{l\infty} = 8.5 \times 10^8[\mathrm{Pa}](\mathrm{water})$$

It is reported by Jolgam et al. [35] that although the stiffened-gas EoS is relatively simple, it has almost the same accuracy as the more sophisticated Tait's EoS or van der Waals's EoS.

4.1.6 Numerical Fluxes

SLAU2 is used to calculate numerical fluxes for each phase, denoted as $\mathbf{F}_{k,1/2,L/R}$, where L and R indicate the left and right cells, respectively. The numerical flux is expressed as

$$\begin{aligned} \mathbf{F}_{k,1/2,L/R} = & \frac{\dot{m}_{k,1/2} + \left|\dot{m}_{k,1/2}\right|}{2} \mathbf{\Psi}_{k,L} + \frac{\dot{m}_{k,1/2} - \left|\dot{m}_{k,1/2}\right|}{2} \mathbf{\Psi}_{k,R} \\ & + \alpha_{k,1/2,L/R} p_{k,1/2} \mathbf{N} \end{aligned} \tag{4.14}$$

$$\mathbf{\Psi}_k = (\alpha, \alpha u, \alpha v, \alpha H,)_k^T, \mathbf{N} = (0, 1, 0, 0)^T \tag{4.15}$$

Only SLAU2 can be used, whereas the exact Riemann (Godunov) solver can be combined with it [23]. In the latter case, the Godunov solver is used only when the difference between the volume fractions at a cell interface (i.e., “the effective length,” $\Delta_{eff} = |\alpha_{g,1/2,L} - \alpha_{g,1/2,R}|$) is above a threshold, say, ε:

- *if* $\Delta_{eff} = |\alpha_{g,1/2,L} - \alpha_{g,1/2,R}| < \varepsilon$: SLAU2 is used everywhere;
- *otherwise*: SLAU2 flux is used for gas–gas and liquid–liquid interfaces, with Godunov elsewhere

These two approaches are illustrated in Figs. 4.6 and 4.7: In either case, at least one AUSM-family flux (SLAU2 in this book) is used. The AUSM schemes [36–41] have showed satisfactory performance in single-phase gas flows from low speed to hypersonic as stated in the previous chapters. Here, we include in the following the multiphase-flow version of SLAU2.

4.1.6.1 SLAU and SLAU2

SLAU by Shima and Kitamura [37] is extended for multiphase flows as follows. The mass flux for each fluid is given as

$$\left(\dot{m}_{k,1/2}\right)_{SLAU} = \frac{1}{2} \times \left\{\rho_{k,L}\left(u_{k,L} + \left|\overline{V}_{k,n}\right|^{+}\right) + \rho_{k,R}\left(u_{k,R} - \left|\overline{V}_{k,n}\right|^{-}\right) - \frac{\chi_k}{a_{1/2}}(p_R - p_L)\right\} \tag{4.16}$$

$$\left|\overline{V}_{k,n}\right|^{+} = (1-g_k)\left|\overline{V}_{k,n}\right| + g_k|u_{k,L}|, \left|\overline{V}_{k,n}\right|^{-} = (1-g_k)\left|\overline{V}_{k,n}\right| + g_k|u_{k,R}| \tag{4.17}$$

$$\left|\overline{V}_{k,n}\right| = \frac{\rho_{k,L}|u_{k,L}| + \rho_{k,R}|u_{k,R}|}{\rho_{k,L} + \rho_{k,R}} \tag{4.18}$$

$$g_k = -\max\left[\min\left(M_{k,L}, 0\right), -1\right] \cdot \min\left[\max\left(M_{k,R}, 0\right), 1\right] \in [0,1] \tag{4.19}$$

$$\chi_k = \left(1 - \widehat{M}_k\right)^2 \tag{4.20}$$

$$\widehat{M}_k = \min\left(1.0, \frac{1}{a_{1/2}}\sqrt{\frac{\boldsymbol{u}_{k,L}{}^2 + \boldsymbol{u}_{k,R}{}^2}{2}}\right) \tag{4.21}$$

$$M_k = \frac{u_k}{a_{1/2}} \tag{4.22}$$

where the common speed of sound for gas and liquid $a_{1/2}$ is given again by

$$a_{1/2} = \frac{1}{2}\left(a_{l,1/2} + a_{g,1/2}\right) \tag{4.23}$$

$$a_{k,1/2} = \overline{a}_k = \frac{a_{k,L} + a_{k,R}}{2} \tag{4.24}$$

We recognize that other forms for providing the interface speed of sound $a_{k,1/2}$ (e.g., the geometric mean of left and right states) are possible, but we confirmed that the present choice (arithmetic mean) gives robust performance. The pressure flux is then

$$\begin{aligned}\left(p_{k,1/2}\right)_{SLAU} &= \frac{p_L + p_R}{2} + \frac{\left.\mathrm{P}^{+}_{(5)k}(M_{k,L})\right|_{\alpha=0} - \left.\mathrm{P}^{-}_{(5)k}(M_{k,R})\right|_{\alpha=0}}{2}(p_L - p_R) \\ &+ (1-\chi_k)\left(\left.\mathrm{P}^{+}_{(5)k}(M_{k,L})\right|_{\alpha=0} + \left.\mathrm{P}^{-}_{(5)k}(M_{k,R})\right|_{\alpha=0} - 1\right)\frac{p_L + p_R}{2}\end{aligned} \tag{4.25}$$

$$\left.\mathrm{P}^{\pm}\right|_{\alpha} = \begin{cases} \frac{1}{2}(1 \pm sign(M)), & if|M| \geq 1 \\ \frac{1}{4}(M \pm 1)^2(2 \mp M) \pm \alpha M\left(M^2 - 1\right)^2, & otherwise \end{cases} \tag{4.26}$$

where $\alpha = 0$.

The dissipation term (last term) in the pressure flux was originally designed only for the ideal gas, according to the relation $\overline{p} \propto \overline{\rho a}^2$. In SLAU2, this term was modified so that real fluids can be treated.

In SLAU2 [40], the dissipation term in the pressure flux of SLAU [Eq. (4.25)] is

$$\begin{aligned}\left(p_{k,1/2}\right)_{SLAU2} &= \frac{p_L + p_R}{2} + \frac{\left.\mathrm{P}^{+}_{(5)k}(M_{k,L})\right|_{\alpha=0} - \left.\mathrm{P}^{-}_{(5)k}(M_{k,R})\right|_{\alpha=0}}{2}(p_L - p_R) \\ &+ \sqrt{\frac{\mathbf{u}_{k,L}{}^2 + \mathbf{u}_{k,R}{}^2}{2}}\left(\left.\mathrm{P}^{+}_{(5)k}(M_{k,L})\right|_{\alpha=0} + \left.\mathrm{P}^{-}_{(5)k}(M_{k,R})\right|_{\alpha=0} - 1\right)\overline{\rho}_k a_{1/2}\end{aligned} \tag{4.27}$$

for (1) ready extension to real fluids and (2) γ times the dissipation.

4.1.6.2 G-SLAU2: Combination with Godunov Solver

As stated above, utilizing the exact Riemann (Godunov) solver is another approach. The Godunov solver is used only when the void fraction jump is large (Fig. 4.7); otherwise, only SLAU2 is used (Fig. 4.6). In other words, the former method includes the latter when the effective length is small.

The exact Riemann (Godunov) solver [42] for a stiffened-gas EoS is written in a very similar manner as in the ideal gas [23, 43]. Solving this tells us whether the right phase flows into the left, or vice versa (Fig. 4.9). This combination of Godunov and SLAU2 is denoted as "G-SLAU2." In a similar manner, "H-SLAU2" can be established, where "H" stands for "HLLC" [44].

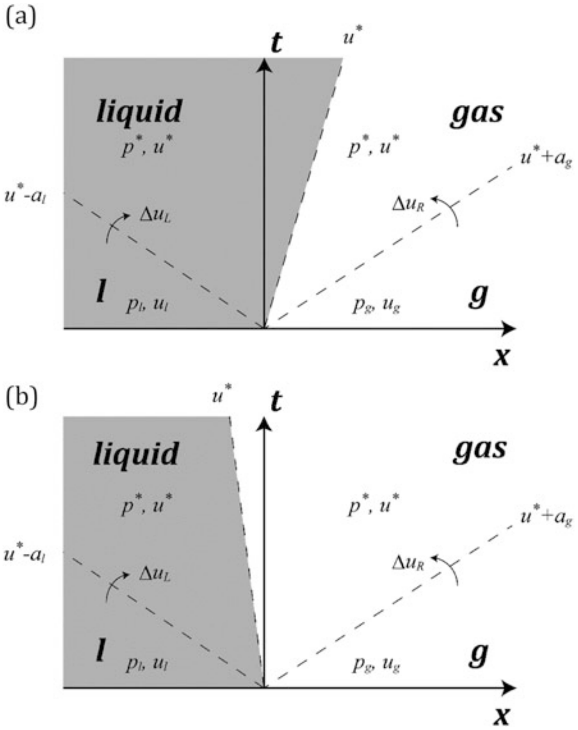

Fig. 4.9 Riemann problem in liquid–gas two-phase flow

4.1.7 Time Integration, Decoding, and Update of Variables

Equation (4.7) is rewritten in the three-stage TVD Runge-Kutta [45] form as

$$\widehat{\mathbf{Q}}_j^{(1)} = \widehat{\mathbf{Q}}_j^n + \frac{\Delta t}{V_j}\mathbf{R}_j^n \tag{4.28}$$

$$\widehat{\mathbf{Q}}_j^{(2)} = \frac{3}{4}\widehat{\mathbf{Q}}_j^n + \frac{1}{4}\widehat{\mathbf{Q}}_j^{(1)} + \frac{1}{4}\frac{\Delta t}{V_j}\mathbf{R}_j^{(1)} \tag{4.29}$$

$$\widehat{\mathbf{Q}}_j^{n+1} = \frac{1}{3}\widehat{\mathbf{Q}}_j^n + \frac{2}{3}\widehat{\mathbf{Q}}_j^{(2)} + \frac{2}{3}\frac{\Delta t}{V_j}\mathbf{R}_j^{(2)} \tag{4.30}$$

$$\widehat{\mathbf{Q}}_j \equiv \mathbf{Q}_j + \begin{bmatrix} 0 \\ 0 \\ p_j^{\mathrm{int}}\alpha_j \end{bmatrix} = \begin{bmatrix} \widehat{Q}_1 \\ \widehat{Q}_2 \\ \widehat{Q}_3 \end{bmatrix} \tag{4.31}$$

$$\mathbf{R}_j \equiv -\left[\mathbf{E}_{j+1/2}S_{j+1/2} - \mathbf{E}_{j-1/2}S_{j-1/2}\right] + \begin{bmatrix} 0 \\ p_j^{\mathrm{int}}\left(\alpha_{j+1/2,L} - \alpha_{j-1/2,R}\right) \\ 0 \end{bmatrix} + \mathbf{S}_j \tag{4.32}$$

where k is omitted for brevity, but the term $(p^{\mathrm{int}}\alpha)$ is included in $\widehat{\mathbf{Q}}$ as in Eq. (4.31) [30, 46]. p^{int} is frozen throughout the Runge-Kutta stages at the value of nth time step [46].

After obtaining $\widehat{\mathbf{Q}}^{n+1}$, we conduct the following decoding process to update $p^{\mathrm{n+1}}$ and $\alpha_k^{\mathrm{n+1}}$

$$F(p) = p^2 - Bp - C = 0 \tag{4.33}$$

Because p is positive, a unique root is determined:

$$p = \frac{1}{2}\left(B + \sqrt{B^2 + 4C}\right) \tag{4.34}$$

with the volume fraction

$$\alpha_k = \frac{\widehat{A}_k}{p + \widehat{a}_k} \tag{4.35}$$

where

$$\widehat{A}_k = (\gamma_k - 1)\left(\widehat{Q}_{3,k} - \frac{\widehat{Q}_{2,k}^2}{2\widehat{Q}_{1,k}}\right) \tag{4.36}$$

$$B = \sum_{k=1}^{2}\left(\widehat{A}_k - \widehat{a}_k\right) \tag{4.37}$$

$$C = \widehat{a}_1\widehat{A}_2 + \widehat{a}_2\widehat{A}_1 - \widehat{a}_1\widehat{a}_2 \tag{4.38}$$

$$\widehat{a}_k = \gamma_k p_{k,\infty} + (\gamma_k - 1)p^{\mathrm{int}} \tag{4.39}$$

Because a large value of $p_{l\infty}$ is involved in these equations, the resulting numerical errors can be large. Thus, to improve the accuracy, Eq. (4.35) is solved simultaneously by a Newton iteration method for both the air and water phases [23]:

$$\begin{cases} F_g = (p + \widehat{a}_g)\alpha_g - \widehat{A}_g = 0 \\ F_l = (p + \widehat{a}_l)\alpha_l - \widehat{A}_l = 0 \end{cases} \tag{4.40}$$

Usually, a few iterations are enough to reduce the pressure error to below 10^{-5}.

Next, to enhance stability, variables of the "vanishing" phase (i.e., $\varepsilon_{\min} \leq \alpha_1 \leq \varepsilon_{\max}$) are blended with those of the remaining phase (i.e., $\alpha_2 \approx 1$) [23, 47]:

$$(q_1)_{adjust} = G(\xi_1)q_1 + (1 - G(\xi_1))q_2, q = \mathbf{u}, T \tag{4.41}$$

$$G(\xi_1) = -\xi_1^2(2\xi_1 - 3) \tag{4.42}$$

$$\xi_1 = \frac{\alpha_1 - \varepsilon_{\min}}{\varepsilon_{\max} - \varepsilon_{\min}} \tag{4.43}$$

where G is a smooth function satisfying $G(0) = 0$, $G(1) = 1$, and $G'(0) = G'(1) = 0$. The small values of $\varepsilon_{\min}$ and $\varepsilon_{\max}$ are chosen as 0.1ε and $10^3\varepsilon$ in this book, unless otherwise stated. If α_1 is below $\varepsilon_{\min}$, $\alpha_1 = \varepsilon_{\min}$ is enforced. Note that we must update ($\mathbf{u}$, T), not ($\mathbf{u}$, ρ). If the density is replaced by that of the other phase, which differs by a factor of $O(10^3)$, a large error will possibly emerge in the water temperature, say, $O(10^5)$ [K] at the standard sea-level conditions.

4.1.8 Boundary Conditions

Because a cell-centered, 2-D structured grid solver is used here, the following typical boundary conditions using the typical "ghost cell" approach are applied as follows [47]:

- Inlet: All the variables are imposed except for pressure.
- Outlet: Only pressure is specified, and all the other variables are extrapolated.
- Slip: The opposite sign is assigned to the velocity component normal to the boundary.

4.1.9 Numerical Examples

The SLAU2 extended to multiphase flows or G-SLAU2 will be used. The following "CFL-like number" is adopted to determine the time step:

$$CFL = \Delta t / \min_j \left(\frac{\Delta x}{\max(a_g, a_l) + \max(|\mathbf{u}_g|, |\mathbf{u}_l|)} \right)_j \tag{4.44}$$

4.1.9.1 Moving Phase Contact Discontinuity

A moving contact discontinuity between air and water is solved [23] as the first problem. It is desired to accurately capture this phase discontinuity at $x = 5$ m, across which a constant pressure should be maintained. 200 uniform cells is used for the domain of [0 m, 10 m]. The initial conditions are given as follows:

$$x \le 5\ \mathrm{m} : \left(p, u_k, T_k, \alpha_g\right)_L = \left(10^5\mathrm{Pa}, 100\ \mathrm{m/s}, 300\ \mathrm{K}, 1 - \varepsilon\right)$$

$$x > 5\ \mathrm{m} : \left(p, u_k, T_k, \alpha_g\right)_R = \left(10^5\mathrm{Pa}, 100\ \mathrm{m/s}, 300\ \mathrm{K}, \varepsilon\right)$$

where $k = g, l$. Note that this setup leads to $\rho_l = 1053\ \mathrm{kg/m^3}$ and $\rho_g = 1.16\ \mathrm{kg/m^3}$; that is, a large density ratio of $O(10^3)$ across the interface, which is known as a difficult condition for preserving a constant pressure [48]. The computations are conducted with $\Delta t = 6.0 \times 10^{-6}$ s (CFL ≈ 0.2) until 0.03 s (5000 steps).

The solutions are displayed in Fig. 4.10. SLAU2 showed excellent performance in both smooth transition of the two phases and preserving a uniform pressure across the contact discontinuity. Note that these solutions are almost identical to those obtained by using other AUSM-family fluxes such as AUSM$^+$-up or G-SLAU2.

4.1.9.2 Air-to-Water Shock Tube

$$x \le 5\ \mathrm{m} : \left(p, u_k, T_k, \alpha_g\right)_L = \left(10^9\mathrm{Pa}, 0\ \mathrm{m/s}, 308.15\ \mathrm{K}, 1 - \varepsilon\right)$$

$$x > 5\ \mathrm{m} : \left(p, u_k, T_k, \alpha_g\right)_R = \left(10^5\mathrm{Pa}, 0\ \mathrm{m/s}, 308.15\ \mathrm{K}, \varepsilon\right)$$

where $k = g, l$, with the uniform cells ($\Delta x = 0.02$ m).

The simulation is conducted with $\Delta t = 2.0 \times 10^{-6}$ s (CFL ≈ 0.2) until 2.0×10^{-3} s (1000 steps).

The result of SLAU2 is shown in Fig. 4.11. It displayed a smooth rarefaction wave, a phase interface, and a shock.

4.1.9.3 Water-to-Air Shock Tube

$$x \le 5\ \mathrm{m} : \left(p, u_k, T_k, \alpha_g\right)_L = \left(1 \times 10^7\mathrm{Pa}, 0\ \mathrm{m/s}, 308.15\ \mathrm{K}, \varepsilon\right)$$

$$x > 5\ \mathrm{m} : \left(p, u_k, T_k, \alpha_g\right)_R = \left(5 \times 10^6\mathrm{Pa}, 0\ \mathrm{m/s}, 308.15\ \mathrm{K}, 1 - \varepsilon\right)$$

with $\Delta x = 0.02$ m and $\Delta t = 2.0 \times 10^{-6}$ s (CFL ≈ 0.2), until 2.0×10^{-3} s (1000 steps).

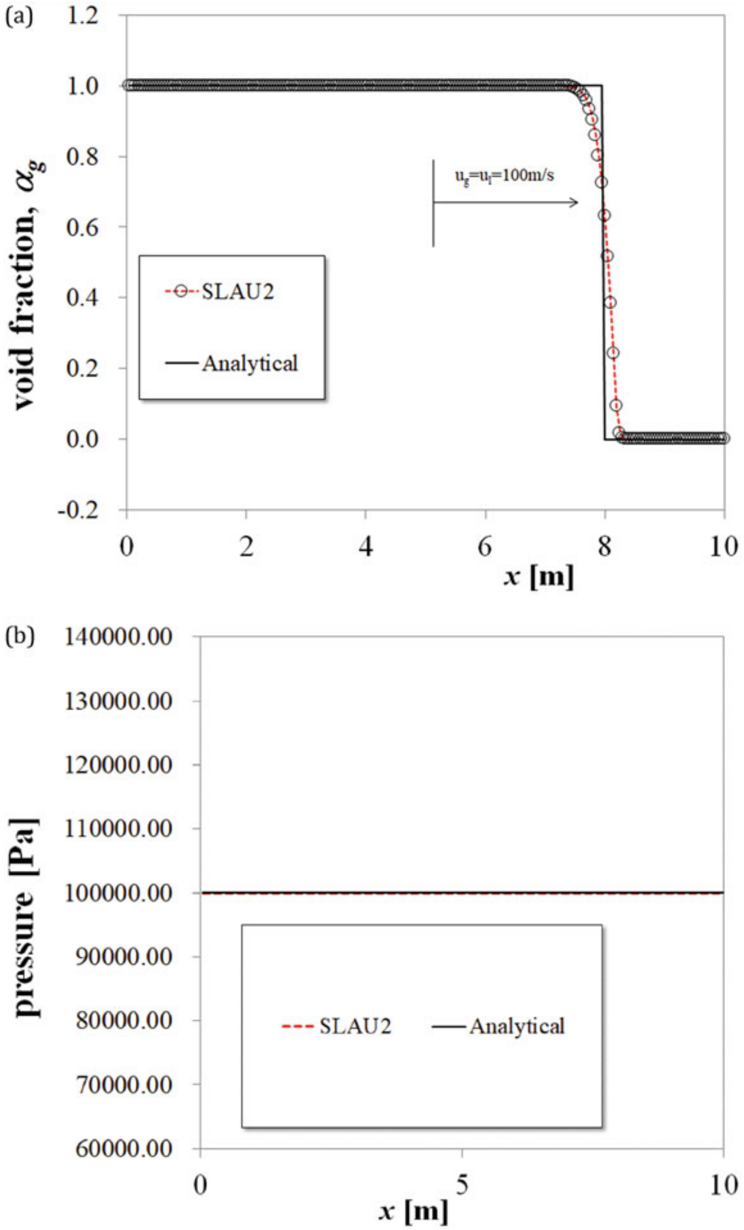

Fig. 4.10 Moving phase contact discontinuity solutions (SLAU2) at $t = 0.03$ s: (**a**) void fraction, α_g; (**b**) pressure

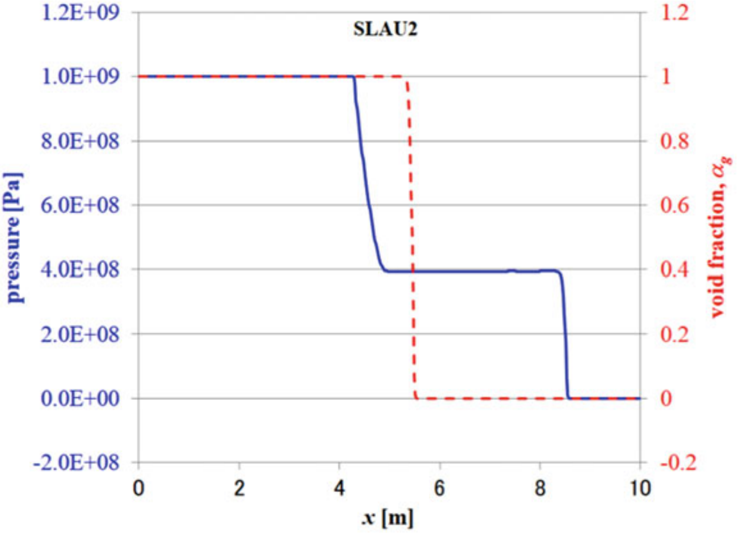

Fig. 4.11 Air-to-water shock tube problem solutions at $t = 2$ ms, SLAU2

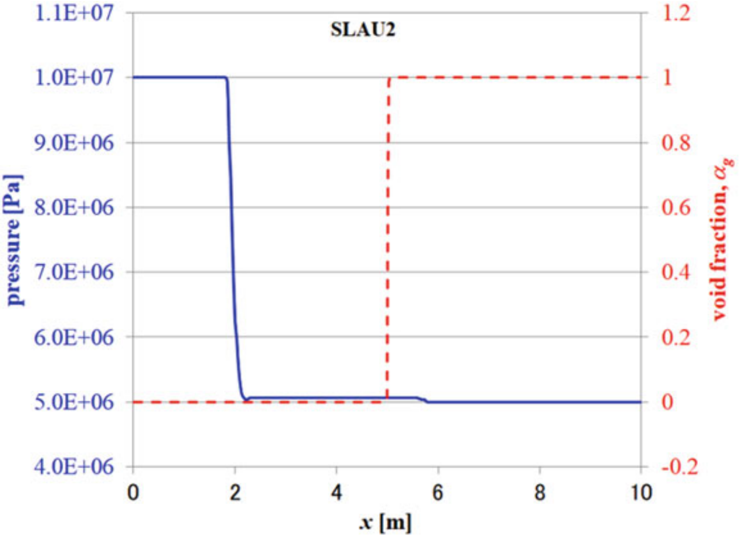

Fig. 4.12 Water-to-air shock tube problem solutions at $t = 2$ ms, SLAU2

The result of SLAU2 in Fig. 4.12 seemed free of oscillations, demonstrating a reasonable capturing of the rarefaction wave, a smooth transition at the phase interface, and robust capturing of the shock. It is demonstrated in [22] that the Godunov solver helped increase the smoothness of these profiles in the G-SLAU2 (not shown here). In addition, if the pressure ratio is raised from 2 (present) to 1000, the single SLAU2 or AUSM$^+$-up blows up (unless additional dissipation is added [49, 50]), whereas their combination with Godunov is successful [22].

4.1.9.4 Shock/Droplet Interaction

An air shock interacting with a water column (i.e., a 2D droplet) is simulated.

- 400 × 200 isotropic cells for a domain of [–5 mm, 5 mm] × [0 mm, 5 mm], covering the 6.4-mm-diameter water column with its center being located at the origin ($\Delta x_{\min} = \Delta y_{\min} = 0.025$ mm in this region)
- The cells are stretched toward the outer boundaries so that a domain of [–15 mm, 20 mm] × [0 mm, 15 mm] is filled with a total of 900 × 300 cells.

The initial conditions [30]:

- $x \leq -4$ mm: $(p, u_k, v_k, T_k, \alpha_g)_L = (2.35438 \times 10^5$ Pa, 225.86 m/s, 0 m/s, 381.85 K, $\varepsilon)$
- $x > -4$ mm: $(p, u_k, v_k, T_k, \alpha_g)_R = (1 \times 10^5$ Pa, 0 m/s, 0 m/s, 293.15 K, $\varepsilon)$, except for $x^2 + y^2 < (3.2\ \text{mm})^2$ in which $\alpha_g = 1 - \varepsilon$

where $\varepsilon = 1.0 \times 10^{-5}$ ($\varepsilon_{\min} = 1.0 \times 10^{-5}$, $\varepsilon_{\max} = 1.0 \times 10^{-4}$). Then the shock moves with $M_{sh} = 1.47$, and hits the droplet at $t \approx 1.5$ μs. The computations are conducted with $\Delta t = 1.25 \times 10^{-9}$ s (CFL ≈ 0.15) until 7.5 μs (6000 steps).

The SLAU2 solutions are displayed at $t = 7.5$ μs in Fig. 4.13. SLAU2 captured large-scale structures, and the solution appeared to be fair.

In summary, the single AUSM-family SLAU2 can be used for this challenging 2D shock/water-column interaction problem, at least at the early stages (to proceed

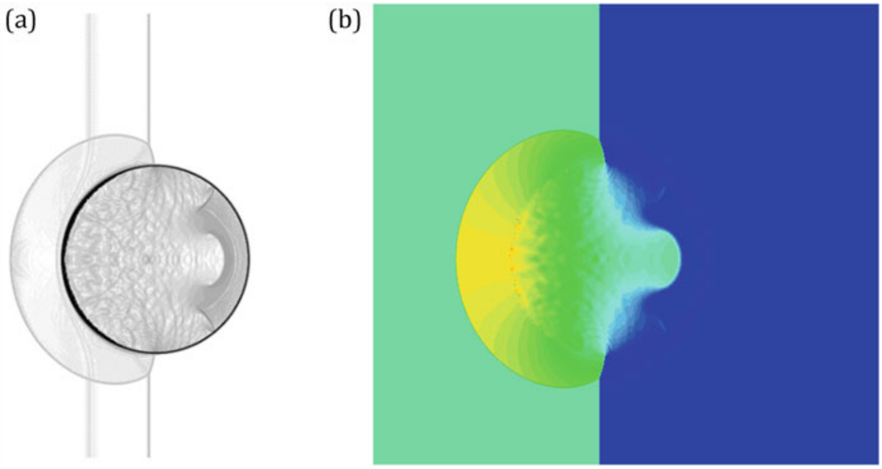

Fig. 4.13 Time evolution of solution of shock/water-droplet interaction problem of SLAU2: (**a**) $t = 7.5$ μs (numerical Schlieren); (**b**) $t = 7.5$ μs (pressure)

further in time evolution, a finer mesh is required to resolve small-scale structures). The Godunov-combined methods, on the contrary, were able to compute this problem longer with this initial grid.

4.1.9.5 Shock/Air-Bubble Interaction

A shock in water impacts a column of an air (i.e., 2D bubble), with very high pressure ratio (1.6×10^4).

- $x \leq -4$ mm: $(p, u_k, v_k, T_k, \alpha_g)_L = (1.6 \times 10^9$ Pa, 661.81 m/s, 0 m/s, 595.13 K, $1 - \varepsilon)$
- $x > -4$ mm: $(p, u_k, v_k, T_k, \alpha_g)_R = (1.01325 \times 10^5$ Pa, 0 m/s, 0 m/s, 292.98 K, $1 - \varepsilon)$, except for $x^2 + y^2 < 3.2$ mm^2 in which $\alpha_g = \varepsilon = 1.0 \times 10^{-3}$ ($\varepsilon_{\min} = 1.0 \times 10^{-3}$, $\varepsilon_{\max} = 1.0 \times 10^{-1}$)
  with $\Delta t = 3.125 \times 10^{-10}$ s (CFL ≈ 0.05) until 5.0 μs (16,000 steps).

The shock travels with $M_{sh} = 1.51$ and hits the air bubble at $t \approx 0.3$ μs. The result of G-SLAU2 is shown in Fig. 4.14; SLAU2 and AUSM$^+$-up standalone (i.e., without Godunov or HLLC) cases blew up immediately after the shock hit the bubble, in this severe case. Details of solutions are explained by Chang and Liou in [23].

All in all, it has been demonstrated from all the above problems that SLAU2 (AUSM-family flux) has been successfully extended within the two-fluid framework [23, 30] and provide reliable results including shock/water-column or shock/air-bubble interaction.

4.1.10 Multiphase Flows Summary

In this section, the extension of SLAU2 (AUSM-family numerical flux function) to compressible multiphase-flow computations is introduced with numerical evidence, based on the stratified flow model concept, following Liou et al. [30] (in which AUSM$^+$-up was used stand-alone) and Chang and Liou [23] (in which the exact Riemann solver was combined).

Currently, the following two works are in progress:

1. Inspired by "AUSM+-upf" flux [49], we are trying to design an enhanced SLAU2 that can handle strong phase/shock discontinuities without calling for Godunov or HLLC at phase discontinuities [50].
2. HLLC expressed in an AUSM-form [51] will bridge the gap between SLAU2 and HLLC in two-fluid modeling, which will eventually lead to a unified method.

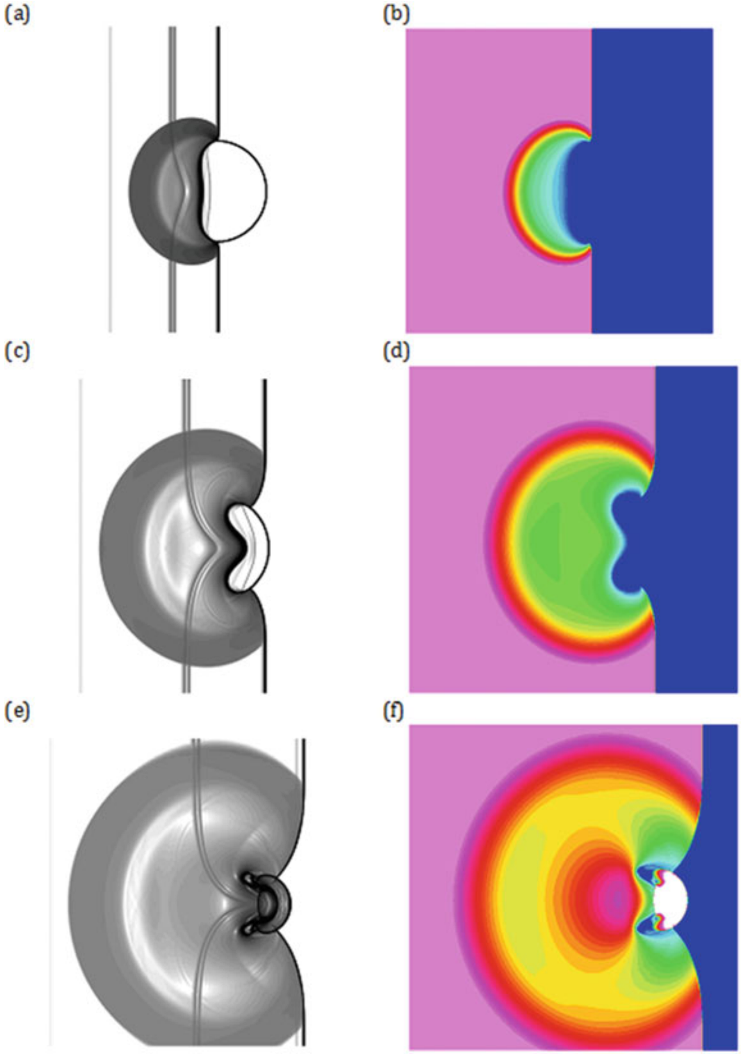

Fig. 4.14 Transient solutions of shock/air-bubble of G-SLAU2: (**a**) $t = 1.875$ μs (numerical Schlieren); (**b**) $t = 1.875$ μs (pressure); (**c**, **d**) $t = 3.15$ μs; (**e**, **f**) $t = 4.375$ μs

4.2 Supercritical Fluids

4.2.1 Supercritical Fluids and FVM

The air flows are typically treated as a perfect gas under standard conditions, and also at high-temperature, high-pressure conditions . On the other hand, supercritical (= beyond the critical temperature and critical pressure) [52] (Fig. 4.15a) fluids may

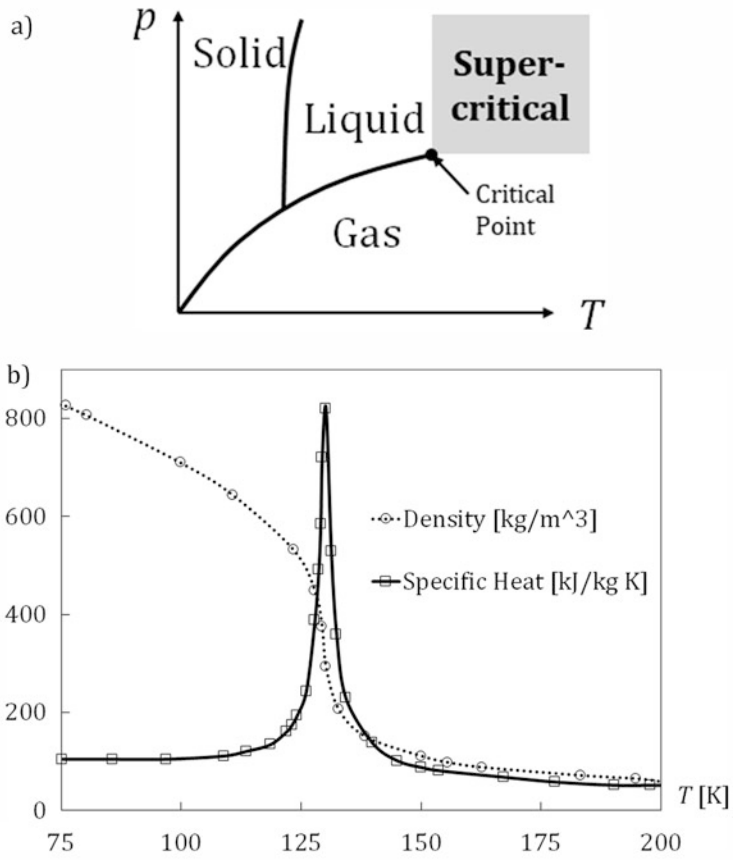

Fig. 4.15 (**a**) Schematic of supercritical fluids, and (**b**) density and specific heat of N_2 (4 MPa, around the supercritical temperature)

appear in a liquid rocket engine, for instance, which exhibit large differences from the perfect gas due to the highly nonlinearity of thermodynamic properties (Fig. 4.15b). Simulation technologies for such extreme conditions of a real EoS have not been fully established yet, and investigations are still ongoing [48, 53, 54].

In particular, unphysical pressure oscillations are reported at a contact surface between cryogenic and standard-temperature supercritical fluids. We tried to cure this problem by solving the "non-conservative" *pressure evolution equation* rather than the conservative equation for the total energy ("fully conservative form," hereafter). The motivations for this are stated below.

Terashima and Koshi [54] proposed the use of the *pressure evolution equation* [55, 56] instead of the *energy equation* (the total energy conservation equation). This (mass, momentum, and *pressure*)-form explicitly satisfies equilibriums of both velocity and pressure. Note that, however, Terashima and Koshi [54] adopted a structured-grid-based, higher-order method. Higher-order methods for unstructured grids (e.g., [57]) have been enthusiastically studied, but they are usually based on the fully conservative form.

If the *pressure evolution equation* is solved instead of the energy conservation equation, the pressure equilibrium will be explicitly guaranteed, and its oscillations will be removed. Therefore, in the present section, we will introduce our recent work which employed the *pressure evolution equation* and designed a new (mass, momentum, and *pressure*)-formulation for SLAU2 [40].

As already mentioned in Chap. 3, the authors have proposed SLAU [37] and SLAU2 [40] (and variants) [36]. These two are almost the same, but SLAU2 features numerical dissipation which (1) grows with the Mach number at supersonic speeds, and (2) is extendable to fluids other than the perfect gas. Thus, SLAU2 is expected to be extended to supercritical flows (Fig. 4.15b) expressed by the Soave–Redlich–Kwon (SRK) EoS [58]. The SRK EoS is widely used for supercritical flows, which is represented by a cubic equation with two constants, showing strong nonlinearity as in Fig. 4.15b.

We emphasize again that numerical flux functions such as SLAU2 can be directly used on unstructured grids [59–62] in practical three-dimensional simulations (e.g., [56, 63, 64]) for complicated geometries.

4.2.2 Governing Equations for Supercritical Fluids

4.2.2.1 Euler or Navier–Stokes Equations

In the conservative form, the governing equations are the same as those of the standard compressible gases (with the different EoS in Sect. 4.2.2.2 to close these equations).

$$\left.\begin{aligned} &\frac{\partial \mathbf{Q}}{\partial t}+\frac{\partial \mathbf{F}_k}{\partial x_k}=0 && :\text{Euler}\\ &\frac{\partial \mathbf{Q}}{\partial t}+\frac{\partial \mathbf{F}_k}{\partial x_k}=\frac{\partial \mathbf{Fv}_k}{\partial x_k} && :\text{Navier}-\text{Stokes}\end{aligned}\right\} \tag{4.45}$$

$$\mathbf{Q}=\begin{bmatrix}\rho\\ \rho u_l\\ \rho E\end{bmatrix},\ \mathbf{F}_k=\begin{bmatrix}\rho u_k\\ \rho u_l u_k+p\delta_{lk}\\ \rho u_k H\end{bmatrix},\ \mathbf{Fv}_k=\begin{bmatrix}0\\ \tau_{lk}\\ u_m\tau_{mk}+\kappa\dfrac{\partial T}{\partial x_k}\end{bmatrix} \tag{4.46}$$

$$\tau_{lk}=\mu\left(\frac{\partial u_l}{\partial x_k}+\frac{\partial u_k}{\partial x_l}\right)-\frac{2}{3}\mu\frac{\partial u_n}{\partial x_n}\delta_{lk} \tag{4.47}$$

where $k, l, m, n = 1{,}2$ in 2D. The molecular viscosity μ and the thermal conductivity κ for supercritical fluids are calculated according to [65], whereas $\mu = \kappa = 0$ in the inviscid case.

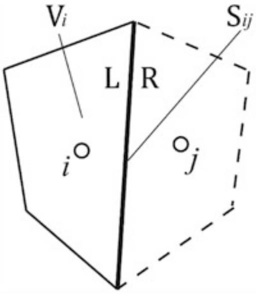

Fig. 4.16 Schematic of cell geometric properties

These equations are discretized by FVM, and can be written as follows (Fig. 4.16).

$$\frac{V_i}{\Delta t}\Delta\mathbf{Q}_i+\sum_j\left(\mathbf{F}_{i,j}-\mathbf{Fv}_{i,j}\right)S_{i,j}=0 \tag{4.48}$$

In the non-conservative treatment here, the energy equation (last line in Eq. (4.45)) can be replaced with the following *pressure evolution equation* [54, 66].

$$\frac{\partial p}{\partial t}+u_k\frac{\partial p}{\partial x_k}+\rho a^2\frac{\partial u_k}{\partial x_k}=\left(\frac{\partial p}{\partial e}\right)_\rho\cdot\left(\frac{1}{\rho}\frac{\partial}{\partial x_k}\left(u_m\tau_{mk}+\kappa\frac{\partial T}{\partial x_k}\right)\right) \tag{4.49}$$

where a is the speed of sound, and its derivation is given in Sect. 4.2.2.3. This is rewritten as follows, in a conservation form that is more suitable for the FVM:

$$\frac{\partial p}{\partial t}+\frac{\partial(pu_k)}{\partial x_k}+\left(\rho a^2-p\right)\frac{\partial u_k}{\partial x_k}=\left(\frac{\partial p}{\partial e}\right)_\rho\cdot\left(\frac{1}{\rho}\frac{\partial}{\partial x_k}\left(u_m\tau_{mk}+\kappa\frac{\partial T}{\partial x_k}\right)\right) \tag{4.50}$$

where e is the internal energy per unit mass ($e = E - 0.5u_i^2$). The R.H.S. is the viscous term, which is similar to that of the energy equation. Equation (4.50) is then discretized as

$$\begin{aligned}&\frac{V_i}{\Delta t}\Delta p_i+\sum_j(pu)_{i,j}S_{i,j}+\left(p_ia_i^2-p_i\right)\sum_j(u)_{i,j}S_{i,j}\\&=\left(\left(\frac{\partial p}{\partial e}\right)_\rho\right)_i\cdot\frac{1}{\rho_i}\sum_j\left(u_m\tau_{mk}+\kappa\frac{\partial T}{\partial x_n}\right)_{i,j}S_{i,j}\end{aligned} \tag{4.51}$$

where u is assumed outward normal to the cell interface i,j, for brevity. As can be seen, Eq. (4.51) has a very similar form to Eq. (4.48). In the R.H.S. of Eq. (4.51), the part $\sum_j\left(u_m\tau_{mk}+\kappa\frac{\partial T}{\partial x_n}\right)_{i,j}S_{i,j}$ corresponds to the fully conservative form of the viscous term. The part $\left(\left(\frac{\partial p}{\partial e}\right)_{\rho}\right)_{i} \cdot \frac{1}{\rho_i}$ is calculated as explained in [52] and [64]. To close the above equations under supercritical conditions, the SRK EoS below is employed.

4.2.2.2 SRK EoS

The SRK EoS [58] is expressed as follows:

$$p = \frac{RT}{V - B} - \frac{A(T)}{V^2 + BV} \tag{4.52}$$

$$A(T) = \frac{0.042747 R^2 T_{cr}^2}{p_{cr}} \cdot \left\{1 + f_{\omega} \cdot \left(1 - \sqrt{\frac{T}{T_{cr}}}\right)^2\right\} \tag{4.53}$$

$$B = \frac{0.08664 R T_{cr}}{p_{cr}} \tag{4.54}$$

$$f_{\omega} = 0.48 + 1.574\omega - 0.176\omega^2 \tag{4.55}$$

where T_{cr} and p_{cr} are the critical temperature and critical pressure, respectively (Table 4.1), and ω is the acentric factor ($\omega = 0.0372$ for nitrogen). The (universal) gas constant $R = 8.3144$ J/(mol K). The specific volume V is $V = W/\rho$, in which ρ is the density and W is the molecular weight ($W = 0.028$ kg/mol for nitrogen).

4.2.2.3 Pressure Evolution Equation

The mass conservation equation can be written as

$$\frac{\partial \rho}{\partial t} + u_k \frac{\partial \rho}{\partial x_k} = -\rho \frac{\partial u}{\partial x_k} \tag{4.56}$$

The energy equation

$$\frac{\partial (\rho E)}{\partial t} + \frac{\partial (\rho u_k H)}{\partial x_k} = \frac{\partial}{\partial x_k}\left(u_m \tau_{mk} + \kappa \frac{\partial T}{\partial x_k}\right) \tag{4.57}$$

is, after some manipulations, expressed as follows [54] using the internal energy e:

Table 4.1 Critical values for nitrogen [69]

T_{cr} [K]	p_{cr} [MPa]	ρ_{cr} [kg/m^3]
126.2	3.4	313.3

$$\frac{\partial e}{\partial t}+u_k\frac{\partial e}{\partial x_k}=-\frac{p}{\rho}\frac{\partial u_k}{\partial x_k}+\frac{1}{\rho}\frac{\partial}{\partial x_k}\left(u_m\tau_{mk}+\kappa\frac{\partial T}{\partial x_k}\right) \tag{4.58}$$

On the other hand, the substantial derivative (= convective derivative) of the pressure is given by

$$\frac{Dp}{Dt}=\left(\frac{\partial p}{\partial \rho}\right)_e\frac{D\rho}{Dt}+\left(\frac{\partial p}{\partial e}\right)_\rho\frac{De}{Dt} \tag{4.59}$$

which is the non-conservative form of the pressure equation. This is further rewritten as

$$\begin{aligned}\frac{Dp}{Dt}&=\left(\frac{\partial p}{\partial \rho}\right)_e\left(-\rho\frac{\partial u_k}{\partial x_k}\right)+\left(\frac{\partial p}{\partial e}\right)_\rho\left(-\frac{p}{\rho}\frac{\partial u_k}{\partial x_k}+\frac{1}{\rho}\frac{\partial}{\partial x_k}\left(u_m\tau_{mk}+\kappa\frac{\partial T}{\partial x_k}\right)\right)\\&=-\rho a^2\frac{\partial u_k}{\partial x_k}+\left(\frac{\partial p}{\partial e}\right)_\rho\left(\frac{1}{\rho}\frac{\partial}{\partial x_k}\left(u_m\tau_{mk}+\kappa\frac{\partial T}{\partial x_k}\right)\right)\end{aligned} \tag{4.60}$$

where $a=\sqrt{\left(\frac{\partial p}{\partial \rho}\right)_e+\frac{p}{\rho^2}\left(\frac{\partial p}{\partial e}\right)_\rho}$ is the speed of sound. The *pressure evolution equation*

$$\frac{\partial p}{\partial t}+u_k\frac{\partial p}{\partial x_k}+\rho a^2\frac{\partial u_k}{\partial x_k}=\left(\frac{\partial p}{\partial e}\right)_\rho\cdot\left(\frac{1}{\rho}\frac{\partial}{\partial x_k}\left(u_m\tau_{mk}+\kappa\frac{\partial T}{\partial x_k}\right)\right) \tag{4.50$'$}$$

has now been derived.

4.2.3 Conventional SLAU2 and Pressure-Equation-Based SLAU2

4.2.3.1 Conventional SLAU2 (Brief Review)

SLAU2 [40] based on Eqs. (4.44)–(4.48), is written as

$$\boldsymbol{F}_{SLAU2}=\frac{\dot{m}+|\dot{m}|}{2}\boldsymbol{\Psi}^{+}+\frac{\dot{m}-|\dot{m}|}{2}\boldsymbol{\Psi}^{-}+\mathbf{P} \tag{4.61}$$

$$\boldsymbol{\Psi}=(1,\ u,\ v,\ H)^T,\quad \mathbf{P}=\left(0,\quad p_{1/2},\quad 0,\quad 0,\right)^T \tag{4.62}$$

Differences among the AUSM-family fluxes are based upon formulations of the mass flux $\dot{m}$ and pressure flux $p_{1/2}$. For SLAU2, $\dot{m}$ is

$$(\dot{m})_{SLAU} = \frac{1}{2}\left\{\rho_L\left(u_L + \left|\overline{V}_n\right|^+\right) + \rho_R\left(u_R - \left|\overline{V}_n\right|^-\right) - \frac{\chi}{a_{1/2}}\Delta p\right\} \tag{4.63}$$

$$\left|\overline{V}_n\right|^+ = (1-g)\left|\overline{V}_n\right| + g|u_L|, \left|\overline{V}_n\right|^- = (1-g)\left|\overline{V}_n\right| + g|u_R| \tag{4.64}$$

$$\left|\overline{V}_n\right| = \frac{\rho_L|u_L| + \rho_R|u_R|}{\rho_L + \rho_R} \tag{4.65}$$

$$g = -\max\left[\min\left(M_L, 0\right), -1\right] \cdot \min\left[\max\left(M_R, 0\right), 1\right] \in [0, 1] \tag{4.66}$$

where L denotes the left side of the cell interface, and R denotes the right side, and

$$\chi = \left(1 - \widehat{M}\right)^2 \tag{4.67}$$

$$\widehat{M} = min\left(1.0, \frac{1}{a_{1/2}}\sqrt{\frac{\boldsymbol{u}_L{}^2 + \boldsymbol{u}_R{}^2}{2}}\right) \tag{4.68}$$

$$M = \frac{u}{a_{1/2}} \tag{4.69}$$

$$a_{1/2} = \overline{a} = \frac{a_L + a_R}{2} \tag{4.70}$$

and the pressure flux $p_{1/2}$ is given as

$$\begin{aligned} p_{1/2(SLAU2)} &= \frac{p_L + p_R}{2} + \frac{\mathrm{P}^+|_{\alpha=0} - \mathrm{P}^-|_{\alpha=0}}{2}(p_L - p_R) + \sqrt{\frac{\boldsymbol{u}_L{}^2 + \boldsymbol{u}_R{}^2}{2}} \\ &\quad \cdot \left(\mathrm{P}^+|_{\alpha=0} + \mathrm{P}^-|_{\alpha=0} - 1\right)\overline{\rho}a_{1/2} \end{aligned} \tag{4.71}$$

$$\mathrm{P}^{\pm}|_{\alpha} = \begin{cases} \frac{1}{2}(1 \pm sign(M)), & if|M| \geq 1 \\ \frac{1}{4}(M \pm 1)^2(2 \mp M) \pm \alpha M\left(M^2 - 1\right)^2, & otherwise \end{cases} \tag{4.72}$$

$$\overline{\rho} = \frac{\rho_L + \rho_R}{2} \tag{4.73}$$

where $\alpha = 0$ in SLAU2. As one of the differences from SLAU [37], the last term of Eq. (4.71) is applicable to real fluids in SLAU2.

4.2.3.2 Pressure-Equation-Based SLAU2

Once the primitive variables are reconstructed, an AUSM-family flux (e.g., SLAU2) requires *no change in the mass and momentum equations* to demonstrate the constancy of velocity and pressure in an inviscid (u, p)-equilibrium flow. Thus, our primary target here is to improve the construction of the pressure equation part.

According to Eq. (4.51), the normal outward velocity $u_{i,j}$ needs to be determined. Remembering that the mass flux of the AUSM family is given in an upwind manner, we can define the cell-interfacial normal velocity u in the simplest form as

$$u = \begin{cases} \dfrac{\dot{m}}{\rho_L} & \mathit{if}\ \dot{m} \geq 0 \\ \dfrac{\dot{m}}{\rho_R} & \mathit{otherwise} \end{cases} \tag{4.74}$$

Then, there may be several options to obtain $(p_{i,j}u_{i,j})$. In accordance with our preliminary numerical tests, a simple upwinding is adopted.

$$(pu) = \begin{cases} \dfrac{\dot{m}}{\rho_L} p_L & \mathit{if}\ \dot{m} \geq 0 \\ \dfrac{\dot{m}}{\rho_R} p_R & \mathit{otherwise} \end{cases} \tag{4.75}$$

Now temporal pressure oscillations are theoretically zero, in the (u, p)-equilibrium, inviscid flow. In the coding, it is recommended to replace the last component in the energy equation, Eq. (4.61), with

$$u = \frac{\dot{m} + |\dot{m}|}{2} \frac{1}{\rho_L} + \frac{\dot{m} - |\dot{m}|}{2} \frac{1}{\rho_R} \tag{4.76}$$

$$(pu) = \frac{\dot{m} + |\dot{m}|}{2} \frac{p_L}{\rho_L} + \frac{\dot{m} - |\dot{m}|}{2} \frac{p_R}{\rho_R} \tag{4.77}$$

These will be substituted in Eq. (4.51). The pressure is then evolved in time.

4.2.4 Computational Example for Supercritical Fluids

A numerical example in [48] is solved using the aforementioned methods, namely, either the conventional or *pressure-equation-based* SLAU2 ([66] shows other examples such as [54, 67]). The spatial order of accuracy is two, obtained by a MUSCL extrapolation with $\kappa = 1/3$ [31] along with the minmod limiter [68]. The two-stage, second-order Runge-Kutta method is used for the time integration.

The critical temperature, critical pressure, and critical density for nitrogen [69] are summarized in Table 4.1.

The SRK EoS subroutines used for our simulations were already validated in [48]. Nevertheless, we have confirmed that it also works properly in our own code and that the computed values agree well with National Institute of Standards and Technology (NIST) data [69].

4.2.4.1 2D Cryogenic Nitrogen Jet

We apply SLAU2 to a 2D cryogenic nitrogen jet which is injected into standard-temperature nitrogen [54]. As already mentioned by Terashima and Koshi [54], no experimental data are available for such severe conditions. Thus, our objective here is not to fully resolve the physics in detail, but rather to demonstrate that the proposed *pressure-equation-based* SLAU2 can deal with this problem without unphysical errors. The numerical conditions are consistent with those in Terashima and Koshi [54], that is,

$$(\rho, u, v, T, p)_{jet} = \left(850\ \mathrm{kg/m^3}, 100\ \mathrm{m/s}, 0\ \mathrm{m/s},\ \ 71.5\ \mathrm{K}, 5.0\ \mathrm{MPa}\right)$$

$$(\rho, u, v, T, p)_{ambient} = \left(50\ \mathrm{kg/m^3}, 0\ \mathrm{m/s}, 0\ \mathrm{m/s},\ \ 332.2\ \mathrm{K}, 5.0\ \mathrm{MPa}\right)$$

Initially, the ambient condition is applied to the entire computational domain. The boundary conditions are the inlet at the left, the outlet (with specified pressure) at the right, and the periodic at the top and the bottom. The jet exit height h is 1 mm (-0.5 mm $< y <$ 0.5 mm in Fig. 4.17). The jet condition $\mathbf{q}_{jet} = (\rho, u, v, p)_{jet}$ and its ambient $\mathbf{q}_{ambient} = (\rho, u, v, p)_{ambient}$ are smoothly connected by the error function [48, 54]; i.e.,

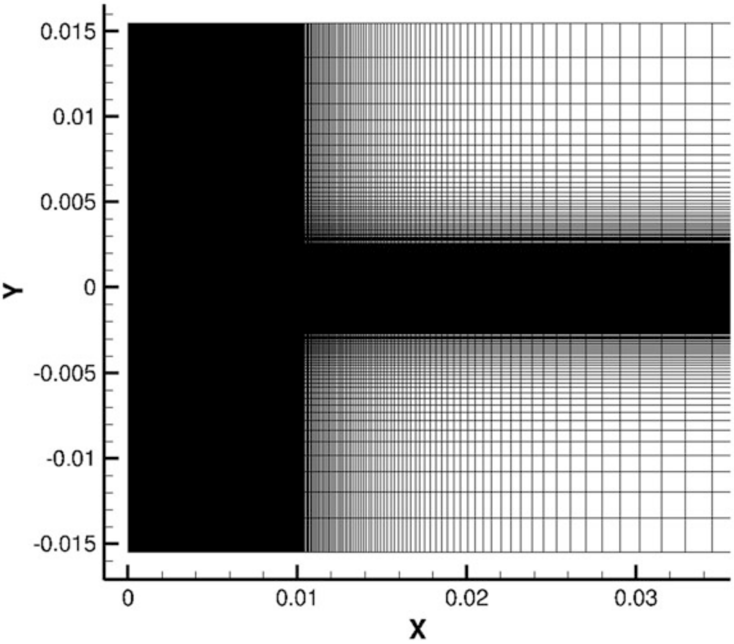

Fig. 4.17 Computational grid for 2D cryogenic N_2 jet under supercritical pressure (close-up around the jet exit)

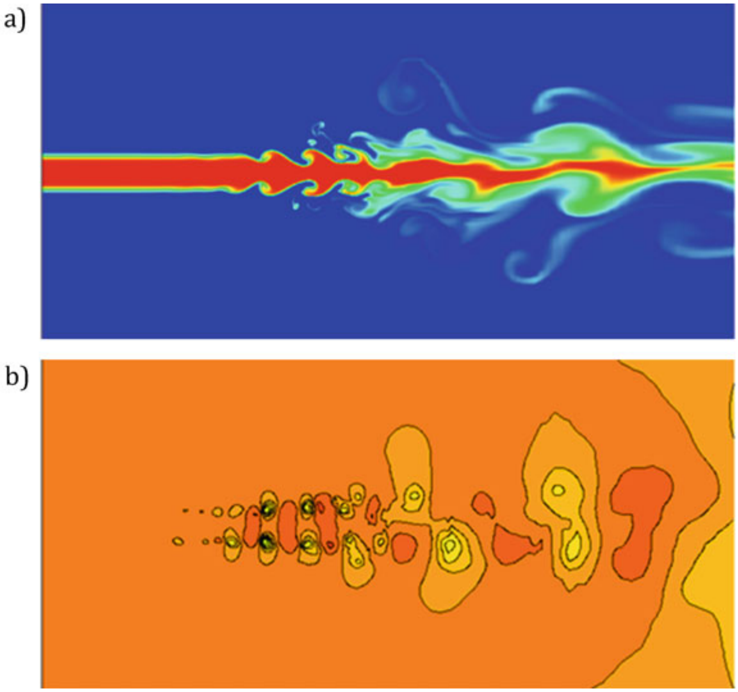

Fig. 4.18 Computed flow fields at $t = 3.96 \times 10^{-4}$ s (2D cryogenic nitrogen jet under supercritical pressure) by *pressure-equation-based* SLAU2: (**a**) density ($45 < \rho < 852$) [kg/m^3], (**b**) pressure ($2.7 < p < 5.31$) [MPa]

$$\mathbf{q} = \mathbf{q}_{ambient}(1 - f_{sm}) + \mathbf{q}_{jet} f_{sm} \tag{4.78}$$

$$f_{sm} = \frac{1}{2}\left\{1 + erf\left(\frac{|y - (h/2)|}{C_\varepsilon \Delta s}\right)\right\} \tag{4.79}$$

are imposed on the entire left boundary, where y is zero at the jet center, Δs is the minimum grid spacing $\Delta s = 0.0125h$. A user-defined parameter C_ε is set at $C_\varepsilon = 9.0$ ($C_\varepsilon\ \Delta s =$ is the same as in [54]) (the smaller the value of C_ε, the sharper the interface). Another value of C_ε is used in [66].

The computational grid (Fig. 4.17) consists of 800 × 400 cells in the (x, y) directions, respectively, covering the domain of $[0, 82.5h] \times [-15.5h, 15.5h]$. We employ the spatially second-order method on a denser grid than [54], especially near the jet. The simulation is carried out with $\Delta t = 5.0 \times 10^{-9}$ s (CFL ≈ 0.4) until $t = 3.96 \times 10^{-4}$ s (79,200 steps).

The solution computed by the *pressure-evolution-based* SLAU2 is shown in Fig. 4.18. As the jet develops, an asymmetry appears in the density profile (Fig. 4.18a) [54], without pressure oscillations (Fig. 4.18b). On the other hand, the conventional SLAU2 diverged within initial few steps.

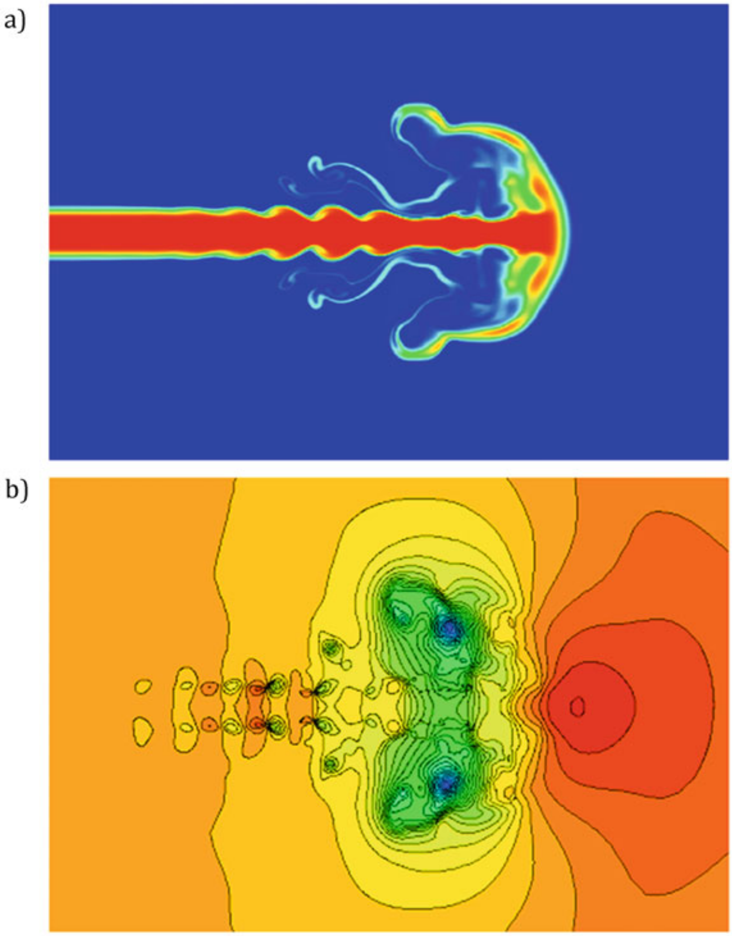

Fig. 4.19 Computed flow fields at $t = 1.50 \times 10^{-4}$ s (cryogenic nitrogen 2D jet under supercritical pressure) by original SLAU2: (**a**) density ($45 < \rho < 852$) [kg/m^3], (**b**) pressure ($3.9 < p < 5.2$) [MPa]

To make clearer comparisons between these two methods, (i) solutions at 30,000 steps ($t = 1.50 \times 10^{-4}$ s) with the *pressure-equation-based* SLAU2 (Fig. 4.19) and (ii) solutions at the same 30,000 steps in which the *pressure-equation-based* SLAU2 was used until 10,000 steps, after which the conventional SLAU2 continued for the remaining 20,000 steps (Fig. 4.20), are shown. The density profiles (Figs. 4.19a and 4.20a) look different, but no unphysical oscillations are observed. However, the pressure profiles are remarkably different (Figs. 4.19b and 4.20b), especially because of pressure oscillations in the conventional SLAU2 (Fig. 4.20b). From those results, the superiority of the *pressure-equation-based* SLAU2 has been confirmed. An extension to three dimensions is straightforward (such as in [63, 64]).

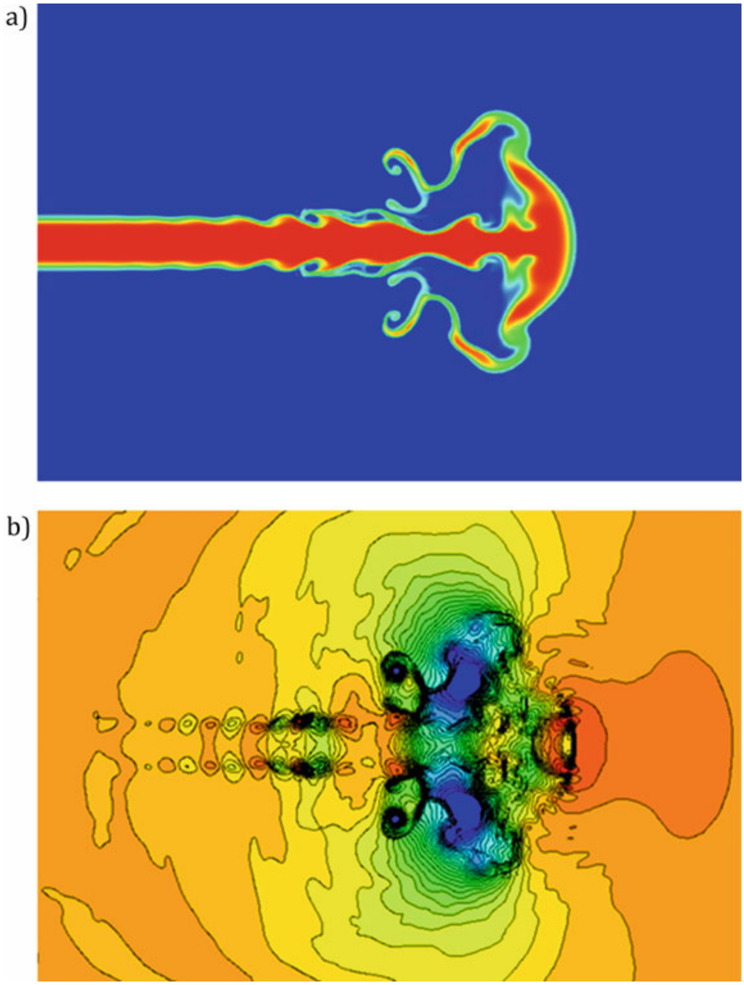

Fig. 4.20 Computed flow fields at $t = 1.50 \times 10^{-4}$ s (cryogenic nitrogen 2D jet under supercritical pressure) by original SLAU2: (**a**) density ($45 < \rho < 852$) [kg/m^3], (**b**) pressure ($3.9 < p < 5.2$) [MPa]

4.2.5 Summary of Supercritical Fluids

It has been demonstrated that the *pressure-equation-based* SLAU2 can successfully handle supercritical flows, within the second-order FVM. Only marginal corrections to the existing method are required, without the need to rely upon higher-order methods or artificial viscosities. This is a strong advantage in practical simulations, because the second-order FVM is readily applicable to three-dimensional complex geometries. Thus, we hope to apply the present method to internal-engine combustion flows in the future. It is also noteworthy that comparable results were obtained using another AUSM-type flux (HLLCL) using the *pressure-equation-based* expression [51].

4.3 Magnetohydrodynamics (MHD)

4.3.1 Compressible, Ideal MHD: Current Status and Proposed Improvements

Continued attention is paid to accurate, robust, yet economical magnetohydrodynamics (MHD) simulations such as in the astrophysics [70–72], aerospace engineering [73], and nuclear engineering communities [74, 75]. To perform such simulations, it is critical to establish and/or employ a reliable numerical method in each part of the computational process, i.e., reconstruction methods [31, 76], slope limiters [68], numerical flux functions [40, 77–79], time integration methods [45], and divergence treatments [81–85]. In this section, particular attention will be paid to the flux functions, because they significantly affect numerical solutions also in MHD: solution quality can be degraded by certain flux functions [39], and in the worst-case scenario, a captured shockwave can collapse [85, 86]. Let us categorize these flux functions into four groups according to the number of resolved waves and their responses to the shocks, as shown in Fig. 4.21, including the AUSM-family fluxes (Fig. 4.22).

- Group I: 7-wave solvers (or full-wave solvers) include Roe [87–91] (extended from gas dynamics [77]) and HLLI (Harten–Lax–van Leer with Intermediate waves) [92]. They capture all the seven waves (left/right fast waves, left/right Alfvén waves, left/right slow waves, and an entropy wave) in MHD. They are accurate, but tend to produce anomalous solutions at the captured shocks (e.g., the "*carbuncle*" phenomena [85, 86]), as pointed out by many researchers in gas dynamics [93–101] and MHD [72]. Furthermore, treating all the seven waves in MHD is numerically expensive.
- Group II: Five-wave solver corresponds with HLLD (Harten–Lax–van Leer with Discontinuities) [78]. This is an extended version of HLLC from gas dynamics, which captures left/right fast waves, left/right Alfvén waves, and the entropy wave. Although this solver omits slow waves, it produces satisfactory solutions [102–104].
- Group III: Three-wave solvers. AUSM (Advection Upstream Splitting Method)-type solvers [105–107], E-CUSP (Energy-conservative Convective-Upwind and Split-Pressure) [108], and HLLC [109, 110] belong to this category. These recent AUSM solvers inherit the spirit of the earlier AUSM; i.e., they possess both the simplicity of flux vector splitting (FVS) (e.g. van Leer's [111]) and the contact-resolving nature of FDS (e.g., Roe). In MHD, they treat the left/right fast waves (i.e., the sound waves in gas dynamics) and the entropy wave. In addition to this

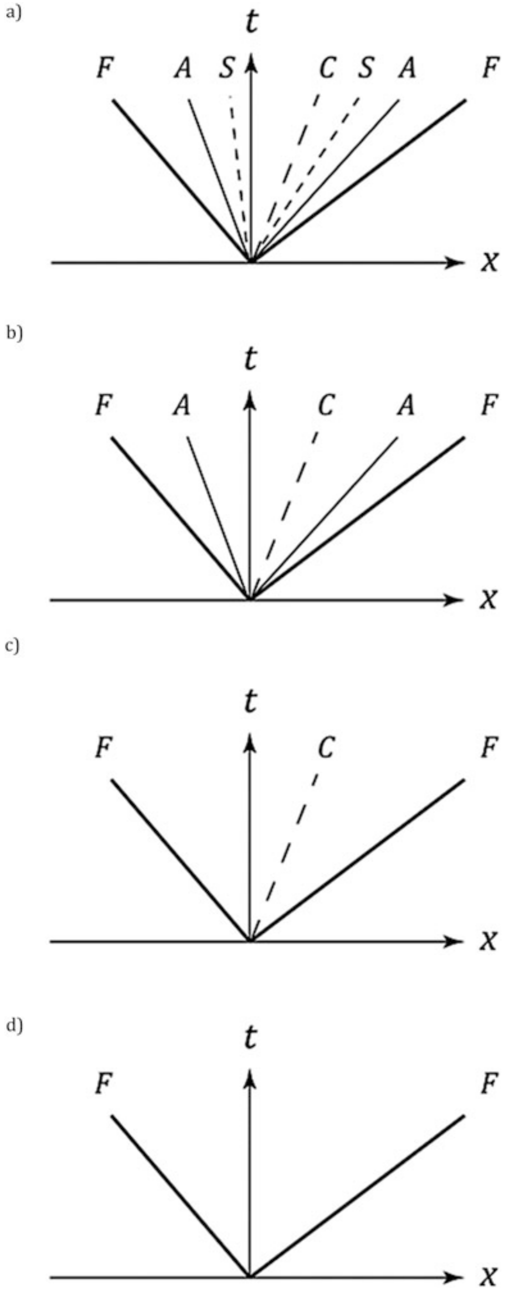

Fig. 4.21 Numerical flux functions in MHD (F: fast wave, A: Alfvén wave, S: slow wave, and C: contact discontinuity): (**a**) 7-wave solvers (Roe, HLLI), (**b**) 5-wave solver (HLLD), (**c**) 3-wave solvers (SLAU2, AUSMPW+, E-CUSP, HLLC), and (**d**) 2-wave solver (HLL)

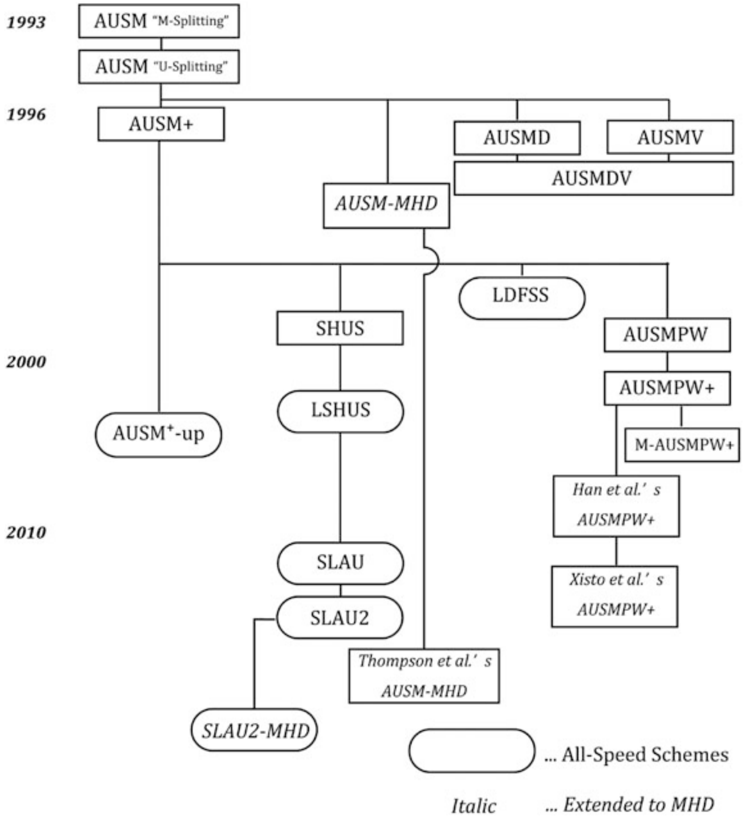

Fig. 4.22 AUSM family tree for MHD

simplification, they eliminate the need for complicated Eigensystems in MHD for *efficiency*. AUSMPW+ (AUSM by Pressure-based Weight functions +) [41] was applied to MHD by Han et al. [107], and later further extended in [105, 106]. SLAU2 [40] was extended to MHD in [105, 112]. They are known to be *very robust* against the shock anomalies in gas dynamics [40, 96, 98]. In addition, they can capture the contact discontinuity and boundary layers *accurately* [40, 41]. E-CUSP [113] has a structure similar to that of the AUSM-type fluxes and was extended to MHD in [108]. HLLC, on the other hand, is known to be as vulnerable as the Roe solver to the carbuncle [95, 114], probably because it can be written in a very similar manner to the Roe solver in the Eigenmatrix-free expression [115, 116]. Li [109] and Gurski [110] tried to extend HLLC [117] to MHD in the three-wave framework.

- Group IV: Two-wave solvers are represented by (2-wave) HLL [79], Rusanov (or also known as Local Lax Friedrich) [118], and typical FVS methods. An MHD-extended HLL was proposed in [119]. These solvers omit the entropy wave, and resolve only the left/right fastest waves (i.e., sound waves in gas dynamics). In contrast with the Roe flux, however, they are very robust in capturing shocks, again as explained in [93]. In ATHENA [103] code, HLL is hybridized with Roe or HLLD such that HLL is used at the shocks only in a multidimensional manner [86, 95, 120], although the universality of such techniques is questionable [96, 121].

As reviewed above, AUSM-type solvers in Group III appear to be promising because they feature *robustness, accuracy, efficiency, and simplicity* by itself. Specifically, SLAU2 is today utilized by many practitioners and incorporated in many numerical codes, such as FaSTAR [122], LS-FLOW [123], and SU2 (Stanford University Unstructured code) [124]. It features robustness against the shock anomalies [40], and also the capability of all-speed (including in an incompressible regime, such as the solar convective zone [125–128] or International Thermonuclear Experimental Reactor (ITER) [74, 75]) flow computations [39]. Therefore, the SLAU2 in MHD is tested in 1D [105] and 2D MHD [112].

In multidimensions, it is reported that the treatment of divergence of the magnetic field is necessary. Among the many methods for a divergence-free treatment of the magnetic field ($\nabla\cdot\mathbf{B} = 0$) [80–84], we select a hyperbolic divergence-cleaning method [80] that is already incorporated in CANS+ [102], an open MHD code developed in Japan.

This section is organized as follows. Section 4.3.2 will describe the governing equations. In Sect. 4.3.3, its discretization, and the numerical methods to solve these equations will be presented, in particular SLAU2 in MHD. Next, 1D and 2D MHD numerical tests are presented in Sect. 4.3.4. Finally, Sect. 4.3.5 will summarize the present chapter.

4.3.2 Governing Equations for MHD

The governing equations are the compressible MHD equations as follows:

$$\frac{\partial \mathbf{Q}}{\partial t} + \frac{\partial \mathbf{F}}{\partial x} + \frac{\partial \mathbf{G}}{\partial y} + \frac{\partial \mathbf{H}}{\partial z} = 0 \tag{4.80}$$

$$\mathbf{Q} = \begin{bmatrix} \rho \\ \rho u \\ \rho v \\ \rho w \\ \rho E \\ B_x \\ B_y \\ B_z \end{bmatrix}, \mathbf{F} = \begin{bmatrix} \rho u \\ \rho u^2 + p_G - B_x^2 \\ \rho uv - B_x B_y \\ \rho uw - B_x B_z \\ \rho uH - B_x(\mathbf{u}\cdot\mathbf{B}) \\ 0 \\ uB_y - vB_x \\ uB_z - wB_x \end{bmatrix},$$

$$\mathbf{G} = \begin{bmatrix} \rho v \\ \rho vu - B_y B_x \\ \rho v^2 + p_G - B_y^2 \\ \rho vw - B_y B_z \\ \rho vH - B_y(\mathbf{u}\cdot\mathbf{B}) \\ vB_x - uB_y \\ 0 \\ vB_z - wB_y \end{bmatrix}, \mathbf{H} = \begin{bmatrix} \rho w \\ \rho wu - B_z B_x \\ \rho wv - B_z B_y \\ \rho w^2 + p_G - B_z^2 \\ \rho wH - B_z(\mathbf{u}\cdot\mathbf{B}) \\ wB_x - uB_z \\ wB_y - vB_z \\ 0 \end{bmatrix} \tag{4.81}$$

where $\mathbf{Q}$ is the vector of the conservative variables, ρ is the density, $\mathbf{u} = (u, v, w)^T$ is the velocity, p the gas pressure, p_G the total (or global) pressure ($p_G = p + B^2/2$), $\mathbf{B}$ the magnetic field [$B^2 = \mathbf{B}\cdot\mathbf{B}$; $\mathbf{B} = (B_x, B_y, B_z)^T$], E the total energy per unit mass [$E = (p/\rho)/(\gamma\text{-}1) + 0.5(u^2 + v^2 + w^2) + 0.5B^2/\rho$], and H the total enthalpy [$H = E + (p/\rho)$]. The gas is assumed to be calorically perfect with specific heat ratio γ. The first five equations are Euler equations, whereas the sixth to eighth equations comprise Faraday's law for MHD, which is a subset of the Maxwell equations. In 1D, the third and fourth terms are absent, and the sixth equation is dropped. The divergence-free requirement for the magnetic field ($\nabla\cdot\mathbf{B} = 0$) is then automatically satisfied, as long as $B_x =$ const. [107]. In multi-D, on the other hand, a scalar potential ψ is solved in a similar manner as a hyperbolic divergence-cleaning method [80].

Equation (4.80) is then solved with FVM written as

$$\Delta\mathbf{Q}_i = -\frac{\Delta t}{V}\left(\mathbf{F}_{i-1/2} - \mathbf{F}_{i+1/2}\right) \tag{4.82}$$

where $\Delta\mathbf{Q}_i$ is the change in the conservative variables over time. Details of the inviscid fluxes are explained in the following sections.

4.3.3 *Numerical Methods for MHD*

4.3.3.1 SLAU2 for MHD

As discussed in [105], the Euler equations (the gas flow part; the first equations of Eq. (4.80)) and Maxwell equations (the magnetic field; the sixth to eighth equations) are handled separately. Let us begin with the Euler equations part, i.e., the first five components of Eq. (4.80).

$$\begin{aligned}\mathbf{F}_{SLAU2(Euler)} &= \frac{\dot{m}+|\dot{m}|}{2}\boldsymbol{\Psi}^{+}_{Euler}+\frac{\dot{m}-|\dot{m}|}{2}\boldsymbol{\Psi}^{-}_{Euler}+\mathbf{P}_{Euler}\\ &\quad + B_{1/2}\frac{\boldsymbol{\Psi}^{+}_{Euler,B}+\boldsymbol{\Psi}^{-}_{Euler,B}}{2}\end{aligned} \tag{4.83}$$

$$\begin{aligned}&\boldsymbol{\Psi}^{+}_{Euler}=(1,u_L,v_L,w_L,H_L)^T;\boldsymbol{\Psi}^{-}_{Euler}=(1,u_R,v_R,w_R,H_R)^T,\\ &\boldsymbol{\Psi}^{+}_{Euler,B}=\left(0,-B_{xL},-B_{yL},-B_{zL},0\right)^T;\boldsymbol{\Psi}^{+}_{Euler,B}=\left(0,-B_{xR},-B_{yR},-B_{zR},0\right)^T\end{aligned} \tag{4.84}$$

$$\mathbf{P}_{Euler}=\begin{pmatrix}0\\ p_{1/2}\\ 0\\ 0\\ \mathrm{P}^{+}\cdot\left\{-\left(u_LB_{L,x}+v_LB_{L,y}+w_LB_{L,z}\right)B_{1/2}\right\}+\mathrm{P}^{-}\cdot\left\{-\left(u_RB_{R,x}+v_RB_{R,y}+w_RB_{R,z}\right)B_{1/2}\right\}\end{pmatrix} \tag{4.85}$$

$$\mathrm{P}^{+}=\begin{cases}\frac{1}{2}(1+sign(M_L)), & if|M_L|\geq 1\\ \frac{1}{4}(M_L+1)^2(2-M_L), & otherwise\end{cases} \tag{4.86}$$

$$\mathrm{P}^{-}=\begin{cases}\frac{1}{2}(1-sign(M_R)), & if|M_R|\geq 1\\ \frac{1}{4}(M_R-1)^2(2+M_R), & otherwise\end{cases} \tag{4.87}$$

where $B_{1/2}=\frac{B_{x,L}+B_{x,R}}{2}$ as in [107]. The mass flux is

$$(\dot{m})_{SLAU2}=\frac{1}{2}\left\{\rho_L\left(u_L+\left|\overline{V}_n\right|^{+}\right)+\rho_R\left(u_R-\left|\overline{V}_n\right|^{-}\right)-\frac{\chi}{\overline{c}}\left(p_{G,R}-p_{G,L}\right)\right\} \tag{4.88}$$

$$\left|\overline{V}_n\right|^{+}=(1-g)\left|\overline{V}_n\right|+g|u_L|,\left|\overline{V}_n\right|^{-}=(1-g)\left|\overline{V}_n\right|+g|u_R| \tag{4.89}$$

$$\left|\overline{V}_n\right| = \frac{\rho_L |u_L| + \rho_R |u_R|}{\rho_L + \rho_R} \tag{4.90}$$

$$g = -\max\left[\min\left(M_L, 0\right), -1\right] \cdot \min\left[\max\left(M_R, 0\right), 1\right] \in [0, 1] \tag{4.91}$$

where p_G is the global pressure ($p_G = p + B^2/2$), and

$$\chi = \left(1 - \widehat{M}\right)^2 \tag{4.92}$$

$$\widehat{M} = \min\left(1.0, \frac{1}{\overline{c}}\sqrt{\frac{\boldsymbol{u}_L{}^2 + \boldsymbol{u}_R{}^2}{2}}\right) \tag{4.93}$$

$$M_L = \frac{u_L}{\overline{c}}, M_R = \frac{u_R}{\overline{c}} \tag{4.94}$$

$$\overline{c} = \frac{c_{f,L} + c_{f,R}}{2} \tag{4.95}$$

where c is the fast magnetosonic speed in MHD,

$$c^2{}_{f,L/R} = \frac{1}{2}\left\{a^2_{L/R} + \frac{\mathbf{B}^2_{L/R}}{\rho_{L/R}} + \sqrt{\left(a^2_{L/R} + \frac{\mathbf{B}^2_{L/R}}{\rho_{L/R}}\right) - 4a^2_{L/R} + \frac{B^2_{x,L/R}}{\rho_{L/R}}}\right\} \tag{4.96}$$

and $a_{L/R}$ is the gas speed of sound, $a^2_{L/R} = \frac{\gamma p_{L/R}}{\rho_{L/R}}$.

Then, the pressure flux is

$$\begin{aligned}\left(p_{1/2}\right)_{SLAU2} = & \frac{p_{G,L} + p_{G,R}}{2} + \frac{\mathrm{P}^+ - \mathrm{P}^-}{2}\left(p_{G,L} - p_{G,R}\right) + \sqrt{\frac{\mathbf{u}_L{}^2 + \mathbf{u}_R{}^2}{2}} \\ & \cdot \left(\mathrm{P}^+ + \mathrm{P}^- - 1\right)\overline{\rho c}\end{aligned} \tag{4.97}$$

$$\overline{\rho} = \frac{\rho_L + \rho_R}{2} \tag{4.98}$$

for the gas dynamics part (first to fifth lines of Eq. (4.80)). On the other hand, the magnetic part, i.e., the sixth to eighth lines, are solved in the simple HLL manner:

$$\mathbf{F}_{SLAU2(Maxwell)} = \mathbf{F}_{HLL(Maxwell)} = \frac{S_R\mathbf{F}_L - S_L\mathbf{F}_R + S_L S_R\left(\mathbf{Q}_R - \mathbf{Q}_L\right)}{S_R - S_L} \tag{4.99}$$

$$\begin{aligned}S_R = & \max\left(u_L, u_R\right) + \max\left(c_{f,L}, c_{f,R}\right), S_L \\ = & \min\left(u_L, u_R\right) - \max\left(c_{f,L}, c_{f,R}\right)\end{aligned} \tag{4.100}$$

where $S_{L/R}$ are "signal" speeds traveling in the left and right directions, respectively. The key idea is the elimination of the dissipation term from the magnetic part

[105]. In addition, Eq. (4.100) uses only local velocities and the fast speeds for simplicity.

Furthermore, to take Alfvén waves into account and enhance the stability at strong shocks, we introduced the following Alfvén speed:

$$\begin{aligned} S_{A,R} &= \max\left(u_R + c_{A,R}, 0\right), \\ S_{A,L} &= \min\left(u_L - c_{A,L}, 0\right) \end{aligned} \tag{4.101}$$

and a strong shock detector using the pressure function borrowed from the AUSMPW+ flux function (but with the c_A weight included) [41, 107]:

$$w = \min\left(\frac{p_{G,L}}{p_{G,R}}, \frac{p_{G,R}}{p_{G,L}}, \frac{c_{A,L}^2}{c_{A,R}^2}, \frac{c_{A,R}^2}{c_{A,L}^2}\right)^3 \tag{4.102}$$

where

$$c_{A,L/R}^2 = \frac{\mathbf{B}_{L/R}^2}{\rho_{L/R}} \tag{4.103}$$

Then, the following new signal speeds are employed that consider both the fast speed and Alfvén speeds:

$$\begin{aligned} S_{R,new} &= \max\left((1-w)S_R + wS_{A,R}, 0\right), \\ S_{L,new} &= \min\left((1-w)S_L + wS_{A,L}, 0\right) \end{aligned} \tag{4.104}$$

which will be substituted for Eq. (4.99). This version will be simply called “SLAU2” in this chapter.

4.3.3.2 Other Parts of Numerical Methods for MHD

We employed the CANS+ code for the MHD tests. The spatial accuracy is five by MP5 (5th-order Monotonicity-Preserving scheme) [76]. A temporal order of accuracy of three was obtained by using an explicit TVD-RK (Total-Variation-Diminishing Runge-Kutta) method [45]. A divergence-free treatment of the magnetic field is realized by hyperbolic divergence cleaning [80]. These detailed descriptions can be found in the original CANS+ paper [102].

4.3.4 Numerical Tests for MHD

Selected test problems are shown below: the 1D shock tube problem by Brio–Wu and the 2D shock and vortex problem by Orzag-Tang.

4.3.4.1 Brio–Wu Shock Tube

This is a widely used MHD shock tube problem that was introduced by Brio and Wu [87].

- $x \leq 0 : (\rho, u, v, w, p, B_y, B_z)_L = (1, 0, 0, 0, 1, \sqrt{4\pi}, 0)$
- $x > 0 : (\rho, u, v, w, p, B_y, B_z)_R = (0.125, 0, 0, 0, 0.1, -\sqrt{4\pi}, 0)$

  with $B_x = 0.75\sqrt{4\pi}$, $\gamma = 2.0$. Computations are conducted with CFL $= 0.3$ to a final time of $t = 0.1$. The computational domain of a unit length $[-0.5, 0.5]$ is even divided by 512 cells. A reference solution by HLL flux for 4000 cells is taken from [105].

The density profile of SLAU2 solution is shown in Fig. 4.23. This successfully reproduced a left-running fast rarefaction wave, a slow compound wave, a contact discontinuity, a slow shock, and a fast rarefaction wave, as in [78], for instance.

4.3.4.2 Orszag–Tang Vortex

This is a standard 2D MHD problem [129] conducted in many computational MHD papers [78, 103, 106–108]. The following initial condition triggers a complicated MHD flow field involving several shock interactions:

$$(\rho, u, v, w, p, B_x, B_y, B_z) = \left(\gamma^2, -\sin(y), \sin(x), 0, \gamma, -\sin(y), \sin(2x), 0\right)$$

with $\gamma = 5/3$. The uniform 100 × 100 cells cover $[0, 2\pi] \times [2\pi]$. The periodic condition is applied to all the four boundaries. The computations are conducted until $t = \pi$ (CFL $= 0.3$).

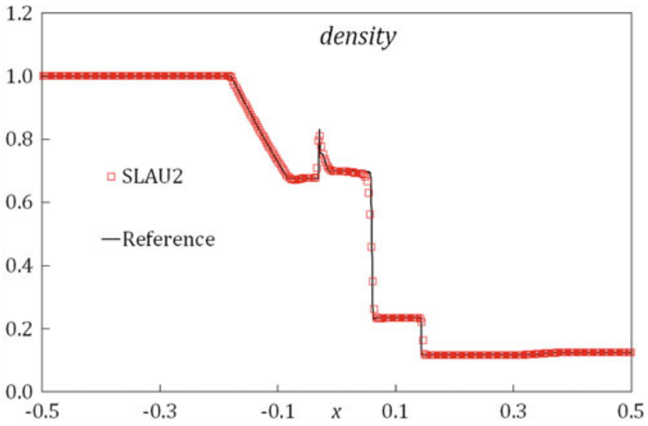

Fig. 4.23 Brio–Wu shock tube problem solution by SLAU2

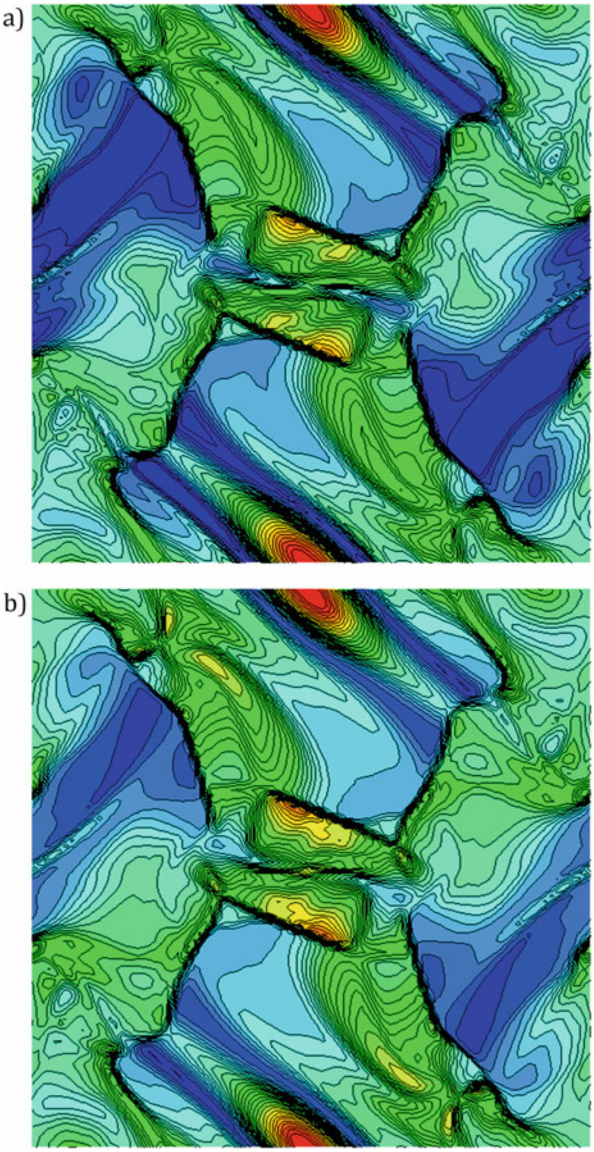

Fig. 4.24 Orszag–Tang vortex problem: (**a**) density, (**b**) pressure

In Fig. 4.24, the density and pressure contours are displayed. Even though the present computational grid is relatively coarse, the solution overall looks similar to the ones reported in the literature [78, 103, 106–108], capturing important physics such as shock interactions. Furthermore, even though SLAU2 is a 3-wave solver, its solution is almost the same as that of HLLD (5-wave solver). Therefore, it has been demonstrated that *SLAU2 successfully handled this 2D MHD problem involving complex shock interactions as well as HLLD did*.

In summary, SLAU2 produced reliable results without showing anomalies, severe oscillations, or losses of resolutions in 1D and 2D MHD. The SLAU2 solutions demonstrated qualities comparable to the HLLD counterparts, whereas HLL smeared out density discontinuities and vorticities [112]. We hope that SLAU2 will be incorporated into MHD codes (e.g., [103, 130, 131]), and will contribute to the further progress of astrophysics and other related research areas.

4.3.5 MHD Summary

The SLAU2 numerical flux function, one of the AUSM-type methods (3-wave solver), originally developed and widely used in gas dynamics, has been applied to 1D and 2D magnetohydrodynamics (MHD) simulations.

- For benchmark tests, detailed and important flow physics such as multidimensional shock/shock interactions have been successfully reproduced by SLAU2.
- Nevertheless, its solution qualities are almost equal to those of HLLD, as opposed to the very diffused HLL solutions.

Let us now review our very recent progress. After further surveys of the MHD version of SLAU2, it was found to be oscillatory in the limited case of low-speed MHD [132]. A remedy was suggested by Mamashita [132], who suppressed the wiggles by borrowing the WS (Wiggle-Sensing)-SLAU's sensor [133], and by Minoshima et al. [134], who interestingly combined the concepts of AUSM and HLLD in a sophisticated manner. Interested readers are encouraged to read the original papers.

References

1. Saurel, R., Abgrall, R.: A multiphase Godunov method for compressible multifluid and multiphase flows. J. Comput. Phys. **150**, 425–467 (1999)
2. Kunz, R.F., Boger, D.A., Stinebring, D.R., Chyczewski, T.S., Lindau, J.W., Gibeling, H.J., Venkateswaran, S., Govindan, T.: A preconditioned Navier–Stokes method for two-phase flows with application to cavitation prediction. Comput. Fluids. **29**(8), 849–875 (2000). https://doi.org/10.1016/S0045-7930(99)00039-0
3. Lempke, M., Gerlinger, R., Seidl, M.J., Aigner, M.: Unsteady high-order simulation of a liquid oxygen/gaseous hydrogen rocket combustor. J. Propul. Power. **31**(6), 1715–1726 (2015). https://doi.org/10.2514/1.B35726
4. Tsutsumi, S., Takaki, R., Hara, T., Ueda, H., Nagata, H.: Numerical analysis of ignition overpressure effect on H-IIB launch vehicle. J. Spacecr. Rocket. **51**(3), 893–899 (2014). https://doi.org/10.2514/1.A32700
5. Kimura, T., Hashimoto, T., Sato, M., Takada, S., Moriya, S., Yagishita, T., Naruo, Y., Ogawa, H., Ito, T., Obase, K., Ohmura, H.: Reusable rocket engine: firing tests and lifetime analysis of

combustion chamber. J. Propul. Power. **32**(5), 1087–1094 (2016). https://doi.org/10.2514/1.B35973

6. Osher, S., Sethian, J.A.: Fronts propagating with curvature dependent speed: algorithms based on Hamilton-Jacobi formulations. J. Comput. Phys. **79**, 12–49 (1988)
7. Sussman, M., Smereka, P., Osher, S.: A level set approach for computing solutions to incompressible two-phase flow. J. Comput. Phys. **114**, 146–159 (1994)
8. Kim, H., Liou, M.-S.: Accurate adaptive level set method and sharpening technique for three dimensional deforming interfaces. Comput. Fluids. **44**, 111–129 (2011)
9. Tryggvason, G., Bunner, B., Esmaeeli, A., Juric, D., Al-Rawahi, N., Tauber, W., Han, J., Nas, S., Jan, Y.-J.: A front-tracking method for the computations of multiphase flow. J. Comput. Phys. **169**, 708–759 (2001)
10. Terashima, H., Tryggvason, G.: A front-tracking/ghost-fluid method for fluid interfaces in compressible flows. J. Comput. Phys. **228**, 4012–4037 (2009)
11. Hirt, C.W., Nichols, B.D.: Volume of fluid (VOF) method for the dynamics of free boundaries. J. Comput. Phys. **39**(1), 201–225 (1981). https://doi.org/10.1016/0021-9991(81)90145-5
12. Ii, S., Sugiyama, K., Takeuchi, S., Takagi, S., Matsumoto, Y., Xiao, F.: An Interface capturing method with a continuous function: the THINC method with multi-dimensional reconstruction. J. Comput. Phys. **231**, 2328–2358 (2012)
13. Goncalves, E., Patella, R.F.: Numerical simulation of cavitating flows with homogeneous models. Comput. Fluids. **38**, 1682–1696 (2009)
14. Edwards, J.R., Franklin, R.K., Liou, M.-S.: Low-diffusion flux-splitting methods for real fluid flows with phase transitions. AIAA J. **38**, 1624–1633 (2000)
15. Ihm, S.-W., Kim, C.: Computations of homogeneous-equilibrium two-phase flows with accurate and efficient shock-stable schemes. AIAA J. **46**, 3012–3037 (2008)
16. Saurel, R., Lemetayer, O.: A multiphase model for compressible flows with interfaces, shocks, detonation waves and cavitation. J. Fluid Mech. **431**, 239–271 (2001)
17. Toumi, I.: An upwind numerical method for two-fluid two-phase flow methods. Nucl. Sci. Eng. **123**, 147–168 (1996)
18. Chang, C.-H., Sushchikh, S., Nguyen, L., Liou, M.-S., Theofanous, T.: Hyperbolicity, discontinuities, and numerics of the two-fluid model. In: 5th Joint ASME/JSME Fluids Engineering Summer Conference, American Society of Mechanical Engineers, Fluid Engineering Div., Paper FEDSM2007-37338 (2007)
19. Shukla, R.K., Pantano, C., Freund, J.B.: An Interface capturing method for the simulation of multi-phase compressible flows. J. Comput. Phys. **229**, 7411–7439 (2010)
20. So, K.K., Hu, X.Y., Adams, N.A.: Anti-diffusion Interface sharpening technique for two-phase compressible flow simulations. J. Comput. Phys. **231**, 4304–4323 (2012)
21. Kiris, C.C., Kwak, D., Chan, W., Housman, J.A.: High-fidelity simulations of unsteady flow through turbopumps and flowliners. Comput. Fluids. **37**, 536–546 (2008)
22. Kitamura, K., Liou, M.-S., Chang, C.-H.: Extension and comparative study of AUSM-family schemes for compressible multiphase flow simulations. Commun. Comput. Phys. **16**(3), 632–674 (2014). https://doi.org/10.4208/cicp.020813.190214a
23. Chang, C.-H., Liou, M.-S.: A robust and accurate approach to computing compressible multiphase flow: stratified flow model and AUSM+-up scheme. J. Comput. Phys. **225**, 840–873 (2007)
24. Nonomura, T., Kitamura, K., Fujii, K.: A simple interface sharpening technique with a hyperbolic tangent function applied to compressible two-fluid modeling. J. Comput. Phys. **258**, 95–117 (2014). https://doi.org/10.1016/j.jcp.2013.10.021
25. Haas, J., Sturtevant, B.: Interaction of weak shock waves with cylindrical and spherical gas inhomogeneities. J. Fluid Mech. **181**, 41–76 (1987)
26. Quirk, J., Karni, S.: On the dynamics of a shock-bubble interaction. J. Fluid Mech. **318**, 129–164 (1996)

27. Shyue, K.-M.: A wave-propagation based volume tracking method for compressible multicomponent flow in two space dimensions. J. Comput. Phys. **215**(1), 219–244 (2006)
28. Ransom, V.H.: Numerical benchmark tests. In: G. F. Hewitt, J. M. Delhay, and N. Zuber, (eds.) Multiphase Science and Technology. Hemisphere, Washington, DC, pp. 465–467 (1987)
29. Stewart, H.B., Wendroff, B.: Two-phase flow: models and methods. J. Comput. Phys. **56**, 363–409 (1984)
30. Liou, M.-S., Chang, C.-H., Nguyen, L., Theofanous, T.G.: How to solve compressible multifluid equations: a simple, robust, and accurate method. AIAA J. **46**, 2345–2356 (2008)
31. van Leer, B.: Towards the ultimate conservative difference scheme. V. A second-order sequel to Godunov's method. J. Comput. Phys. **32**, 101–136 (1979)
32. van Albada, G.D., van Leer, B. and Roberts, Jr., W.W., A comparative study of computational methods in cosmic gas dynamics. *Astron. Astrophys.*, Vol. 108, pp. 76–84, 1982.
33. Stuhmiller, J.: The influence of interfacial pressure forces on the character of two-phase flow model equations. Int. J. Multiphase Flow. **3**, 551–560 (1977)
34. Harlow, F., Amsden, A.: Fluid Dynamics. Technical Report LA-4700Los Alamos National Laboratory (1971)
35. Jolgam, S., Ballil, A., Nowakowski, A., Nicolleau, F.: On equations of state for simulations of multiphase flows. In: Proc. World Congress on Engineering 2012, Vol. *III,* WCE, July 4–6, 2012
36. Liou, M.-S.: A sequel to AUSM, part II: AUSM+-up for all speeds. J. Comput. Phys. **214**, 137–170 (2006)
37. Shima, E., Kitamura, K.: Parameter-free simple Low-dissipation AUSM-family scheme for all speeds. AIAA J. **49**(8), 1693–1709 (2011). https://doi.org/10.2514/1.55308
38. Hosangadi, A., Sachdev, J., Sankaran, V.: Improved flux formulations for unsteady low mach number flows. In: ICCFD7-2202, Seventh International Conference on Computational Fluid Dynamics (ICCFD7), Big Island, Hawaii, July 9–13 (2012)
39. Kitamura, K., Shima, E., Fujimoto, K., Wang, Z.J.: Performance of Low-dissipation Euler fluxes and preconditioned LU-SGS at Low speeds. Commun. Comput. Phys. **10**(1), 90–119
40. Kitamura, K., Shima, E.: Towards shock-stable and accurate hypersonic heating computations: a new pressure flux for AUSM-family schemes. J. Comput. Phys. **245**, 62–83 (2013). https://doi.org/10.1016/j.jcp.2013.02.046
41. Kim, S.S., Kim, C., Rho, O.H., Hong, S.K.: Methods for the accurate computations of hypersonic flows. I. AUSMPW+ Scheme. J. Comput. Phys. **174**, 38–80 (2001)
42. Godunov, S.K.: A finite difference method for the numerical computation of discontinuous solutions of the equations of fluid dynamics. Matematicheskii Sbornik/Izdavaemyi Moskovskim Matematicheskim Obshchestvom. **47**(3), 271–306 (1959)
43. Toro, E.F.: Riemann Solvers and Numerical Methods for Fluid Dynamics: A Practical Introduction3rd edn, Springer-Verlag, Berlin Heidelberg (2009). ISBN 978-3540252023
44. Kitamura, K., Nonomura, T.: Simple and robust HLLC extensions of two-fluid AUSM for multiphase flow computations. Comput. Fluids. **100**, 321–335 (2014). https://doi.org/10.1016/j.compfluid.2014.05.019
45. Gottlieb, S., Shu, C.-W.: Total variation diminishing Runge-Kutta schemes. Math. Comput. **67**, 73–85 (1998)
46. Niu, Y.-Y., Lin, Y.-C., Chang, C.-H.: A further work on multi-phase two-fluid approach for compressible multi-phase flows. Int. J. Numer. Methods Fluids. **58**, 879–896 (2008)
47. Paillère, H., Corre, C., Cascales, J.R.G.: On the extension of the AUSM+ scheme to compressible two-fluid models. Comput. Fluids. **32**, 891–916 (2003)
48. Terashima, H., Kawai, S., Yamanishi, N.: High-resolution numerical method for supercritical flows with large density variations. AIAA J. **49**(12), 2658–2672 (2011)
49. Pandare, A.K., Luo, H.: A robust and efficient finite volume method for compressible inviscid and viscous two-phase flows. J. Comput. Phys. **371**, 67–91 (2018). https://doi.org/10.1016/j.jcp.2018.05.018

50. Aono, J., Kitamura, K.: Numerical investigation of AUSM-family schemes dissipation for compressible multiphase flow simulations. In: OR-09-0367, 32nd International Symposium on Shock Waves (ISSW32)National University of Singapore, Singapore (2019)
51. Kitamura, K., Shima, E.: AUSM-like expression of HLLC and its all-speed extension. Int. J. Numer. Methods Fluids. **92**, 246–265 (2020). https://doi.org/10.1002/fld.4782
52. Mayer, W.O.H., Smith, J.J.: Fundamentals of supercritical mixing and combustion of cryogenic propellants. In: Yang, V., Habiballah, M., Hulka, J., Popp, M. (eds.) Liquid Rocket Thrust Chambers: Aspects of Modeling, Analysis, and Design, Progress in Astronautics and Aeronautics, vol. 200, American Institute of Aeronautics and Astronautics, Inc., Reston, VA (2004)
53. Teramoto, S., Tani, H.: Conservative higher-order simulation of cryogenic transcritical flow. 26th Computational Fluid Dynamics Symposium, C01-2 (2012) (in Japanese).
54. Terashima, H., Koshi, M.: Approach for simulating gas–liquid-like flows under supercritical pressures using a high-order central differencing scheme. J. Comput. Phys. **231**(20), 6907–6923 (2012)
55. Fedkiw, R., Liu, X., Osher, S.: A general technique for eliminating spurious oscillations in conservative schemes for multiphase and multispecies Euler equations. Int. J. Nonlin. Sci. Num. Simulation. **3**(2), 99–106 (2002)
56. Matheis, J., Müller, H., Pfitzner, M., Hickel, S.: Large Eddy simulation of cryogenic coaxial Ln2/Gh2 injection under supercritical pressures. In: International Symposium on Turbulence and Shear Flow Phenomena (TSFP-9), pp. 8C–5C, Melbourne, Australia (2015)
57. Cockburn, B., Shu, C.W.: The Runge-Kutta discontinuous Galerkin method for conservation laws V. Multidimensional systems. J. Comput. Phys. **141**, 199–224 (1998)
58. Soave, G.: Equilibrium constants from a modified Redlich–Kwong equation of state. Chem. Eng. Sci. **27**(6), 1197–1203 (1972)
59. Gnoffo, P., Buck, G., Moss, J., Nielsen, E., Berger, K., Jones, W.T., Rubavsky, R.: Aerothermodynamic analyses of towed Ballutes. In: 9th AIAA/ASME Joint Thermodynamics and Heat Transfer Conference, AIAA Paper 2006-3771, San Francisco, CA (2006)
60. Catalano, P., Marini, M., Nicoli, A., Pizzicaroli, A.: CFD contribution to the aerodynamic data set of the Vega launcher. J. Spacecraft Rockets. **44**(1), 42–51 (2007)
61. Hashimoto, A., Murakami, K., Aoyama, T., Yamamoto, K., Murayama, M., Lahur, P.R.: Drag prediction on NASA common research model using automatic hexahedra grid-generation method. J. Aircraft. **51**(4), 1172–1182 (2014)
62. Kitamura, K., Nonaka, S., Kuzuu, K., Aono, J., Fujimoto, K., Shima, E.: Numerical and experimental investigations of epsilon launch vehicle aerodynamics at Mach 1.5. J. Spacecraft Rockets. **50**(4), 896–916 (2013)
63. Zong, N., Yang, V.: Cryogenic fluid jets and mixing layers in transcritical and supercritical environments. Combust. Sci. Technol. **178**(1), 193–227 (2006)
64. Hosangadi, A., Lee, C., Kannepalli, C., Arunajatesan, S.: Three-dimensional hybrid RANS/LES simulations of a supercritical liquid nitrogen jet. In: AIAA Paper 2008-5227 (2008)
65. Chung, T., Ajlan, M., Lee, L., Starling, K.: Generalized multiparameter correlation for nonpolar and polar fluid transport properties. Ind. Eng. Chem. Res. **27**(4), 671–679 (1988)
66. Kitamura, K., Shima, E.: Pressure-equation-based SLAU2 for oscillation-free, supercritical flow simulations. Comput. Fluids. **163**, 86–96 (2018). https://doi.org/10.1016/j.compfluid.2018.01.001
67. Arina, R.: Numerical simulation of near-critical fluids. Appl. Numer. Math. **51**(4), 409–426 (2004)
68. Roe, P.L.: Characteristic-based schemes for the Euler equations. Annu. Rev. Fluid Mech. **18**, 337–365 (1986)
69. Lemmon, E., Huber, M., McLinden, M.: NIST Standard Reference, Database 23: Reference Fluid Thermodynamic and Transport Properties-REFPROP, Version 8.0National Institute of Standards and Technology, Standard Reference Data Program, Gaithersburg, MD (2007)

70. Esquivel, A., Raga, A.C., Cantó, J., Rodríguez-González, A., López-Cámara, D., Velázquez, P.F., De Colle, F.: Model of Mira's cometary head/tail entering the local bubble. Astrophys. J. **725**, 1466–1475 (2010)
71. Ohnishi, N., Kotake, K., Yamada, S.: Numerical analysis on standing accretion shock instability with neutrino heating in the supernova cores. Astrophys J. **667**(1), 375–381 (2007)
72. Hanawa, T., Mikami, H., Matsumoto, T.: Improving shock irregularities based on the characteristics of the MHD equations. J. Comput. Phys. **227**, 7952–7976 (2008)
73. Poggie, J., Gaitonde, D.V.: Magnetic control of flow past a blunt body: numerical validation and exploration. Phys. Fluids. **14**(1720), 1720–1731 (2002)
74. ITER Physics Expert Groups on Confinement and Transport and Confinement Modelling and Database: ITER physics basis. Nucl. Fusion. **39**, 2137–2638 (1999)
75. Loarte, A., Liu, F., Huijsmans, G.T.A., Kukushkin, A.S., Pitts, R.A.: MHD stability of the ITER pedestal and SOL plasma and its influence on the heat flux width. J. Nucl. Mater. **463**, 401–405 (2015)
76. Suresh, A., Huynh, H.T.: Accurate monotonicity-preserving schemes with Runge–Kutta time stepping. J. Comput. Phys. **136**, 83–99 (1997)
77. Roe, P.L.: Approximate Riemann solvers, parameter vectors, and difference schemes. J. Comput. Phys. **43**, 357–372 (1981)
78. Miyoshi, T., Kusano, K.: A multi-state HLL approximate Riemann solver for ideal magnetohydrodynamics. J. Comput. Phys. **208**, 315–344 (2005)
79. Harten, A., Lax, P.D., van Leer, B.: On upstream differencing and Godunov-type schemes for hyperbolic conservation laws. SIAM Rev. **25**(1), 35–61 (1983)
80. Dedner, A., Kemm, F., Kroner, D., Munz, C.D., Schnitzer, T., Wesenberg, M.: Hyperbolic divergence cleaning for the MHD equations. J. Comput. Phys. **175**, 645–673 (2002)
81. Balsara, D.S.: Second-order-accurate schemes for magnetohydrodynamics with divergence-free reconstruction. Astrophys. J. Suppl. Ser. **151**, 149–184 (2004)
82. Balsara, D.S., Spicer, D.S.: A staggered mesh algorithm using high order Godunov fluxes to ensure solenoidal magnetic fields in magnetohydrodynamics simulation. J. Comput. Phys. **149**, 270–292 (1999)
83. Tóth, G.: The $\nabla \cdot B = 0$ constraint in shock-capturing magnetohydrodynamics codes. J. Comput. Phys. **161**, 605–652 (2000)
84. Powell, K.G., Roe, P.L., Linde, T., Gombosi, T.I., De Zeeuw, D.L.: A solution-adaptive upwind scheme for ideal magnetohydrodynamics. J. Comput. Phys. **154**, 284–309 (1999)
85. Dumbser, M., Moschetta, J.M., Gressier, J.: A matrix stability analysis of the carbuncle phenomenon. J. Comput. Phys. **197**(2), 647–670 (2004)
86. Quirk, J.J.: A contribution to the great Riemann solver debate. Int. J. Numer. Methods Fluids. **18**(6), 555–574 (1994)
87. Brio, M., Wu, C.C.: An upwind differencing scheme for the equations of ideal magnetohydrodynamics. J. Comput. Phys. **75**, 400–422 (1988)
88. Ryu, D.S., Jones, T.W.: Numerical magnetohydrodynamics in astrophysics: algorithm and test for one-dimensional flow. Astrophys. J. **442**, 228–258 (1995)
89. Roe, P.L., Balsara, D.S.: Notes on the Eigensystem of magnetohydrodynamics. SIAM J. Appl. Math. **56**, 57–67 (1996)
90. Cargo, P., Gallice, G.: Roe matrices for ideal MHD and systematic construction of Roe matrices for systems of conservation laws. J. Comput. Phys. **136**, 446–466 (1997)
91. Balsara, D.S.: Linearized formulation of the Riemann problem for adiabatic and isothermal magnetohydrodynamics. Ap. J. Suppl. **116**, 119–131 (1998)
92. Dumbser, M., Balsara, D.S.: A new efficient formulation of the HLLEM Riemann solver for general conservative and non-conservative hyperbolic systems. J. Comput. Phys. **304**, 275–319 (2016)
93. Liou, M.S.: Mass flux schemes and connection to shock instability. J. Comput. Phys. **160**, 623–648 (2000)
94. Peery, K.M., Imlay, S.T.: Blunt-body flow simulations. In: AIAA Paper 88-2904 (1988)

95. Pandolfi, M., D’Ambrosio, D.: Numerical instabilities in upwind methods: analysis and cures for the carbuncle phenomenon. J. Comput. Phys. **166**(2), 271–301 (2001)
96. Kitamura, K., Roe, P., Ismail, F.: Evaluation of Euler fluxes for hypersonic flow computations. AIAA J. **47**(1), 44–53 (2009)
97. Kitamura, K., Shima, E., Nakamura, Y., Roe, P.: Evaluation of Euler fluxes for hypersonic heating computations. AIAA J. **48**(4), 763–776 (2010)
98. Kitamura, K., Shima, E., Roe, P.: Carbuncle phenomena and other shock anomalies in three dimensions. AIAA J. **50**(12), 2655–2669 (2012)
99. Chauvat, Y., Moschetta, J.M., Gressier, J.: Shock wave numerical structure and the carbuncle phenomenon. Int. J. Numer. Methods Fluids. **47**, 903–909 (2005)
100. Barth, T.J.: Some Notes on Shock-Resolving Flux Functions Part 1: Stationary Characteristics. NASA TM-101087 (1989)
101. Roe, P.L.: Fluctuations and signals—a framework for numerical evolution problems. In: Morton, K.W., Baines, M.J. (eds.) Numerical Methods for Fluid Dynamics, pp. 219–257. Academic Press, New York (1982)
102. Matsumoto, Y., Asahina, Y., Kudoh, Y., Kawashima, T., Matsumoto, J., Takahashi, H.R., Minoshima, T., Zenitani, S., Miyoshi, T., Matsumoto, R.: Magnetohydrodynamic simulation code CANS+: assessments and applications. Publ. Astron. Soc. Jpn. **71**(4), 83 (2019). https://doi.org/10.1093/pasj/psz06
103. Stone, J.M., Gardiner, T.A., Teuben, P., Hawley, J.F., Simon, J.B.: ATHENA: a new code for astrophysical MHD. Astrophys. J. Suppl. Ser. **178**(1), 137–177 (2008)
104. Minoshima, T., Miyoshi, T., Matsumoto, Y.: A high-order weighted finite difference scheme with a multi-state approximate Riemann solver for divergence-free magnetohydrodynamic simulations. Ap. J. Suppl. **242**(2) (2019)
105. Kitamura, K., Balsara, D.S.: Hybridized SLAU2–HLLI and hybridized AUSMPW+–HLLI Riemann solvers for accurate, robust, and efficient magnetohydrodynamics (MHD) simulations, part I: one-dimensional MHD. Shock Waves. **29**, 611–627 (2019)
106. Xisto, C.M., Páscoal, J.C., Oliveira, P.J.: A pressure-based high resolution numerical method for resistive MHD. J. Comput. Phys. **275**, 323–345 (2014)
107. Han, S.H., Lee, J.I., Kim, K.H.: Accurate and robust pressure weight advection upstream splitting method for magnetohydrodynamics equations. AIAA J. **47**(4), 970–981 (2009)
108. Shen, Y., Zha, G., Huerta, M.A.: E-CUSP scheme for the equations of ideal magnetohydrodynamics with high order WENO scheme. J. Comput. Phys. **231**, 6233–6247 (2012)
109. Li, S.: An HLLC Riemann solver for magnetohydrodynamics. J. Comput. Phys. **203**, 344–357 (2005)
110. Gurski, K.F.: An HLLC-type approximate Riemann solver for ideal magnetohydrodynamics. SIAM J. Sci. Comput. **25**(6), 2165–2187 (2004)
111. van Leer, B.: Flux-vector splitting for the Euler equations. Lect. Notes Phys. **170**, 507–512 (1982)
112. Kitamura, K., Mamashita, T., Ryu, D.: SLAU2 applied to two-dimensional, ideal magnetohydrodynamics simulations. Comput. Fluids. **209**, 104635 (2020)
113. Zha, G.-C., Shen, Y., Wang, B.: An improved low diffusion E-CUSP upwind scheme. Comput. Fluids. **48**, 214–220 (2011)
114. Kitamura, K.: Assessment of SLAU2 and other flux functions with slope limiters in hypersonic shock-interaction heating. Comput. Fluids. **129**, 134–145 (2016)
115. Weiss, J.M., Smith, W.A.: Preconditioning applied to variable and constant density flows. AIAA J. **33**(11), 2050–2057 (1995)
116. Liu, Y., Vinokur, M.: Upwind algorithms for general thermo-chemical nonequilibrium flows. In: AIAA Paper 89-0201 (1989)
117. Toro, E.F., Spruce, M., Speares, W.: Restoration of the contact surface in the HLL Riemann solver. Shock Waves. **4**, 25–34 (1994)
118. Rusanov, V.V.: Calculation of interaction of non-steady shock waves with obstacles. J. Comput. Math. Phys. USSR. **1**, 267–279 (1961)

119. Janhunen, P.: A positive conservative method for magnetohydrodynamics based HLL and Roe methods. J. Comput. Phys. **160**, 649–661 (2000)
120. Sanders, R., Morano, E., Druguetz, M.C.: Multidimensional dissipation for upwind schemes: stability and applications to gas dynamics. J. Comput. Phys. **145**(2), 511–537 (1998)
121. Shima, E., Kitamura, K.: Multidimensional numerical noise from captured shockwave and its cure. AIAA J. **51**, 992–998 (2013)
122. Hashimoto, A., Murakami, K., Aoyama, T., Ishiko, K., Hishida, M., Sakashita, M., Lahur, P.: Toward the fastest unstructured CFD code 'FaSTAR'. In: AIAA-2012-1075 (2012)
123. Kitamura, K., Fujimoto, K., Shima, E., Kuzuu, K., Wang, Z.J.: Validation of an arbitrary unstructured CFD code for aerodynamic analyses. Trans. Jpn. Soc. Aeronaut. Space Sci. **53**, 311–319 (2011)
124. Molina, E., Zhou, B.Y., Alonso, J.J., Righi, M., Silva, R.G.: Flow and noise predictions around tandem cylinders using DDES approach with SU2. AIAA 2019-0326, AIAA Scitech 2019 Forum, 7–11 January 2019, San Diego, CA.
125. Brown, B.P., Vasil, G.M., Zweibel, E.G.: Energy conservation and gravity waves in sound-proof treatments of stellar interiors. Part I. Anelastic approximations. Astrophys. J. **756**(2), 20 pp. (2012)
126. MacGregor, K.B., Rogers, T.M.: Reflection and ducting of gravity waves inside the sun. Sol. Phys. **270**(2), 417–436 (2011)
127. Brun, A.S., Miesch, M.S., Toomre, J.: Modeling the dynamical coupling of solar convection with the radiative interior. Astrophys J. **742**(2), 20 pp. (2011)
128. Stix, M.: The Sun: An Introduction, 2. Astronomy and Astrophysics Library. Springer Berlin (2004). ISBN: 3-540-20741-4
129. Orszag, A., Tang, C.M.: Small-scale structure of two-dimensional magnetohydrodynamic turbulence. J. Fluid Mech. **90**, 129–143 (1979)
130. Tzeferacos, P., Fatenejad, M., Flocke, N., Graziani, C., Gregori, G., Lamb, D.Q., Lee, D., Meinecke, J., Scopatz, A., Weide, K.: FLASH MHD simulations of experiments that study shock-generated magnetic fields. High Ener. Density Phys. **17**, 24–31 (2015)
131. Mignone, A., Bodo, G., Massaglia, S., Matsakos, T., Tesileanu, O., Zanni, C., Ferrari, A.: PLUTO: a Numerical Code for Computational Astrophysics arXiv:astro-ph/0701854. (2007) Accessed 19 Sept 2017
132. Mamashita, T.: Application and verifications of all speed scheme SLAU2 for magnetohydrodynamics (MHD) simulations. Graduation Thesis. Yokohama National University (2020) (in Japanese)
133. Shima, E.: On the improvement of the all-speed flux scheme for very low mach number flows. In: AIAA Paper 2013-2696, 21st AIAA Computational Fluid Dynamics Conference, June 24–27, 2012, San Diego, CA
134. Minoshima, T., Kitamura, K., Miyoshi, T.: A multistate low-dissipation advection upstream splitting method for ideal magnetohydrodynamics. Ap. J. Suppl. 248(12): 21 pp. (2020)

Chapter 5
Reconstruction and Slope Limiters

Abstract A spatially second-order or higher method is typically employed in practical simulations of FVM. To achieve at least second-order accuracy, the cell-internal distribution of variables should be reconstructed. There are various reconstruction methods such as MUSCL, (Weighted) Least Squares, Green-Gauss, and hybridizations of Green-Gauss/Least Squares, … but which is the best way? The answer depends on the employed numerical setup such as cell geometries and data structure (e.g., whether a structured or unstructured grid is used). In addition to this, a slope limiter such as the minmod limiter or Venkatakrishnan limiter is required to prevent spurious oscillations at discontinuities. This chapter will summarize those reconstruction methods and slope limiters, as well as our recent proposals, including the second limiter and the post limiter.

Keywords MUSCL · Least squares · Green-gauss · GLSQ · Slope limiter (limiting function) · Minmod · Van Albada · Venkatakrishnan · Second limiter · Post limiter

5.1 Monotone Upstream-Centered Schemes for Conservation Laws (MUSCL), (Weighted) Least-Squares, Green-Gauss (G-G), and Green-Gauss/Least-Squares Methods

The Euler/Navier–Stokes equations are discretized as

$$\frac{V_i}{\Delta t_i}\Delta\mathbf{Q}_i + \boldsymbol{\Gamma}_i^{-1}\sum_j \left(\mathbf{F}_{i,j} - \mathbf{Fv}_{i,j}\right)S_{i,j} = 0 \tag{1.4}$$

as reviewed in Chap. 1. To obtain the inviscid numerical flux **F** at the cell interface, for instance, we use a flux function such as

K. Kitamura, *Advancement of Shock Capturing Computational Fluid Dynamics Methods*, https://doi.org/10.1007/978-981-15-9011-5_5

$$\mathbf{F}_{1/2(Roe)} = \frac{1}{2}(\mathbf{F}_L + \mathbf{F}_R) - \frac{1}{2}\hat{\mathbf{R}}\left|\hat{\boldsymbol{\Lambda}}\right|\hat{\mathbf{L}}\boldsymbol{\Delta}\mathbf{Q} \tag{3.4}$$

where $\mathbf{F}_L$ and $\mathbf{F}_R$ are the physical fluxes of the left and right sides, respectively, and $\boldsymbol{\Delta}\mathbf{Q}$ is the conservative-variable difference between both sides, *all* at the cell interface. These cell-interfacial values can be either cell-center values (= 1st-order in space) or interpolated values using estimated cell-internal distributions (= 2nd-order or higher). These distributions are reconstructed from the cell-center values in various ways, along with slope limiters to prevent spurious oscillations at discontinuities, as described in this chapter.

Now let us turn our attention to a very important aspect of computational grids, i.e., structured and unstructured grids. Most of the numerical flux functions in Chap. 2 were developed based on the 1D assumption. They are easily applied both on structured and unstructured grids, because at the cell interface their normal and tangential directions are defined regardless of the grid/cell geometry or data structure. When it comes to spatial reconstruction including slope limiters, however, care must be taken to distinguish between the structured and unstructured grids.

The reconstruction on structured grids is typically conducted by using the MUSCL approach [1], along *only one index* (e.g., *i, j,* or *k*-index in 3D), as if each (index-) direction is completely independent of the others. In other words, the reconstruction, as well as the slope limiting (e.g., minmod, van Leer, van Albada), is carried out in a 1D manner for every direction. Next, the gradients are evaluated at each *cell interface* (which is exactly where the numerical flux is calculated).

In contrast, the reconstruction on unstructured grids uses *all* the surrounding cell information [2] by using the Green-Gauss (G-G) formula, Least-Square (LSQ), or their variants etc., to obtain the gradients of physical variables at each *cell center*. Thus, these methods are genuinely multidimensional, and therefore, so are the slope limiters (e.g., Barth–Jespersen [3] and Venkatakrishnan [4]). Moreover, they can also be used on structured grids. In this section, these reconstruction methods for structured grids and unstructured grids are briefly reviewed.

5.1.1 MUSCL

The MUSCL (pronounced "muscle") reconstruction [1] is written as follows (without a limiter)

$$q_{i+1/2,L} = q_i + \frac{1+\kappa}{4}\left(q_{i+1} - q_i\right) + \frac{1-\kappa}{4}\left(q_i - q_{i-1}\right) \tag{5.1}$$

$$q_{i+1/2,R} = q_{i+1} - \frac{1-\kappa}{4}\left(q_{i+2} - q_{i+1}\right) - \frac{1+\kappa}{4}\left(q_{i+1} - q_i\right) \tag{5.2}$$

where q is one of primitive variables (of course, a conservative or characteristic variable can be substituted, though), and κ is a parameter. When $\kappa = 1/3$, the variable

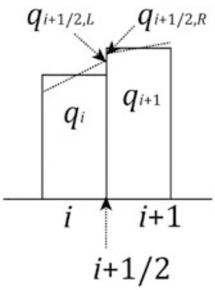

Fig. 5.1 Cell-center values and cell-interfacial values

q is upwind-biased using information from all the three points, $q_{i\text{-}1}$, q_i, and q_{i+1} in Eq. (5.1) (3rd-order in 1D); whereas if $\kappa = -1$, it is fully upwinded (i.e., q_{i+1} is not considered) (2nd-order) [5]. Note that $q_{i+1/2,L}$ is interpolated from the ith cell center, q_i, along with its neighbors q_{i+1} and $q_{i\text{-}1}$, while $q_{i+1/2,R}$ is obtained from q_{i+1} with its neighbors q_{i+2} and q_i. The second and third terms in the R.H.S. will be replaced if a limiter is employed, such as

$$q_{i+1/2,L} = q_i + s \cdot \left[\frac{1 + s\kappa}{4}\left(q_{i+1} - q_i\right) + \frac{1 - s\kappa}{4}\left(q_i - q_{i-1}\right)\right] \tag{5.3}$$

$$q_{i+1/2,R} = q_{i+1} - s \cdot \left[\frac{1 - s\kappa}{4}\left(q_{i+2} - q_{i+1}\right) + \frac{1 + s\kappa}{4}\left(q_{i+1} - q_i\right)\right] \tag{5.4}$$

where

$$s = \frac{2 \cdot \left(q_{i+1} - q_i\right) \cdot \left(q_i - q_{i-1}\right) + \varepsilon}{\left(q_{i+1} - q_i\right)^2 + \left(q_i - q_{i-1}\right)^2 + \varepsilon} \tag{5.5}$$

where ε is a positive small number.

These forms are based on 1D uniform grids, but are extendable to structured grids (Fig. 5.1). Furthermore, they are also extended to unstructured grids, which are called U-MUSCL (Unstructured MUSCL) [6].

5.1.2 *(Weighted) Least Squares (WLSQ)*

On unstructured grids, on the other hand, the expression

$$q_{i,j} = q_i + \phi \nabla q_i \cdot \left(\mathbf{r}_{i,j} - \mathbf{r}_i\right) \tag{5.6}$$

is commonly used (which is also valid on structured grids). Note that Eq. (5.1) is a special case of Eq. (5.6) when ∇q_i is evaluated by $(q_i - q_{i\text{-}1})/\Delta x$, and $(\mathbf{r}_{i,j} - \mathbf{r}_i)$ by $\Delta x/2$, if $\kappa = -1$ and $\phi = 1$. In practice, the gradient ∇q_i is computed by Green-Gauss, Least Squares, or their variants, according to all the surrounding cells (Eq. (5.6) already included the limiter value ϕ).

There are many choices for the reconstruction for arbitrary polyhedra or polygons in unstructured meshes [2, 7–15]. The weighted-least-squares (WLSQ) methods give exact gradients for a linear distribution of the variables. On the other hand, the Green-Gauss (G-G) reconstruction has this property only on symmetric and uniform meshes.

In [16], we proposed a robust and (second-order) accurate hybrid reconstruction method of WLSQ and G-G suitable for, but not limited to, those mixed grids in a unified manner that overcomes the abovementioned difficulties encountered by the existing methods.

5.1.2.1 WLSQ (N)

In WLSQ, the gradient is computed so that the sum of the squared errors shown below is minimized:

$$\prod_i = \sum_j \omega_{i,j} \left(\nabla q_i \cdot \left(\mathbf{r}_j - \mathbf{r}_i \right) - \Delta q_{i,j} \right)^2, \omega_{i,j} > 0 \tag{5.7}$$

where Δ stands for the difference between variables at cells i and j; i.e., $\Delta q_{i,j} = q_j - q_i$.

From the stationary condition, the following linear equation is obtained:

$$\mathbf{M}_i \nabla q_i = \sum_j \omega_{i,j} \Delta q_{i,j} \left(\mathbf{r}_j - \mathbf{r}_i \right) = \sum_j \omega_{i,j} L_{ij} \Delta q_{i,j} \mathbf{r}_{L,j} \tag{5.8}$$

$$\mathbf{M}_i = \begin{pmatrix} I_{XX,i} & I_{XY,i} & I_{ZX,i} \\ I_{XY,i} & I_{YY,i} & I_{YZ,i} \\ I_{ZX,i} & I_{YZ,i} & I_{ZZ,i} \end{pmatrix} \tag{5.9}$$

$$I_{AB,i} = \sum_j \omega_{ij} \Delta A \Delta B \tag{5.10}$$

where $\mathbf{r}_{L,\ j}$ is a unit vector from the cell center to its neighboring cell's center: $\mathbf{r}_{L,\ j} \equiv (\mathbf{r}_j - \mathbf{r}_{ii})/|\mathbf{r}_j - \mathbf{r}_i| = (\mathbf{r}_j - \mathbf{r}_i)/L_{i,\ j}$ (Fig. 5.2).

WLSQ uses a cell-center distance $L_{i,j}$ as the weight function,

$$\omega_{i,j} = L_{i,j}{}^{-N} \tag{5.11}$$

and is called WLSQ (N) here for convenience. (Unweighted) LSQ is referred to as WLSQ (0) in this unified manner. It can be proved [16] that *only WLSQ (3) achieves second-order spatial accuracy in linear coordinate systems* having non-orthogonal and nonuniform grids.

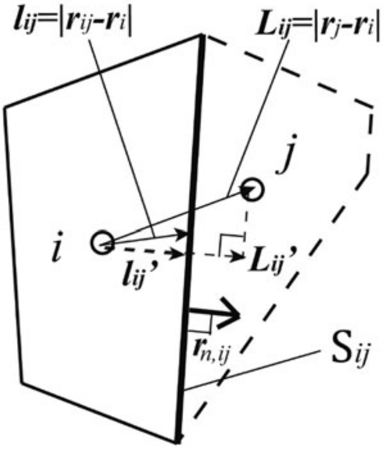

Fig. 5.2 Schematic of cell geometrical values of an arbitrary two-dimensional polygonal cell

5.1.2.2 WLSQ (G)

As will be explained in Sect. 5.1.3, the Green-Gauss (G-G) method features the usage of cell-face areas (rather than the cell-center distance) as appropriate weights for the cell-center values of the surrounding cells. The weight function, in which respect WLSQ is similar to G-G, was therefore proposed. From the gradient formula of WLSQ (N) in Eq. (5.8) and that of G-G (which will be given later in Sect. 5.1.3), the contributions from a surrounding (jth) cell, $\Delta q_{i,j}$, in each scheme is extracted as

$$\text{WLSQ} : \omega_{ij} L_{i,j} \mathbf{r}_{L,j} \Delta q_{i,j} \tag{5.12}$$

$$\text{G-G} : \frac{1}{V_i} s_{i,j} \alpha_{i,j} (\mathbf{r}_n)_{i,j} \Delta q_{i,j} \tag{5.13}$$

where V_i is the volume of the cell i, $s_{i,j}$ is the face area at the cell interface between i and j, $\alpha_{i,j}$ is an interpolation factor, and $(\mathbf{r}_n)_{i,\ j}$ is the outward (from i to j) unit-normal vector. If the mesh is nearly orthogonal, the following approximate relation can be obtained:

$$(\mathbf{r}_n)_{i,j} \approx \mathbf{r}_{L,j} \tag{5.14}$$

Because the coefficient $1/V_i$ is constant and thus neglected, we can use the following weight function for WLSQ.

$$\omega_{ij} = \frac{\alpha_{i,j} s_{i,j}}{L_{i,j}} \tag{5.15}$$

The interpolation factor $\alpha_{i,j}$ is defined to obtain spatially second-order accuracy in the 1D case. This discussion is valid also for parallel and linear meshes, even if they are non-orthogonal or nonuniform. When the factor $\alpha_{i,j}$ is defined as

$$\alpha_{Wi,j} = \left(\frac{2l_{i,j}}{L_{i,j}}\right)^2 \tag{5.16}$$

where $l_{i,j}$ is the distance between the cell center i and the cell-face center i,j, $l_{i,\,j} = |\mathbf{r}_{i,\,j} - \mathbf{r}_i|$, and the subscript "W" stands for "WLSQ," the weight function using this factor becomes

$$\omega_{i,j} = \left(\frac{2l_{i,j}}{L_{i,j}}\right)^2 \frac{s_{i,j}}{L_{i,j}} = 4s_{i,j}{l_{i,j}}^2{L_{i,j}}^{-3} \tag{5.17}$$

Consequently, it corresponds to the weight function of WLSQ (3) which has a second-order spatial accuracy, recalling that $s_{i,j}$ and $l_{i,j}$ are constants in 1D. For a non-orthogonal cell, Eq. (5.16) is extended by using projections of $L_{i,j}$ and $l_{i,j}$ to the cell-face normal, $L_{i,j}$', and $l_{i,j}$' (Fig. 5.2) as

$$\alpha_{Wi,j} = \left(\frac{2{l_{i,j}}'}{{L_{i,j}}'}\right)^2 \tag{5.18}$$

Finally, WLSQ that uses the following weight function is called WLSQ (G):

$$\omega_{i,j} = \left(\frac{2{l_{i,j}}'}{{L_{i,j}}'}\right)^2 \frac{s_{i,j}}{L_{i,j}} \tag{5.19}$$

WLSQ (G) preserves the linear distribution and gives second-order spatial accuracy for a parallel linear mesh.

5.1.3 Green-Gauss (G-G)

The cell-center gradient can be computed using G-G [2] as

$$\nabla q_i = \frac{1}{V_i}\sum_j s_{i,j}q_{i,j} \cdot (\mathbf{r}_n)_{i,j} \tag{5.20}$$

where $(\mathbf{r}_n)_{i,\,j}$ is the outward (from i to j) unit-normal vector, and $s_{i,j}$ is the face area, at the cell interface between i and j, respectively. Note that this formula can give exact averaged gradients in the cell with second-order accuracy at the cell center only if the exact cell-face averages $q_{i,j}$ and $s_{i,j}$ are available, which is not the case in actual numerical computations (only approximate cell-face values are at hand, instead).

To generalize the equation to those actual circumstances, we can use the following interpolated value of the neighboring cells:

$$q_{i,j} = \alpha_{i,j} q_i + \left(1 - \alpha_{i,j}\right) q_j = q_i + \alpha_{i,j} \Delta q_j \tag{5.21}$$

On isotropic grids, $\alpha_{i,j}$ is half; however, it should be treated as a variable for second-order spatial accuracy on other, general types of grids. With these values, the gradient using G-G is computed as

$$\nabla q_i = \frac{1}{V_i} \sum_j s_{i,j} \alpha_{i,j} \Delta q_j \cdot (\mathbf{r}_n)_{i,j} \tag{5.22}$$

where the contributions from q_i have canceled.

5.1.4 Green-Gauss/Least Squares (GLSQ)

It can be geometrically shown that WLSQ (G) should give reasonable gradients for typical mesh geometries. However, it was numerically shown that all WLSQs including WLSQ (G) can exhibit large reconstruction errors on a thin, distorted mesh even if the cell-center gradients were calculated properly. G-G, on the other hand, is more stable on such meshes. Thus, a mixed formula that switched between G-G [Eq. (5.22)] and WLSQ [Eq. (5.8)] was proposed.

$$\begin{aligned} [\beta_o \mathbf{M}_o + 2D(1 - \beta_o) V_i \mathbf{I}] \nabla q_i = \beta_o \sum_j \omega_{i,j} L_{i,j} \mathbf{r}_{Lj} \Delta q_j \\ + 2D(1 - \beta_o) \sum_j \alpha_{Gi,j} s_{i,j} (\mathbf{r}_n)_{i,j} \Delta q_{i,j} \beta_o \\ \in [0, 1] \end{aligned} \tag{5.23}$$

where $\alpha_{Gi,\ j}$ is the α of G-G, and D is a dimensional consistency constant. This formula gives G-G when the blending factor for interpolation $\beta_0 = 0$, and WLSQ when $\beta_0 = 1$. If WLSQ (G) is used as the WLSQ, the constant D can be simply taken as unity. Finally, the following method, called GLSQ (G-G/WLSQ), was obtained [16]:

Table 5.1 Properties of gradient reconstruction methods [16]

Gradient Reconstruction	Accuracy (second order on thin, curved meshes and Cartesian meshes having hanging nodes)	Monotonicity
WLSQ(0)	No	Yes (low accuracy)
WLSQ(1)	No	No
WLSQ(2)	No	No
WLSQ(3)	Yes	No
G-G	No	Yes
WLSQ(G)	Yes	No
GLSQ	Yes	Yes

$$[\beta_0 \mathbf{M}_0 + 2(1-\beta_0)V_i \mathbf{I}]\nabla q_i = \sum_j \left[\beta_0 \alpha_{Wi,j}\mathbf{r}_{Lj} + 2(1-\beta_0)\alpha_{Gi,j}(\mathbf{r}_n)_{i,j}\right] s_{i,j}\Delta q_{i,j} \tag{5.24}$$

GLSQ required an inversion of the 3×3 matrix, whose R.H.S. was slightly complicated. However, this computational cost increment was trivial, compared with many timesteps during the whole flow simulation. A parameter β_0 was expected to be used on thin, distorted cells, corresponding to G-G. Thus, the following simple definition was found sufficient for the hybrid meshes through our numerical experiments:

$$\begin{aligned} \beta_o &= \min\left(1, \frac{2}{AR}\right), \\ AR &\equiv \frac{2 \cdot \max|\mathbf{r}_{i,j} - \mathbf{r}_i| \cdot \max(s_{i,j})}{V_i} \end{aligned} \tag{5.25}$$

where AR was defined as an "effective" aspect ratio, equivalent to *(Maximum Side Length)/(Minimum Side Length)*, if, for instance, uniformly spaced 2D rectangular cells were considered. As a result, the full WLSQ (G) is used in cells of $AR < 2$, and G-G are used in higher-aspect-ratio cells. Eventually, WLSQ (G) is used in the Cartesian mesh, whereas G-G is used in the layer cells part. The properties of those reconstruction methods for unstructured grids are summarized in Table 5.1.

5.2 Conventional Limiters

The slope limiting functions (also known as "limiters") are summarized in Fig. 5.3. In cell-centered FVM, as briefly reviewed above, the cell-interface values $q_{i,j}$ are extrapolated from the cell-center values q_i using the gradients ∇q_i, distance between the center $\mathbf{r}_i$ and the interface $\mathbf{r}_{i,j}$ (see Fig. 5.2), and the slope limiting function ϕ:

$$q_{i,j} = q_i + \phi \nabla q_i \cdot \left(\mathbf{r}_{i,j} - \mathbf{r}_i\right) \tag{5.6}$$

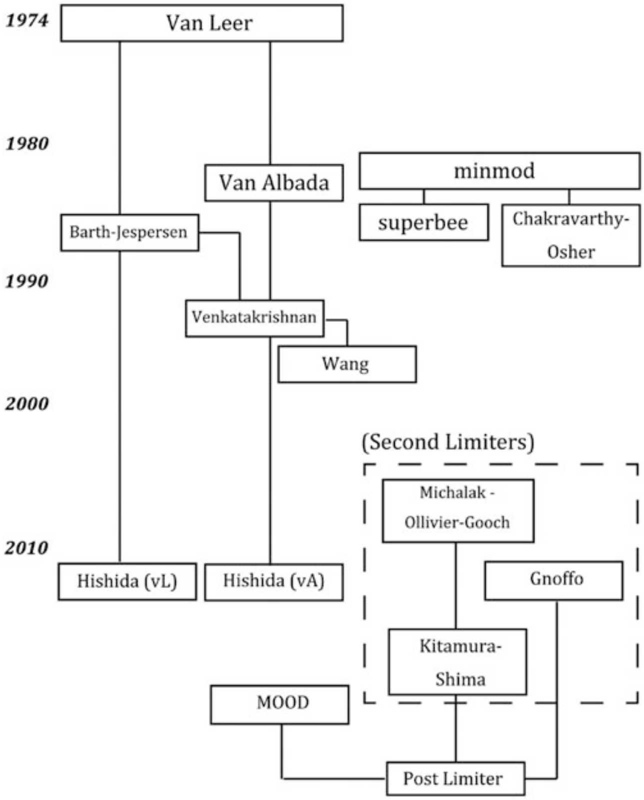

Fig. 5.3 Slope limiter tree

where the limiter ϕ can be (i) common to all the variables, (ii) computed for each variable, or (iii) once calculated, for instance, for ρ and p independently, but with their minimum used for all the primitive values (i.e., ρ, u, v, w, p in 3D). These (i)–(iii) significantly affect the solutions, although this important information is often omitted in literature.

According to Godunov's theorem [17], these slope limiters are necessary to stabilize the solutions of a spatially second-order scheme or higher, specifically at discontinuities such as shocks. When the limiter is activated ($\phi = 0$), the cell-interfacial value $q_{i,j}$ is the same as the cell-center value q_i at the cell (the variable q has no variation within the cell i), i.e., first-order in space. These limiters are briefly reviewed in the following.

5.2.1 Minmod

The minmod function is expressed as follows:

$$\mathrm{minmod}(a,b) = \begin{cases} a & \mathit{if}\, r \geq 1 \\ b & \mathit{if}\, 0 \leq r < 1\,; r = \dfrac{b}{a} \\ 0 & \mathit{if}\, r < 0 \end{cases} \tag{5.26}$$

In other words,

$$\phi_{mm} = \mathrm{minmod}(1,r) = \begin{cases} 1 & \mathit{if}\ r \geq 1 \\ r & \mathit{if}\ 0 \leq r < 1 \\ 0 & \mathit{if}\ r < 0 \end{cases} \tag{5.27}$$

When it is used as a limiter, a and b are variable gradients such as $\frac{q_{i+1}-q_i}{\Delta x}$ and $\frac{q_{i+2}-q_{i+1}}{\Delta x}$ (for structured grids), or ∇q_i and ∇q_j (for unstructured grids). Then, if they have opposite signs, $\phi_{\mathrm{mm}} = 0$, and the order of the spatial accuracy is degraded to one locally; otherwise, the gradient having a smaller magnitude is commonly employed at both sides [18].

Then, for structured grids, Eqs. (5.1) and (5.2) are replaced with

$$\begin{aligned} q_{i+1/2,L} = q_i &+ \frac{1+\kappa}{4}\mathrm{minmod}\left[q_{i+1}-q_i, q_i - q_{i-1}\right] \\ &+ \frac{1-\kappa}{4}\mathrm{minmod}\left[q_i - q_{i-1}, q_{i+1}-q_i\right] \end{aligned} \tag{5.28}$$

$$\begin{aligned} q_{i+1/2,R} = q_{i+1} &- \frac{1-\kappa}{4}\mathrm{minmod}\left[q_{i+2}-q_{i+1}, q_{i+1} - q_i\right] \\ &- \frac{1+\kappa}{4}\mathrm{minmod}\left[q_{i+1} - q_i, q_i-q_{i-1}\right] \end{aligned} \tag{5.29}$$

This limiter is very strong, robust, and well used. Due to its non-differentiability, however, it can cause convergence problems. In addition, because it is easily activated at places other than shocks, it can smear the solutions [19].

5.2.2 van Leer

The van Leer limiter is written as follows:

$$\phi_{VL} = \frac{|r|+r}{1+r} = \begin{cases} \dfrac{2r}{1+r} = \dfrac{2ab}{a+b} & \mathit{if}\, r \geq 0 \\ 0 & \mathit{if}\, r < 0 \end{cases} \tag{5.30}$$

which is smooth for $r \geq 0$, unlike the minmod limiter.

As van Albada and van Leer [20] pointed out, however, this limiter had a zero-division problem if $a = -b$.

5.2.3 van Albada

Thus, van Albada and van Leer [20] proposed the following smoother limiter:

$$\phi_{VA} = \frac{2ab + \varepsilon}{a^2 + b^2 + \varepsilon} \tag{5.31}$$

with ε being a small positive number (such as 1.e−6) to avoid zero division even in smooth regions [5].

In the actual implementation,

$$s = \frac{2 \cdot (q_{i+1} - q_i) \cdot (q_i - q_{i-1}) + \varepsilon}{(q_{i+1} - q_i)^2 + (q_i - q_{i-1})^2 + \varepsilon} \tag{5.32}$$

and then, Eqs. (5.1) and (5.2) are replaced with

$$q_{i+1/2,L} = q_i + s \cdot \left[\frac{1 + s\kappa}{4}(q_{i+1} - q_i) + \frac{1 - s\kappa}{4}(q_i - q_{i-1})\right] \tag{5.33}$$

$$q_{i+1/2,R} = q_{i+1} - s \cdot \left[\frac{1 - s\kappa}{4}(q_{i+2} - q_{i+1}) + \frac{1 + s\kappa}{4}(q_{i+1} - q_i)\right] \tag{5.34}$$

The author would like to warn the reader that the original form in [20] was

$$ave(a,b) = \frac{(b^2 + \varepsilon')a + (a^2 + \varepsilon')b}{a^2 + b^2 + 2\varepsilon'} \tag{5.35}$$

which can be confusing and may look different from Eq. (5.31). However, it is interpreted as follows (Shima, E., private communication, July-09-2008). The "ave" stands for the (weighted) average, and thus, starting from Eq. (5.35), the above equation can be expressed as the product of the "arithmetic average of both sides" and "the rest":

$$\begin{aligned} ave(a,b) &= \frac{a+b}{2}\frac{2ab + \varepsilon}{a^2 + b^2 + \varepsilon} \\ &= \frac{(a+b)(ab + (\varepsilon/2))}{a^2 + b^2 + \varepsilon} \\ &= \frac{(b^2 + (\varepsilon/2))a + (a^2 + (\varepsilon/2))b}{a^2 + b^2 + \varepsilon} \end{aligned} \tag{5.36}$$

If $\varepsilon' = \varepsilon/2$, Eqs. (5.35) and (5.36) are the same.

5.2.4 Barth–Jespersen

Barth–Jespersen's limiter [3] is described as follows according to Wang [21]:

$$\phi_{BJ} = \min\left[1, \left(\frac{\max\limits_j |q_j - q_i|}{\max\limits_j |q_{i,j} - q_i|}\right), \left(\frac{\min\limits_j |q_j - q_i|}{\min\limits_j |q_{i,j} - q_i|}\right)\right] \tag{5.37}$$

where q_j is the value at the neighboring cell j of cell i, and $q_{i,j}$ is the value at the cell interface separating cells i and j, within the cell i. Note that this form is slightly different from the original expression in [3], because the present book uses variables only at cell centers, whereas [3] used cell-center and cell-vertex values both [21].

This limiter is applicable to unstructured grids. As noted in [4], however, it can fail to reach convergence due to its non-differentiability, similar to van Leer's limiter on structured grids.

5.2.5 Venkatakrishnan

This limiter [4] is sometimes regarded as an unstructured grid version of the van Albada limiter due to its differentiability and its similarity in form to van Albada's.

$$\phi_{Ven} = \frac{1}{\Delta_-}\left[\frac{\left({\Delta_-}^2 + \varepsilon^2\right)\Delta_- + 2{\Delta_-}^2\Delta_+}{{\Delta_+}^2 + 2{\Delta_-}^2 + \Delta_+\Delta_- + \varepsilon^2}\right] \tag{5.38}$$

$$\Delta_- = q_{i,j} - q_i, \Delta_+ = \begin{cases} q_{\max} - q_i & if\, \Delta_- > 0 \\ q_{\min} - q_i & if\, \Delta_- < 0 \end{cases} \tag{5.39}$$

where $q_{\max}$ and $q_{\min}$ are the maximum and the minimum values, respectively, over the current cell i and its *all the surrounding* cells j,

$$\varepsilon^2 = (K\Delta x)^3 \tag{5.40}$$

where K is constant ($K = 0.3$ or 5.0, for instance) and Δx is the mesh size, or given by Wang's corrected expression [7]

$$\varepsilon = \varepsilon'\left(q^{\max} - q^{\min}\right) \tag{5.41}$$

where $\varepsilon' = 0.05$, and $q^{\max}$ and $q^{\min}$ are the maximum and the minimum over the *whole* computational domain. Either way, this limiter achieves better overall convergence than its predecessor by Barth–Jespersen [3]; however, its convergence rate is hindered by several factors, such as unexpected activation at hanging nodes where grid sizes change abruptly [12]. Thus, the parameter K or ε' should be carefully chosen.

5.3 Second Limiters and Post Limiter

Unstructured grids are popular because they can handle complex geometries [9, 12–14, 22–28]. The slope limiters for unstructured grids are likely to encounter convergence difficulty, even in smooth regions, because the slope limiter can be activated by trivial differences in the surrounding cells (as reviewed in Sect. 5.2). One way to avoid this problem is obviously to turn off limiters, but such a strategy is effective only when the whole computational domain is *a priori* known to be filled with subsonic flows; otherwise, some portion of the computational region may become supersonic and create shock waves.

This difficulty was removed in [29] by interchanging the "supersonic-mode" and "subsonic-mode" of the limiter, though in an elaborate manner (explained later in Sect. 5.3.1). In addition, because their modification was extended from the Barth–Jespersen limiter involving several user-defined parameters, its general applicability was questionable. Similarly, various additional limiters are available in commercial or research codes [30, 31], but such techniques have not been thoroughly investigated nor have they been widely utilized. Therefore, in [28], a simpler, parameter-free, and easy-to-use alternative was pursued for engineering purposes.

Further, because it is known from Godunov's theorem [17] that a second-order scheme or higher in space is unstable at discontinuities, typically the limiters are locally adopted there to avoid the instabilities. However, *Godunov's theorem is based on linear (or linearized) equations. Its validity is hence unclear in nonlinear practical problems solving Euler or Navier–Stokes equations.*

In fact, in our preliminary simulation for a 2D shock/boundary-layer interaction problem [19], $4 \times 4 = 16$ times the equivalent resolution was achieved without a limiter, compared with the conventional, limiter-ON computational case. Nevertheless, whether the computation indeed continued stably depended on the shock strength and mesh smoothness. A second limiter such as [28] deactivates the (first) limiter at subsonic speed depending on the solution.

Methods proposed in [28, 29, 32] are so-called "second (or auxiliary) limiters" that are also belong to the category of *a priori* limiters. This is because these limiters use already available values only, i.e., local Mach number [28, 29], and pressure ratio [32].

Clain et al. [33], on the other hand, proposed the MOOD (Multi-dimensional Optimal Order Detection) framework, which includes an "*a posteriori*" limiting procedure. In their *a posteriori* limiting, the spatial accuracy is degenerated from higher order to lower order only when it is truly necessary. Its paradigm structure is, however, complicated, and a simpler alternative was desired for popular second-order unstructured grid methods [2, 14, 15, 34–38]. In addition, although [33] and subsequent papers [39, 40] were not dedicated to convergence improvement to steady solutions, our proposal [19] examined and improved it.

Higher-order methods [41–48] such as DG (discontinuous Galerkin) [49], SV (spectral-volume) [50], or residual distribution [51, 52] are, of course, attractive. At the moment of preparation of this book, however, they usually call for smooth structured grids, and thus, there are relatively fewer examples in practical simulations to date. Furthermore, typical higher-order methods are known to be quite expensive, except for recent, cheaper alternatives [53]. The second-order unstructured grid FVMs which are, in contrast, available in standard CFD codes such as [15, 54, 55].

5.3.1 Michalak and Ollivier-Gooch Second Limiter

Michalak and Ollivier-Gooch [29] proposed the following implementation for convergence improvement of (the first) Barth–Jespersen's limiter.

$$\phi'_{MO} = \widetilde{\sigma}_i + (1 - \widetilde{\sigma}_i)\phi_{1-BJ}; \tag{5.42}$$

$$\widetilde{\sigma}_i = \begin{cases} 1 & (\Delta q)^2 \le (K\Delta x)^3 \\ s\left(\dfrac{(\Delta q)^2 - (K\Delta x)^3}{(K\Delta x)^3}\right) & (K\Delta x)^3 < (\Delta q)^2 < 2(K\Delta x)^3 \\ 0 & (\Delta q)^2 \ge 2(K\Delta x)^3 \end{cases} \tag{5.43}$$

$$\begin{aligned} &\Delta q \equiv (\Delta q)_i^{\max} - (\Delta q)_i^{\min} < (K\Delta x)^{1.5}, \\ &(\Delta q)_i^{\max} = \max\left(q_j - q_i\right), (\Delta q)_i^{\min} = \min\left(q_j - q_i\right) \end{aligned} \tag{5.44}$$

$$s(y) = 2y^3 - 3y^2 + 1 \tag{5.45}$$

where $\phi_{1\text{-}BJ}$ is the (first) limiting function derived from Barth–Jespersen limiter [3].

This method successfully disabled the limiter in smooth regions. However, the user needs to specify the constant K, which was borrowed from Venkatakrishnan's limiter, used in a different manner from the original limiter [4]. Furthermore, an additional modification was made using two prescribed Mach numbers, $M_1 = 0.8$ and $M_2 = 0.85$, in their supersonic case to accurately treat the stagnation region:

$$\phi_{MO} = \widehat{\sigma}_i + (1 - \widehat{\sigma}_i)\phi'_{MO}; \tag{5.46}$$

$$\widehat{\sigma}_i = \begin{cases} 1 & M_{i,\max} \leq M_1 \\ s\left(\dfrac{M_{i,\max} - M_1}{M_2 - M_1}\right) & M_1 < M_{i,\max} < M_2 \\ 0 & M_{i,\max} \geq M_2 \end{cases} \tag{5.47}$$

where $M_{i,\max}$ stands for the maximum Mach number of the control volume averages of the reconstruction stencil of cell i. Thus, the resulting limiter contains several tunable parameters K, M_1, and M_2.

5.3.2 Kitamura–Shima Second Limiter

We simply required that limiters be activated only at shock discontinuities, without any user-defined values. In other words, we focused on whether they are turned off (i.e., $\phi_2 = 1$) at subsonic speeds, not in the supersonic smooth regions. Thus, we proposed the following modification to the limiter function ϕ_1:

$$\phi_{2.} = \max\left[\phi_1, f(M_{\max})\right]; \tag{5.48}$$

$$M_{\max} = \max_j\left(M, M_j\right) \tag{5.49}$$

where j stands for any neighboring cells of the current cell, with

$$f(M) = 0.5\{1 - \tanh(5\pi(M-1))\} \tag{5.50}$$

Then, the final form of the modification to the existing limiters is given as

$$\phi_2 = \max\left[\phi_1, 0.5\{1 - \tanh(5\pi(M_{\max} - 1))\}\right] \tag{5.51}$$

$$M_{\max} = \max_j\left(M, M_j\right) \tag{5.52}$$

Note that this modification is *applicable to any existing slope limiter*, because it is used immediately after the usual computation of the limiter function ϕ_1 without the requirement for any specified parameters. Such an implementation can be called a "second" limiter (ϕ_2), because it is applied after the "first" limiter for the original ϕ_1. The formal second-order accuracy is retained [28].

5.3.3 Post Limiter

The second-order method requires a limited value, q^{lim}, or an "unlimited" (without a limiter, in a smooth flow region) candidate value, q^{unlim}, which are both available in the same loop in the code, because they differ only in whether the limiter value is multiplied by the gradient or not.

$$q_{i,j}^{unlim} = q_i + \nabla q_i \cdot (\mathbf{r}_{i,j} - \mathbf{r}_i) \tag{5.53}$$

$$q_{i,j}^{\mathrm{lim}} = q_i + \phi \nabla q_i \cdot (\mathbf{r}_{i,j} - \mathbf{r}_i) \tag{5.54}$$

where ϕ is the conventional, a priori limiter value.

Thus, a simpler *a posteriori* method was established that simply chose the cell-interfacial values from these two candidates, or even blended them, unlike the MOOD or the *a priori* approach, which selects one of these two *before* actually employing the unlimited value.

As for the criteria for adopting unlimited values, "(i) The positivity: $\rho^{unlim} > 0$ and $p^{unlim} > 0$," and "(ii) DMP (Discrete Maximum Principle) [$\min(\rho_i, \rho_j) < \rho^{unlim} < \max(\rho_i, \rho_j)$ and $\min(p_i, p_j) < p^{unlim} < \max(p_i, p_j)$]" were borrowed from MOOD [33].

As an additional criterion, after a careful investigation of the literature on shock detection [56, 57], we decided to employ "(iii) Gnoffo's auxiliary limiter [33]", because it is continuous, and is based on the pressure ratio as follows:

$$\phi_G = \frac{1 - \cos(\Phi\pi)}{2} \tag{5.55}$$

$$\Phi = \min\left[1, \max\left(0, \frac{\varphi_{\max} - \varphi}{\varphi_{\max} - \varphi_{\min}}\right)\right] \tag{5.56}$$

$$\varphi = \frac{p_{\max}}{p_{\min}} \tag{5.57}$$

$$p_{\max} = \max\left(p^{unim}, p_i, p_j\right) \tag{5.58}$$

$$p_{\min} = \min\left(p^{unim}, p_i, p_j\right) \tag{5.59}$$

where $(\varphi_{\max}, \varphi_{\min}) = (3, 2)$ (so that $0 \leq \phi_G \leq 1$) here. Thus, if the pressure ratio $\varphi \geq 3$, then $\phi_G = 0$, and if $\varphi \leq 2$, $\phi_G = 1$. As a result, *even if DMP is not satisfied, the unlimited value can be fully or partially adopted*, according to the pressure ratio. These are summarized as follows. If conditions (i) and (ii) apply, the final limiter is unity; if only (i) holds, it is ϕ; otherwise, 0. Then, (iii) the Gnoffo form interpolates between the two candidates:

$$q = \phi_{\mathrm{G}}\, q^{unlim} + (1 - \phi_{\mathrm{G}}) q^{lim} \tag{5.60}$$

where q^{unlim} and q^{lim} are given by Eqs. (5.53) and (5.54), respectively, and ϕ_G is calculated according to Eq. (5.55). Even if (ii) DMP is not strictly satisfied, the two values of q^{unlim} and q^{lim} are connected smoothly by (iii) Gnoffo's auxiliary limiter, unlike the MOOD.

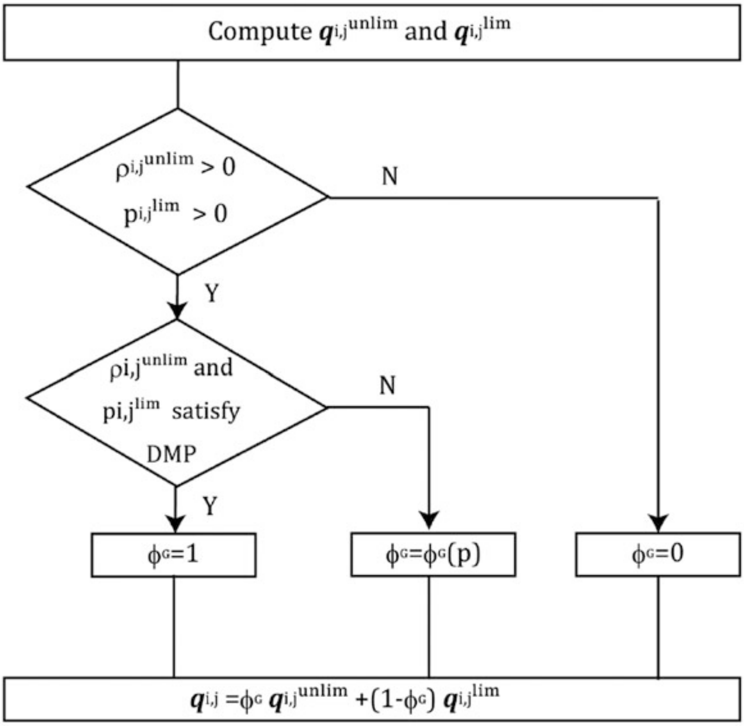

Fig. 5.4 Flowchart of post limiter

Therefore, the present, simple *a posteriori* limiter ("post limiter"), ϕ_{final}, employs the unlimited value ($\phi_{final} = 1$) as much as possible, and blends the unlimited and limited values ($\phi_{final} = \phi_{lim}$) smoothly using Gnoffo's auxiliary limiter function, ϕ_G elsewhere [32], as long as positivity of the density and pressure is satisfied (Fig. 5.4).

The above procedure is further summarized as

$$q_{i,j} = q_i + \phi_{final} \nabla q_i \cdot \left(\mathbf{r}_{i,j} - \mathbf{r}_i\right) \tag{5.61}$$

$$\phi_{final} = \phi_G + (1 - \phi_G) \cdot \phi_{\lim} \tag{5.62}$$

where ϕ_G again lies between 0 (large pressure ratio, or negative density/pressure) and 1 (small pressure ratio, and smooth).

The post limiter can easily be implemented on 1D or smooth structured grids (such as in astrophysics [47]). On unstructured grids, however, additional care should be paid to cell geometries [58]. If shocks are better detected [59], its accuracy and robustness may be improved further.

References

1. van Leer, B.: Towards the ultimate conservative difference scheme. V. A second-order sequel to Godunov's method. J. Comput. Phys. **32**, 101–136 (1979)
2. Mavriplis, D.J.: Revisiting the least-squares procedure for gradient reconstruction on unstructured meshes. In: AIAA Paper 2003-3986 (2003)
3. Barth, T.J., Jespersen, D.C.: The design and application of upwind schemes on unstructured meshes. In: AIAA Paper 89-0366 (1989)
4. Venkatakrishnan, V.: Convergence to steady state solutions of the Euler equations on unstructured grids with limiters. J. Comput. Phys. **118**, 120–130 (1995)
5. Anderson, W.K., Thomas, J.L., van Leer, B.: Comparison of finite volume flux vector splittings for the Euler equations. J. Comput. Phys. **24**, 1453–1460 (1986)
6. Burg, C.O.E.: Higher order variable extrapolation for unstructured finite volume RANS flow solvers. In: AIAA-2005-4999 (2005)
7. Wang, Z.J.: A fast nested multi-grid viscous flow solver for adaptive Cartesian/quad grids. Int. J. Numer. Methods Fluids. **33**, 657–680 (2000)
8. Aftosmis, M., Gaitonde, D., Tavares, T.S.: On the accuracy, stability and monotonicity of various reconstruction algorithms for unstructured meshes. In: AIAA Paper 94-0415 (1994)
9. Hirsch, C.: Numerical Computation of Internal and External Flows, Volume 1, Second edition: The Fundamentals of Computational Fluid Dynamics. Butterworth-Heinemann, Burlington (2007)
10. Shima, E., Kitamura, K., Fujimoto, K.: New gradient calculation method for MUSCL type CFD schemes in arbitrary polyhedra. In: AIAA Paper 2010-1081 (2010)
11. Tamaki, Y., Harada, M., Imamura, T.: Near-Wall Modification of Spalart–Allmaras Turbulence Model for Immersed Boundary Method. AIAA J. **55**(9), 3027-3039 (2017). https://doi.org/10.2514/1.J055824
12. Wang, Z.J., Chen, R.F.: Anisotropic solution-adaptive viscous Cartesian grid method for turbulent flow simulation. AIAA J. **40**, 1969–1978 (2002)
13. Aftosmis, M.J., Berger, M.J., Alonso, J.J.: Applications of a Cartesian mesh boundary-layer approach for complex configurations. In: AIAA Paper 2006-0652 (2006)
14. Luo, H., Spiegel, S., Lohner, R.: Hybrid grid generation method for complex geometries. AIAA J. **48**, 2639–2647 (2010). https://doi.org/10.2514/1.J050491
15. Hashimoto, A., Murakami, K., Aoyama, T., Ishiko, K., Hishida, M., Sakashita, M., Lahur, P.R.: Toward the fastest unstructured CFD code 'FaSTAR'. In: 50th AIAA Aerospace Sciences Meeting Including the New Horizons Forum and Aerospace Exposition, AIAA Paper 2012-1075 (2012)
16. Shima, E., Kitamura, K., Haga, T.: Green-gauss/weighted-least-squares hybrid gradient reconstruction for arbitrary polyhedra unstructured grids. AIAA J. **51**(11), 2740–2747 (2013). https://doi.org/10.2514/1.J052095
17. Godunov, S.K.: Different methods for shock waves. Ph.D. Dissertation. Moscow State University (1954)
18. Roe, P.L.: Characteristic-based schemes for the Euler equations. Annu. Rev. Fluid Mech. **18**, 337–365 (1986)
19. Kitamura, K., Hashimoto, A.: Simple a posteriori slope limiter (post limiter) for high resolution and efficient flow computations. J. Comput. Phys. **341**, 313–340 (2017). https://doi.org/10.1016/j.jcp.2017.04.002
20. van Albada, G.D., van Leer, B., Roberts Jr., W.W.: A comparative study of computational methods in cosmic gas dynamics. Astron. Astrophys. **108**, 76–84 (1982)
21. Wang, Z.J.: A Quadtree-based adaptive Cartesian/quad grid flow solver for Navier-Stokes equations. Comput. Fluids. **27**, 529–549 (1998)
22. Kidron, Y., Mor-Yossef, Y., Levy, Y.: Robust Cartesian grid flow solver for high-Reynolds-number turbulent flow simulations. AIAA J. **48**, 1130–1140 (2010). https://doi.org/10.2514/1.45817

23. Nakahashi, K.: Building-cube method for flow problems with broadband characteristic length. In: Armfield, S., Morgan, R., Srinivas, K. (eds.) Computational Fluid Dynamics 2002, pp. 77–81. Springer, Cham (2003)
24. Lahur, P.R.: Hexahedra grid generation method for flow computation. In: AIAA Paper 2004-4958 (2004)
25. Kamatsuchi, T.: Turbulent flow simulation around complex geometries with Cartesian grid method. In: AIAA Paper 2007-1459 (2007)
26. Kallinderis, Y., Khawaja, A., McMorris, H.: Hybrid prismatic/tetrahedral grid generation for complex geometries. In: AIAA Paper 1995-0210 (1995)
27. Ochi, A., Ibrahim, M.K., Nakamura, Y.: Computational fluid dynamics validation study of wake-capturing capability for a flat-plate wake. J. Aircraft. **47**, 441–449 (2010). https://doi.org/10.2514/1.33502
28. Kitamura, K., Shima, E.: Simple and parameter-free second slope limiter for unstructured grid aerodynamic simulations. AIAA J. **50**(6), 1415–1426 (2012). https://doi.org/10.2514/1.J051269
29. Michalak, C., Ollivier-Gooch, C.: Accuracy preserving limiter for the high-order accurate solution of the Euler equations. J. Comput. Phys. **228**, 8693–8711 (2009). https://doi.org/10.1016/j.jcp.2009.08.021
30. Gnoffo, P.A.: Semi-analytic reconstruction of flux in finite volume formulations. In: AIAA Paper 2006-1090 (2006)
31. CFL3D Version 6 Web Page, http://cfl3d.larc.nasa.gov/, Accessed Feb 2011
32. Gnoffo, P.A.: Updates to multi-dimensional flux reconstruction for hypersonic simulations on tetrahedral grids. In: AIAA 2010-1271 (2010)
33. Clain, S., Diot, S., Loubère, R.: A high-order finite volume method for systems of conservation laws–multi-dimensional optimal order detection (MOOD). J. Comput. Phys. **230**, 4028–4050 (2011)
34. Kitamura, K., Fujimoto, K., Shima, E., Kuzuu, K., Wang, Z.J.: Validation of an arbitrary unstructured CFD code for aerodynamic analyses. Trans. JSASS. **53**(182), 311–319 (2011)
35. Gnoffo, P., Buck, G., Moss, J., Nielsen, E., Berger, K., Jones, W.T., Rubavsky, R.: Aerothermodynamic analyses of towed Ballutes. In: AIAA Paper 2006-3771 (2006)
36. Pandya, S., Onufer, J., Chan, W., Klopfer, G.: Capsule Abort Recontact Simulation. NAS technical report, NAS-06-005 (2006)
37. Catalano, P., Marini, M., Nicoli, A., Pizzicaroli, A.: CFD contribution to the aerodynamic data set of the Vega launcher. J. Spacecraft Rockets. **44**, 42–51 (2007)
38. Kitamura, K., Nonaka, S., Kuzuu, K., Aono, J., Fujimoto, K., Shima, E.: Numerical and experimental investigations of epsilon launch vehicle aerodynamics at Mach 1.5. J. Spacecraft Rockets. **50**(4), 896–916 (2013)
39. Diot, S., Clain, S., Loubère, R.: Improved detection criteria for the multi-dimensional optimal order detection (MOOD) on unstructured meshes with very high-order polynomials. Comput. Fluids. **64**, 43–63 (2012)
40. Diot, S., Loubère, R., Clain, S.: The MOOD method in the three-dimensional case: very high-order finite volume method for hyperbolic systems. Int. J. Numer. Methods Fluids. **73**, 362–392 (2013)
41. Jiang, G.-S., Shu, C.-W.: Efficient implementation of weighted ENO schemes. J. Comput. Phys. **126**, 202–228 (1996)
42. Hu, C., Shu, C.W.: Weighted essentially non-oscillatory schemes on triangular meshes. J. Comput. Phys. **150**, 97–127 (1999)
43. Dumbser, M., Balsara, D., Toro, E.F., Munz, C.D.: A unified framework for the construction of one-step finite-volume and discontinuous Galerkin schemes on unstructured meshes. J. Comput. Phys. **227**, 8209–8253 (2008)
44. Loubère, R., Dumbser, M., Diot, S.: A new family of high order unstructured MOOD and ADER finite volume schemes for multidimensional systems of hyperbolic conservation laws. Commun. Comput. Phys. **16**, 718–763 (2014)

45. Dumbser, M., Loubère, R.: A simple robust and accurate a posteriori sub-cell finite volume limiter for the discontinuous Galerkin method on unstructured meshes. J. Comput. Phys. **319** (15), 163–199 (2016)
46. Dumbser, M., Zanotti, O., Loubère, R., Diot, S.: A posteriori subcell limiting for discontinuous Galerkin finite element method for hyperbolic system of conservation laws. J. Comput. Phys. **278**, 47–75 (2014)
47. Zanotti, O., Fambri, F., Dumbser, M.: Solving the relativistic magnetohydrodynamics equations with ADER discontinuous Galerkin methods, a posteriori subcell limiting and adaptive mesh refinement. Mon. Not. R. Ast. Soc. **452**, 3010–3029 (2015)
48. Zanotti, O., Fambri, F., Dumbser, M., Hidalgo, A.: Space-time adaptive ADER discontinuous Galerkin finite element schemes with a posteriori sub-cell finite volume limiting. Comput. Fluids. **118**, 204–224 (2015)
49. Cockburn, B., Shu, C.W.: The Runge–Kutta discontinuous Galerkin method for conservation laws V multidimensional systems. J. Comput. Phys. **141**, 199–224 (1998)
50. Wang, Z.J., Zhang, L., Liu, Y.: Spectral (finite) volume method for conservation Laws on unstructured grids IV – extension to two-dimensional systems. J. Comput. Phys. **194**, 716–741 (2004)
51. van Leer, B.: Upwind and high-resolution methods for compressible flow: from donor cell to residual-distribution schemes. Commun. Comput. Phys. **1**, 192–206 (2006)
52. Nishikawa, H.: A first-order system approach for diffusion equation. I: second-order residual-distribution schemes. J. Comput. Phys. **227**, 315–352 (2007). https://doi.org/10.1016/j.jcp.2007.07.029
53. Hu, X.Y., Wang, B., Adams, N.A.: An efficient low-dissipation hybrid weighted essentially non-oscillatory scheme. J. Comput. Phys. **301**, 415–424 (2015)
54. Diskin, B., Nishikawa, H.: Evaluation of Multigrid Solutions for Turbulent Flows. AIAA 2014-0082 (2014)
55. Langer, S., Schwöppe, A., Kroll, N.: The DLR flow solver TAU – status and recent algorithmic developments. In: AIAA 2014-0080 (2014)
56. Ducros, F., Ferrand, V., Nicoud, F., Weber, C., Darracq, D., Gacherieu, C., Poinsot, T.: Large-Eddy simulation of the shock/turbulence interaction. J. Comput. Phys. **152**, 517–549 (1999)
57. Shima, E., Kitamura, K.: Multidimensional numerical noise from captured shockwave and its cure. AIAA J. **51**(4), 992–998 (2013)
58. Kitamura, K., Aogaki, T., Inatomi, A., Fukumoto, K., Takahama, T., Hashimoto, A.: Post limiters and simple dirty-cell detection for three-dimensional, unstructured, (unlimited) aerodynamic simulations. AIAA J. **56**(8), 3192–3204 (2018). https://doi.org/10.2514/1.J056683
59. Fujimoto, T., Kawasaki, T., Kitamura, K.: Canny-edge-detection/Rankine-Hugoniot-conditions unified shock sensor for inviscid and viscous flows. J. Comput. Phys. **396**, 264–279 (2019). https://doi.org/10.1016/j.jcp.2019.06.071